Automotive fan noise reduction using flow obstructions

Tjeu Gehlen

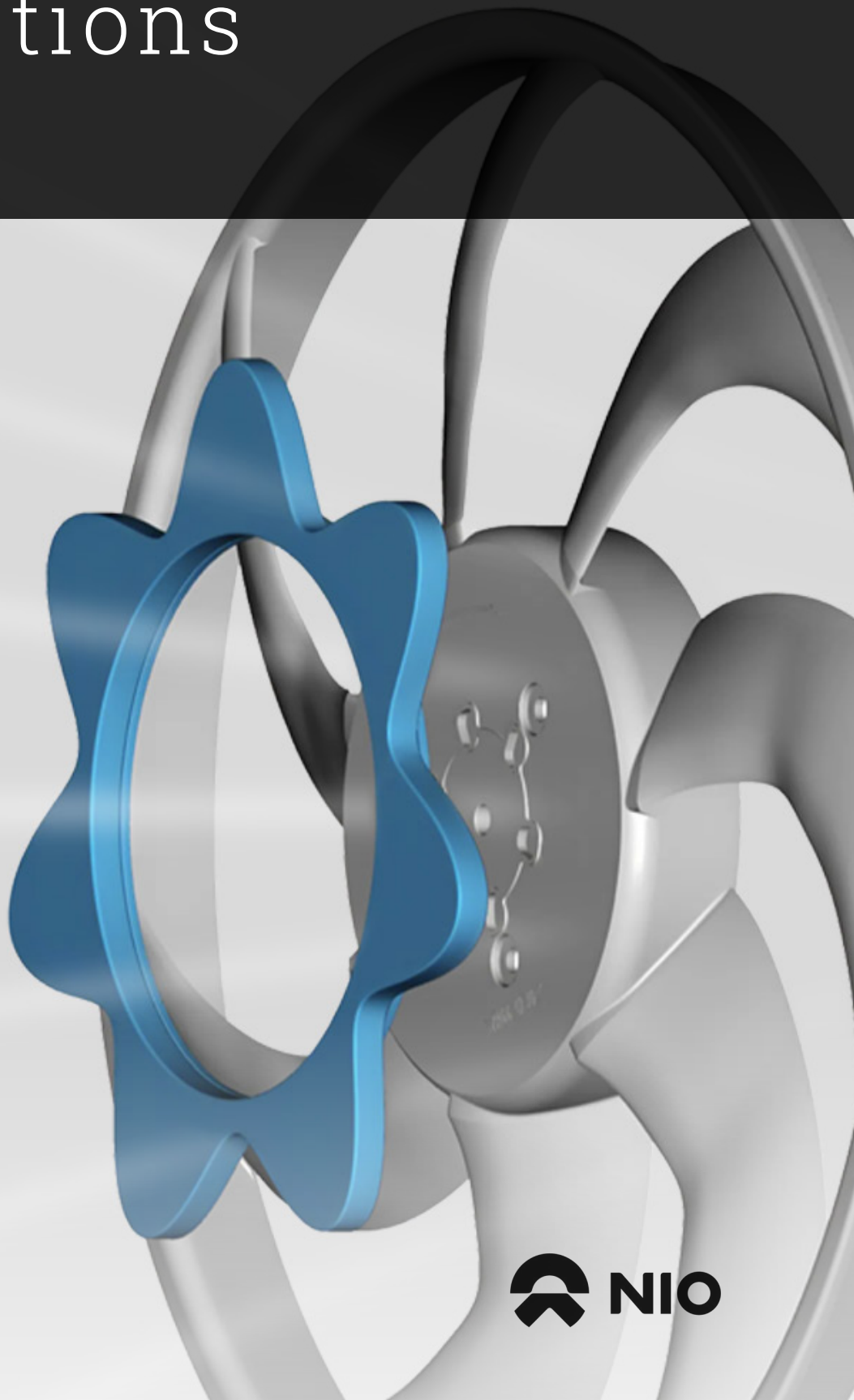

Delft University of Technology

TU Delft

NIO

Automotive fan noise reduction using flow obstructions

by

Tjeu Gehlen

to obtain the degree of Master of Science
at the Delft University of Technology,
to be defended on Wednesday May 22, 2024 at 13:00.

Student number: 4682858

Thesis committee:	Dr. Ir. D. Ragni,	TU Delft, supervisor
	Prof. Dr. Ir. F. Avallone,	TU Delft
	Dr. Ir. T. Sinnige,	TU Delft
	Ir. A. Bissell,	NIO Engineering Ltd

TU Delft

NIO

Preface

Finishing this thesis marks the end of a year of modal decompositions, Fourier transforms, and acoustic analogies, racking my brain on these concepts to get a fan just that bit quieter. But it also finalizes the end of my time as a student in Delft, on which I look back with joy.

Regarding this thesis there are a number of people I would like to thank. First of all, I want to thank my supervisors Daniele Ragni, Francesco Avallone, and Andy Bissell, for their guidance, support, and feedback throughout the entire project. Also, thanks to Adam Bushell for arranging the project within NIO. I'm furthermore thankful to Olaf, Michiel, Friso, Bieke, and Laurens for sharing the office and making the lunch and coffee breaks fun and enjoyable. Special thanks to my fellow thesis students, the 'noise-boys' Marlon and Hielke, and also Jop. Going through this year on a similar timeline has helped in keeping our spirits high and the fun alive, but I also believe it has improved our own work. Latly, I would like to thank Stephan Bernardy, Martijn Looman, and Tercio Lima Pereira for their support during the preparation of the experimental campaign, and Henry den Bok for allowing me to use the anechoic chamber.

Finally, I want to thank my family and friends for the support and joy they have given me not just during this thesis, but throughout all of my student years.

Tjeu Gehlen
Delft, May 2024

Summary

With the ever-increasing issues caused by global warming, the emission of carbon dioxide has to be minimized. With the transport section being responsible for 24% of global emissions, the demand for electric alternatives is on the rise. The electrification of passenger vehicles comes with benefits like a smoother driving experience, requiring less maintenance, and has led to an overall noise decrease. However, annoying noises that were previously masked by loud engines are now audible. Automotive cooling fan noise is such an example. The tonal character of the fan is annoying to pedestrians and residents, especially during car charging. The batteries reach high temperatures while charging, increasing the cooling demand from the fan module compared to conventional cars. In this situation, no inflow is generated from driving and the fan is operating at high rotational velocities and pressure requirements.

When the (axial) inflow to the fan is non-uniform, (the velocity changes over the circumference), a varying force is generated on the fan blade, when it rotates. When this non-uniformity is stationary (constant in time), these force fluctuations are periodic, and this is the main cause of the tonal noise. The non-uniformities in fan modules arise from inflow distortions, like for example heat exchanger, duct bends, or the shape of the shroud.

In current fan modules, unequal blade spacing is used to reduce the annoyance of these tones. This reduces the noise at the Blade Pass Frequency, but introduces tones at other harmonics of the rotational frequency, overall mainly leading to a reduction in noise annoyance.

Flow obstructions have been shown an effective means of reducing noise in equally spaced axial fans with low Mach number, while minimizing aerodynamic losses. They introduce a secondary non-uniformity in the inflow, which creates a secondary aeroacoustic source on the fan blade. When placed at the correct circumferential angle, cancellation between the primary and secondary source is possible. This research investigates if such flow obstructions can still yield adequate noise reduction on unequally spaced fans, and if (multiple) upstream heat exchangers prohibit the working mechanism of flow obstructions.

It was found that flow obstructions can indeed significantly reduce tonal noise at the fan BPF, by up to 13 dB on the fan axis, and 6dB at an angle 45°from the axis. The upstream radiator and condenser did not compromise this reduction, and the obstruction still reduces noise when the fan operates at a lower rotational velocity. Using a superposition of obstructions (creating a multi-modal obstruction) could also control multiple tones. However, with the large number of tones to be controlled in an unequally spaced fan, the overall sound pressure attenuation and annoyance reduction are insignificant.

Furthermore, the low-fidelity analytical tool developed in the thesis was an effective means of rapid obstruction design and optimization. Although information on the fan's primary noise is needed, as well as some parameters to define the obstruction wake (which can be obtained with cheaper, RANS simulations), the model correlated well with simulation data obtained in PowerFLOW.

Contents

List of tables

List of figures

Nomenclature

In case of ambiguous symbols, the context in which they appear in the text should provide clarity as to which symbol is referred to.

Acronyms

Symbol	Description
(V)LES	(Very) Large Eddy Simulaton
BPF	Blade Pass Frequency
CFD	Computational Fluid Dynamics
CI	Confidence Interval
CPUH	Central Processing Unit Hour
CRFM	Cooling Radiator Fan Module
DFT	Discrete Fourier Transform
EU	European Union
EV	Electric Vehicle
FES	Fine Equivalent Surfels
FEV	Fine Equivalent Voxels
FFA	Far Field Analysis
FWH	Ffowcs Williams Hawkings
GCI	Grid Convergence Index
HVAC	Heating, Ventilation, and Air Conditioning
LBM	Lattice Boltzman Method
LPF	Lobe Pass Frequency
LRF	Local Reference Frame
OSPL	Overall Sound Pressure Level
PA	PowerACOUSTICS
PA	Psychoachoustic Annoyance
PM	Porous Media
PSD	Power Spectral Density
RANS	Reynolds Averaged Navier Stokes
RPM	Rotations Per Minute
SE	Standard Error
SPL	Sound Pressure Level
SQM	Sound Quality Metric
TNR	Tone-to-Noise Ratio
VR	Variable Resolution
WHO	World Health Organization

Dimensionless numbers

Symbol	Description	Definition
M	Mach number	$\frac{V}{c}$
Re	Reynolds number	$\frac{VL}{\nu}$

Greek symbols

Symbol	Description		Units
α	Angle of attack	–	$^\circ$
β	Velocity factor	–	$^\circ$
η	Efficiency	–	–
γ	Blade twist angle	–	$^\circ$
ν	Kinematic Viscosity	–	$\mathrm{m^2\,s^{-1}}$
Ω	Rotational frequency	–	$\mathrm{s^{-1}}$
Φ	Inflow angle	–	$^\circ$
ϕ	Observer angle	–	$^\circ$
ρ	Density	–	$\mathrm{kg\,m^{-3}}$
σ	Gaussian wake parameter	–	–
σ	Standard deviation	–	–
τ	Relaxation time	–	–
Θ	Obstruction width parameter	–	rad

Latin symbols

Symbol	Description	Units
A	Lobe amplitude	m
B	Blade number	–
C	Chord	m
c	Speed of sound	$\mathrm{m\,s^{-1}}$
D	Harmonic content rate	–
F	Force	N
f	Frequency	$\mathrm{s^{-1}}$
J	Ordinary Bessel function	–
K	Modified Bessel function	–
k	Wave number	–
L	Lift force	N
N	Frequency harmonic number	–
O	Overlap Coefficient	–
P	Power	W
p	Pressure	Pa
q	Flowrate	$\mathrm{m^3\,s^{-1}}$
q	Fourier pressure mode	–

R	Radius	m
r	Observerd distance	m
S	Sears function	–
t	Time	s
V	Fourier velocity component	$\mathrm{m\,s^{-1}}$
V	Number of stator vanes	–
v	Velocity	$\mathrm{m\,s^{-1}}$
W	Effective velocity	$\mathrm{m\,s^{-1}}$
w	Fourier force mode	–
M	Number of microphones	–
T	Temperature	K

Superscripts

Symbol	Description
eq	Equilibrium

Subscripts

Symbol	Description
c	Compressible
H	Hub
m	Wake velocity defect
p	Pressure
ref	Reference
r	Radial direction
s	Static
T	Tip

1 Introduction

With the continuous rise of environmental issues caused by fossil fuel transportation, the electrification of transport, particularly in the case of cars, has become increasingly imperative in recent years. Road transport is responsible for up to 24% of global emissions, and two-thirds of that originates from passenger cars.[1] With the European Union planning to ban the sale of all fossil fuel cars by 2035[2], the market share of electric vehicles will become larger and larger. This shift not only mitigates air pollution and reduces carbon dioxide emissions but also removes the dependency on finite resources fossil fuels offer, along with the benefits of being quieter, requiring less maintenance, and offering a smoother driving experience.

Although the switch from fossil cars to electric cars comes with a reduction in overall noise levels, it does have some downsides. With the removal of the noise from the engine, noises that were previously masked now become apparent. For example, Lennstrom et al [45], showed that high-pitched, tonal components in the gearbox are no longer masked by the sound of the engine. These tones led to severe annoyance and compromised cabin comfort. Aeroacoustic noise is another example of this 'unmasking'. Otto et al [61] showed that for a similar loudness (dB level of the noise) electric cars were experienced to be more annoying by a subjective evaluation compared to conventional vehicles.

Automotive fan noise

One noise source that has been an issue in the automotive industry for years, but has inflated with the rise of electrical vehicles is the sound created by the car's cooling fan. The purpose of the fan is to provide cooling airflow to a radiator and condenser, which together with the fan and a shroud make up the Cooling Radiator Fan Module (CRFM). The CRFM is situated in the front of the vehicle, right behind the grill, which is shown in Fig. 1-1 (picture taken from [3]).

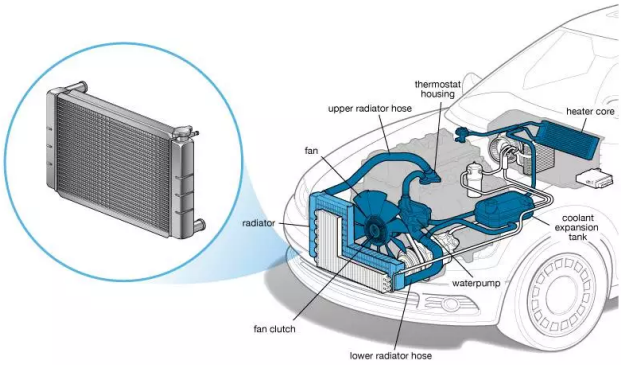

Figure 1-1 Location of CRFM

[1] European commision
[2] European Parliament
[3] cars.com

In normal driving situations, the airflow created by the driving wind is sufficient to provide the necessary cooling flow to the radiator/condenser. However, when driving slowly inside the city or in idle conditions, the fan is needed to generate this flow. Furthermore, in Electrical Vehicles (EVs), the batteries and other electrical components get hot during the charging process, resulting in larger cooling demands compared to conventional vehicles. In this situation, the fan has to operate at or close to the maximum duty cycle and will get noisy. This results in a nuisance for passing pedestrians and residents, especially near large charging stations with numerous cars. The tonal character of the noise results in a large annoyance [61]. Furthermore, brand perception is an important consideration for automotive companies, where any disturbing or weird noises during car charging can largely influence the perception of the brand that people have.

Although the noise from a single car fan is usually in the range of 60-80dB, which is not harmful on its own, the combined effect of multiple cars and the duration of the noise exposure are problematic especially in urban areas. According to a study by the World Health Organization (WHO), noise pollution is a widespread environmental problem that affects human health and well-being [60]. The European Commision even describes it as one of the biggest health risks in urban areas[4].

Noise reduction using flow obstructions

In recent decades, effort has been put into reducing the noise (annoyance) of automotive cooling fan modules. The noise spectrum of low tip-speed axial fans (like the automotive fan), is broadband superimposed with discrete (tonal) noise, of which the latter is perceived as especially annoying. This tonal noise is caused by periodic force fluctuations on the rotor blade. Those can exist due to for example the presence of stators or other stationary, non-uniformities in the flow. Reduction of this noise has been attempted by using, for example, resonators [59][69][35], or using an uneven spacing of rotor blades and stator vanes [20][17], effectively redistributing the tone.

Polacsek [71], and later Kota and Wright [44] tried using passive flow obstructions (in their case upstream rods) to introduce another non-uniformity into the flow. By placing this secondary non-uniformity in anti-phase with the primary, the blade force fluctuation of that particular order can be canceled, and the tonal noise reduced or eliminated. This was applied to low-speed axial fans (like automotive fans) by Gerard et al [32][31] (see Fig. 1-2), and numerically investigated by Moreau et al [57].

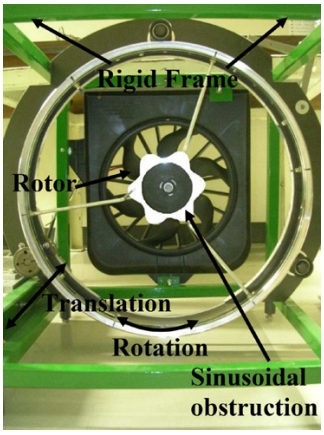

Figure 1-2 Flow obstruction investigated by Gerard et al [31]

They were able to show significant tonal noise reductions (order 10-15dB), while aerodynamic losses remained small (1-2%). This research aims to apply the concept of flow reduction to a current, industry-standard automotive fan. Especially the unequal spacing of blades (redistributing the BPF to more tones), as well as the upstream radiator and condenser, pose an uncertainty on the applicability of the concept.

[4] https://projects.research-and-innovation.ec.europa.eu/en/horizon-magazine/noise-pollution-one-biggest-health-risks-city-life

1.1 Thesis scope

Research objectives
The goal of this research can be divided into four thesis objectives:

1. **Understand the fan primary noise:** Numerical simulations using the commercial software PowerFLOW will be used to identify and understand the origin of the fan primary (tonal) noise.
2. **Develop low-fidelity tool to predict unsteady loading noise:** Since noise reduction using flow obstructions is based on fundamental aeroacoustic theories involving modal analysis, this tool should aid in understanding and optimizing noise reduction from flow obstructions. The equations are largely taken from the work of Gerard et al [32]. The model will be verified by comparing it to the aforementioned numerical simulations, taking it from a qualitative comparison tool to a quantitative tonal prediction model.
3. **Apply flow obstructions on current industry standard fan module:** Flow obstructions have thus far been applied to equally spaced fans where the number of tones to be controlled is limited. Furthermore, the application of fans with non-uniform stator spacing and upstream radiator+condenser has not been researched before.
4. **Validate results from low- and high-fidelity model experimentally, and compare them to literature:** The fan noise will be measured experimentally and compared to previous results, to validate if noise (reductions) can be accurately predicted with said methods. Furthermore, the results will be compared to the works of Gerard et al [31] and Moreau et al [57].

Research questions
Based on these objectives, two research questions are formulated, which are further divided in sub-questions. For the sake of brevity, 'fan configuration' in the research questions denotes a subsonic axial-flow fan featuring non-uniformly spaced rotor blades and stator vanes, downstream of an inline straight-fin radiator and louvered-fin condenser. This is a fan module configuration as found in the current industry standard EV.

1. **In what way can flow obstruction reduce the tonal noise of the fan configuration while limiting aerodynamic losses, and why?**
   (a) What are the dominant circumferential pressure modes in the far-field of the fan? Are these generated from rotor-stator interaction or a non-uniform inflow?
   (b) What obstruction geometry can generate the loudest, and most selective tone, while keeping the loss in flow rate minimal?
   (c) Do heat exchangers, in between obstruction and rotor, compromise the noise reduction from flow obstructions?
   (d) Does reducing a single acoustic pressure mode (identified in question 1.(a)), reduce the overall sound (annoyance) of the fan configuration, at different locations? How does that compare to the results from Gerard et al [31] and Moreau et al [57]?
   (e) Can a multi-modal obstruction control multiple tones?
   (f) Does an obstruction optimized for maximum duty cycle still reduce noise at lower fan RPM? Is this in line with the findings of Goth et al [36]?
2. **Are the assumptions in the model proposed by Gerard et al [32] valid on the fan configuration?**
   (a) Is it possible to model the wake of a flow obstruction using a Gaussian filter, when upstream heat exchangers are present?
   (b) To what accuracy can a 1D Sears gust approach predict the unsteady blade loading caused by a non-uniform inflow?
   (c) When the force fluctuation of the rotor blades is known, can the far-field tonal noise be predicted (within 3dB accuracy) using the rotating dipole theory? Also for unequally spaced blades?

Thesis structure
Firstly, Chapter 2 considers the theoretical background. The aerodynamics and noise sources for fan modules are discussed, as well as the academic literature on flow obstructions. Next, Chapter 3 describes the methodology of the thesis, which is divided into an analytical, numerical, and experimental part. A mesh convergence study on the numerical results, together with the verification of the analytical model and validation using experimental results is discussed in Chapter 4. This leads to the description and discussion of the results in Chapter 5. Finally, a discussion on how these results compare to literature, along with the conclusions and recommendations from the thesis are presented in Chapter 6.

2

Theoretical background

This chapter will summarize the theoretical background needed to comprehend the motivation and content of this study. In Section 2.1, the function of the fan module in its subsystem is explained along with the necessary aerodynamic background knowledge, followed by a description of the critical operating conditions. Next, in Section 2.2, the main aeroacoustic noise sources that are observed in automotive fans are elucidated. Following that, in Section 2.3, metrics for the assessment of fan noise are investigated, taking into account the annoyance of the sound to humans. Then, in Section 2.4, the design of the current industry standard fan is investigated, focusing on readily implemented noise suppression strategies. Finally, in Section 2.5, the working mechanism of flow obstructions is explained, and the previous research on flow obstructions is summarized.

2.1 Heat management, aerodynamics & operation

In this section, the purpose of the fan module in the heat management system will be explained in Sec. 2.1.1. The aerodynamic working mechanisms and definitions, like pressure rise, flow rate and efficiency will be touched upon in Sec. 2.1.2. The critical operating point with regards to noise nuisance is also defined.

2.1.1 Heat management system

An electric car heat management system can be subdivided into two distinct parts: the cooling system and the HVAC (Heating, Ventilation, and Air Conditioning) system. The former ensures the temperature of the battery, electric motor, and other electronic components stays within their operating regime. The latter controls the cabin temperature and humidity inside the cabin, ensuring a comfortable environment for passengers.

A simplified overview of these subsystems is given in Fig. 2-1 below (pictures are taken from [1]). Note that the cooling system is for a petrol car, for an EV the battery would also have to be cooled.

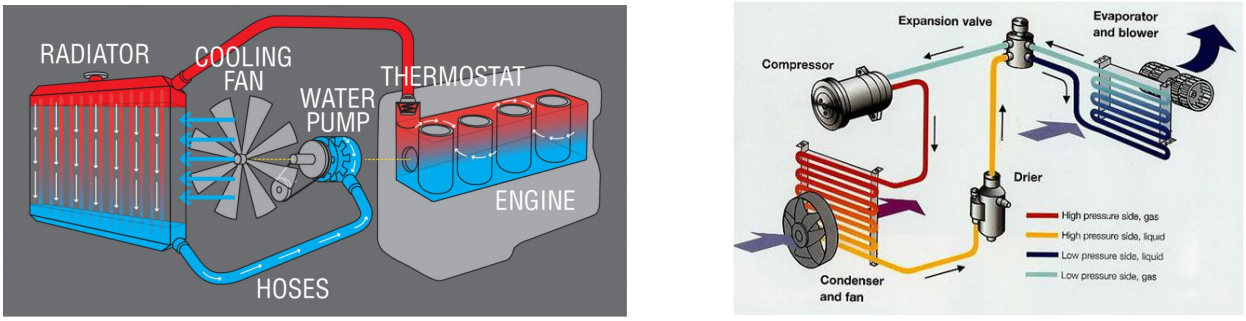

(A) Cooling system (simplified)

(B) HVAC system

Figure 2-1 Heat management systems

[1] Cooling system and HVAC system

The radiator (cooling system) and condenser (HVAC system), are responsible for cooling the coolant liquid and refrigerant of their respective subsystem. This is achieved by the convection of cool air through the condenser/radiator, removing heat from these components. The radiator and condenser are therefore strategically placed in the same position at the front of the vehicle. When driving, air can enter through the front grille cooling these components. When the car is driving slowly or idle, a fan is necessary to generate this cooling flow. This fan is placed downstream of the radiator/condenser (puller fan). The combination of the radiator, condenser, fan, and shroud is called the Cooling Radiator Fan Module (CRFM). Renders of such a module are shown in Fig. 2-2 below. This is the CRFM from one of the NIO cars, which has been used throughout the thesis.

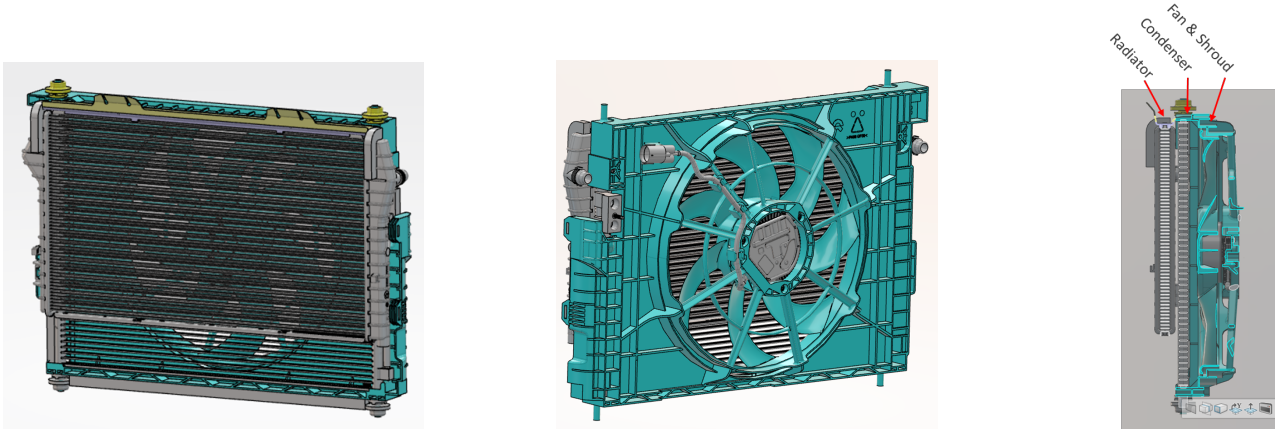

(A) Isometric front view (B) Isometric rear view (C) Side view

Figure 2-2 Cooling Radiator Fan Module

2.1.2 Aerodynamics & operation

The aerodynamic requirements for the axial fan are twofold, explained by Sortor [78]. Firstly the velocity requirement (airflow requirement): the fan has to supply sufficient cooling airflow to the radiator/condenser, even in idle condition. Secondly, the fan has to supply a pressure rise to overcome the pressure drop imposed by obstructions, including the radiator, condenser, but also the inlet grill and engine block. Since the velocity requirement is large compared to the pressure requirement (large volume of air to a large area), together with the space requirement in the front of the vehicle, the choice of an axial fan as opposed to a centrifugal fan is sensible. [2]

Fan performance curve

The performance of the fan (pressure rise and flow rate) have to match with the system it is operating in. This is usually characterized with the P-Q curve (performance curve, characterizing the fan), and the system resistance/impedance curve. An example of these curves is given in Fig. 2-3.[3]

[2] URL: https://www.cuidevices.com/blog/axial-fans-vs-centrifugal-fans-what-is-the-difference
[3] URL:https://techcompass.sanyodenki.com/en/training/cooling/fan_basic/007/index.html

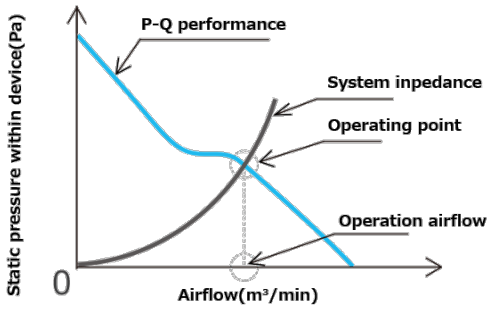

Figure 2-3 PQ-curve and system resistance

As can be seen in the figure, the system resistance follows a quadratic relation with massflow. The ideal operating point of the fan (maximum efficiency, this will be expanded upon later) is annotated in the figure. Just left of the operating point, a kink can be seen in the P-Q curve, which marks the onset of stall. Moving further onto the left of the performance curve, the pressure requirement is too big for little massflow, causing the angle of attack to increase and eventually leading to stall. For a properly designed system, the system impedance will cross the performance curve at the operating point, as is the case in the figure. The point all the way to the left of this curve is referred to as the shut-off condition, whilst the point on the far right is the free delivery condition, where no blockage is present at all.

Efficiency and noise

The efficiency of an axial fan is defined as the useful output power divided by the input power, where the output power is the product of the airflow and pressure increase of the fan [4]:

$$\eta = \frac{\Delta p_s q}{P} \tag{2-1}$$

In this equation Δp_s is the static pressure increase, q the airflow and P the input power, which is usually obtained from the product of the fan voltage and current. The efficiency of an axial fan therefore depends on the operating point of the fan. This is shown in Fig. 2-4a. In this figure the PQ-curve is plotted along with the efficiency, and it can be seen where the fan operating point should be.

Similar to how the efficiency changes with the flow rate of the fan, the aeroacoustic noise produced by the fan does as well. An example of how the noise varies with the operation point is shown in Fig. 2-4b. As can be seen in the figure, the maximum noise is found near shut-off condition, whilst a minimum exists (region b in the figure).

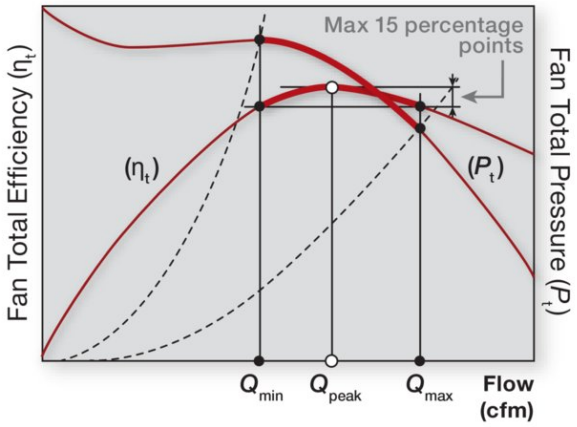

(a) Efficiency curve and PQ-curve [40]

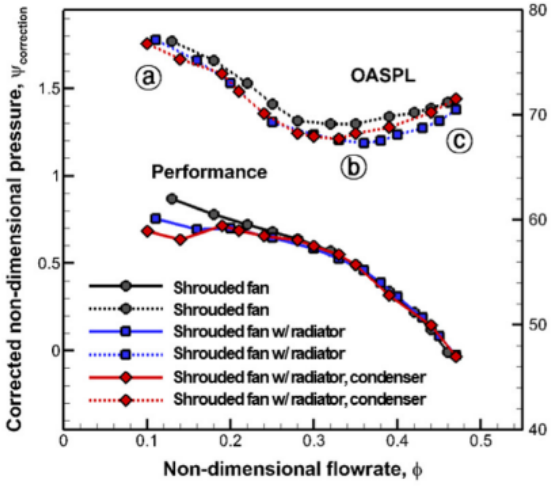

(b) Noise and PQ-curve [65]

Figure 2-4 Efficiency and noise on PQ-curve

[4] URL: https://www.engineeringtoolbox.com/fans-efficiency-power-consumption-d_197.html

Mellin [52] showed, however, that the peak efficiency and the lowest noise level of the fan do not necessarily coincide. In the aeroacoustic design of the cooling fan, bringing the peak efficiency and minimum noise closer together should therefore be a priority. This can be achieved by changing design variables like pitch angle, camber, and chord length [52]. Longhouse [46] furthermore showed that using a rotating shroud (which will be elaborated in Section 2.4) was effective in shifting these points closer together.

Critical operating point
This study focuses on the aerodynamic noise of an CRFM module. The main noise disturbance of the fan module in EV's is during the charging process: the battery and electronics get hot while no flow is generated from driving. In this condition, the radiator requires a cooling power of around 12kW to cool the batteries, depending on the ambient conditions, which influence the heat transfer coefficient. Cars are charging in urban areas, where the fan noise can lead to annoyance for pedestrians and residents, especially if multiple cars are charging at the same time. The operating point that is studied in this thesis is, therefore, toward the left of the PQ-curve, where the flow rate is low. Usually, fans will be designed for this condition, however, and it can be expected that the fan is not operating in stall condition. In simulations and tests throughout this thesis, no inflow is present, to resemble the operating point mentioned above.

2.2 CRFM Noise Sources

Axial fans/compressor noise has been researched since the 1960's by Sharland [76]. He determined that axial fans have a combination of tonal and broadband noise, attributing the former to rotor/stator interaction and the latter to blade trailing edge noise. However he also observed an increase of noise with increased inflow turbulence. He also showed that the noise is dipolar, scaling with M^6. Longhouse [47] focused his research on low tip-speed axial fans (of which automotive fans are an example), and he showed turbulence ingestion and inflow disturbance, as well as blade tip clearance noise are significant noise contributors. A recent review study on fan noise mechanisms and reduction strategies by Neisse [58], summarizes the current understanding of the noise sources present in axial fans. An overview of those was adopted from his paper by Allam and Abom [3], and is shown in Fig. 2-5 below.

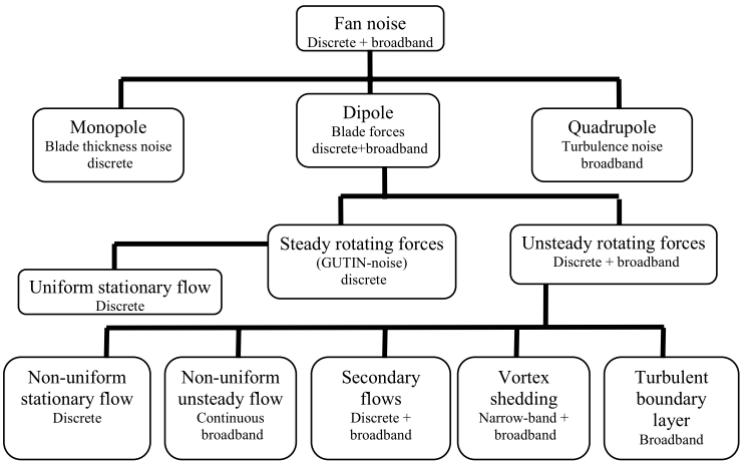

Figure 2-5 Overview of noise sources [3]

As shown in the figure, the noise from axial fans is mainly dipolar noise, caused by loading (forces) on the blades and shroud/stators. Blade thickness noise is caused by the displacement of air by the fan blades, causing a monopolar radiation pattern. Thickness noise has long been studied for propellers by eg Demming [14], but is a weak radiator of sound for low Mach number fans (for automotive fans, $M \approx 0.15$), having thin blades and a low solidity, shown by for example Caro [10]. Turbulence causes broadband noise by itself, responsible for the quadrupole noise. However, this is much lower than loading noise at low Mach number, as it scales with M^8.

So, the noise sources that are observed in axial fans are all dipole sources. An example of a typical automotive fan noise spectrum, with the different sources annotated is given in Fig. 2-6 below:

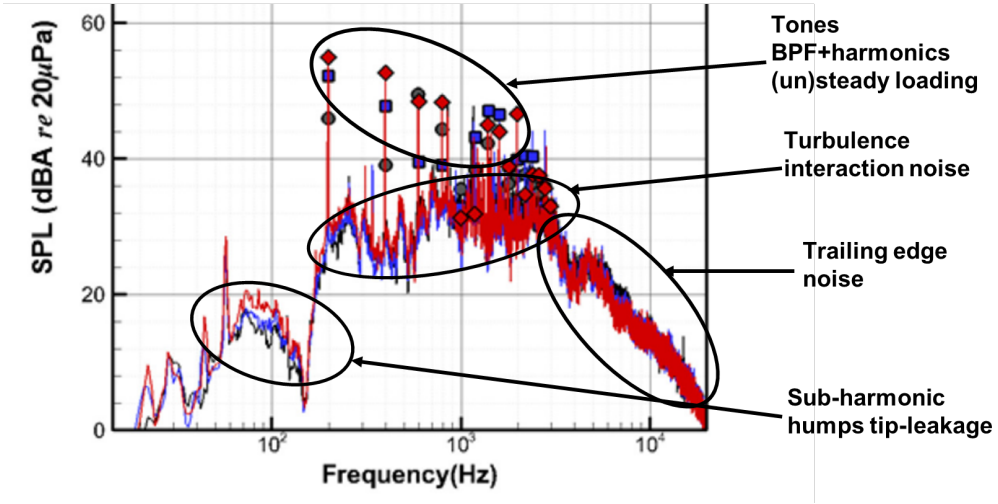

Figure 2-6 General occurrence of noise sources, annotated from [65]

In the next subsections, these sources will be elaborated upon. They are divided into the tonal sources ('discrete' in Fig. 2-5), given in Sec. 2.2.1, and broadband sources, in Sec. 2.2.2. Note that only the noise sources that are observed in current automotive fans specifically are discussed, a more general overview is given in the literature study [27].

2.2.1 Tonal noise sources

Discrete noise is generated at the Blade Pass Frequency (BPF) and harmonics, due to blade loading. This noise source can be divided into steady loading noise, and unsteady loading noise: periodic noise generated from a stationary, non-uniform inflow. These two sources are explained separately below.

Steady loading noise
Gutin [37] investigated the noise generated by propeller blades in steady loading, and derived an equation to model pressure fluctuations. In this model he assumes high Mach number blades and uniform, steady, symmetric inflow. This type of noise is often referred to as Gutin noise in literature. He found that the fundamental frequency of the radiated sound was the product of the number of blades and the rotational frequency; the Blade Pass Frequency (BPF). This sound source is a result of the blade-induced pressure fluctuations on a stationary reference point. The amplitude and directional characteristics (a dipole with it's zero on the fan axis) of his model (based on fundamental aerodynamics and acoustic analogies), correlated well with experimental data obtained by Paris [63] and Kemp [43]. This sound source is inevitable for any fan/propeller/compressor doing work since it is related to the thrust/torque. Ways to reduce steady loading would mean reducing the blade force, which can be achieved by using more blades or a larger fan diameter. In automotive fans, however, steady loading is usually dominated by unsteady loading, since the Mach number is relatively low. Wright [83] showed that force fluctuations with magnitudes smaller than 0.1% of the steady loading can still dominate steady loading in low-speed axial fan applications. Tones generated by steady loading show a decay over the harmonics as shown in Fig. 2-7a.

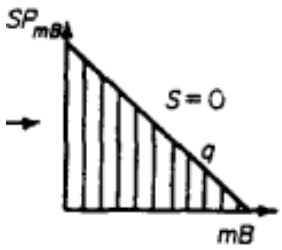

(A) Tones generated by steady loading [84]

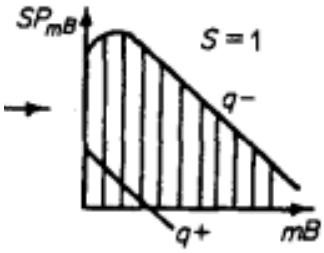

(B) Tones generated by unsteady loading order $S = 1$ [84]

FIGURE 2-7 Steady and unsteady loading discrete noise spectra

Unsteady loading noise

When the inflow to the rotor is non-uniform (but still stationary), unsteady, periodic forces are generated on the blades: in the reference frame of the fan, the inflow is now unsteady. These unsteady force fluctuations can generate tones of much higher magnitude compared to steady loading, especially for low Mach number rotors. This was first observed experimentally by Fileul [23] and Doak et al [16], who saw that Gutins model under-predicted tones significantly.

Unsteady loading noise is usually analyzed in the frequency domain since it is periodic in nature. The first to develop a model to calculate noise from asymmetrically loaded rotors was Wright [84], who used a modal approach: the force fluctuations can be spatially decomposed into azimuthal modes with order w, which radiate sound at discrete tones, being multiples of the BPF:

$$q = nB \pm w \tag{2-2}$$

In this equation, q are the rotating (azimuthal) pressure modes, Fourier components of the far-field pressure field. n is the harmonic number (Fourier time mode), hence $n = 1$ corresponds to BPF, with B the number of blades, and w is the harmonic blade loading number (Fourier force mode/space domain). For a given w, a q_- and q_+ mode exists. These modes rotate at velocities not necessarily equal to the rotational velocity of the fan. The rotational speed of a mode is given by:

$$\Omega_q = \frac{nB\Omega}{q} \tag{2-3}$$

In this equation, Ω is the fan rotational frequency, and Ω_q is the mode rotational frequency. When $w = 0$, the two modes overlap and rotate with Ω, and this is the steady mode (the noise equations converge to Gutin's results).

Two examples of these rotating modes are given in Fig. 2-8 below. The direction and velocity of rotation is indicated, following Equation 2-3, witth $n = 1$ and $B = 7$ (this is on the BPF).

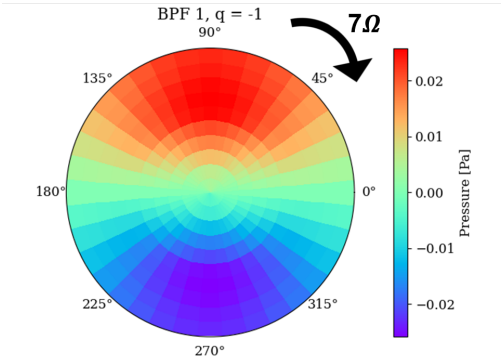

(A) Pressure mode -1

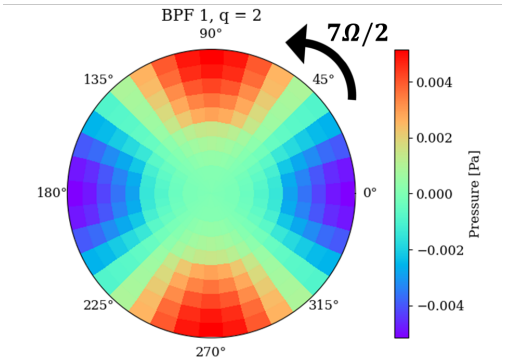

(B) Pressure mode +2

FIGURE 2-8 Visualization of rotating pressure modes

Wright found that the radiation strength of these modes is correlated to the rotational frequency of the mode. Following Equation 2-3, the rotational velocity of the q_- modes is higher and therefore dominates over the q_+ modes. It reaches infinity when $nB = w$, which is therefore the most effective radiating mode. Infinite rotational velocity practically means the dipoles from each blade are in phase, and this mode, therefore, radiates like a symmetric dipole with maximum along the rotational axis, a plane wave. All other modes, with $w \neq nB$ are 'spinning modes', and have zero contribution on the axis [81]. These modes can be dominant when radial or tangential force fluctuations are significant in the rotor plane [30].

The noise spectrum generated by a certain mode $w = 1$ (s is used in some references, like the one where the diagram is taken from), is shown in Fig. 2-7b. This shows that a force mode s contributes to each harmonic n, but is especially high close to the harmonics for which the resulting pressure mode q is (close to) zero. Since the q_+ modes are dominated by q_- modes, they are often ignored.

In an automotive fan, asymmetrical positioning of the radiator/condenser, along with the transition from a rectangular grill/shroud to a round fan are examples of non-uniformities in the inflow. Examples of this are shown in Fig. 2-9. Furthermore, backflow at the top and bottom part of the shroud can cause non-uniformites, which can be seen in both Fig. 2-9a and Fig. 2-9b.

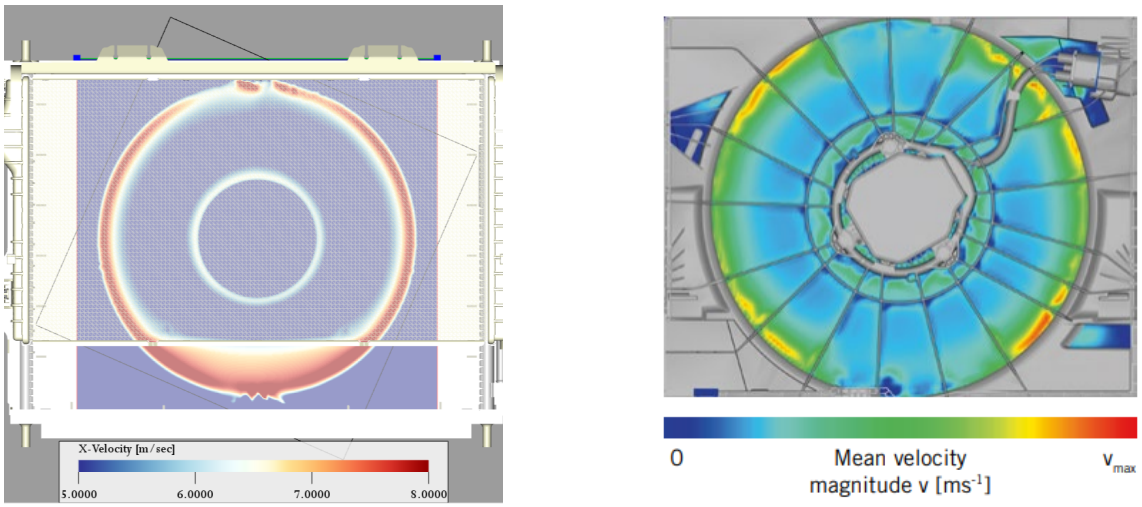

(A) Non-uniformity due to radiator

(B) Non-uniformity due to shroud transition[34]

Figure 2-9 Examples of flow non-uniformities

Furthermore, installed in the car, duct bends resulting from the transition of the inlet grill to the CRFM module can introduce non-uniformities. Finally, downstream objects like the stator vanes or engine can have a potential effect on the upstream flow through the rotor.

Rotor/stator interaction noise

Aside from the effect on the rotor by the potential field of stators, the wake of the rotors can also produce unsteady loading on the stator vanes, resulting in another interaction noise, pointed out by for example Lowson [48]. Since the number of stators is often different from the number of rotors, this noise is usually created by different (azimuthal) lobe modes and hence generates sound at different orders of the rotational frequency. This was shown by e.g. Duncan and Dowson [19], and more recently by Peng et al [67]. Modal analysis of (unevenly spaced) rotors and stators is an effective tool for reducing and redistributing discrete frequency noise along the spectrum. Tyler and Sofrin [82] found that the modes at which rotor-stator interaction noise is significant can be found with Equation 2-4, which is an adaptation of Equation 2-2.

$$q = nB \pm kV \tag{2-4}$$

In this equation, V is the number of stator vanes and k is an arbitrary integer. In modal analysis, modes resulting from rotor-stator interaction are referred to as 'Tyler-Sofrin' modes.

2.2.2 Broadband noise sources

As mentioned previously, the tonal content described in the previous subsection is superimposed on a broadband noise spectrum. Three distinct mechanisms cause the broadband noise: turbulence interaction noise (leading edge noise), turbulent boundary layer trailing edge noise (airfoil self noise/trailing edge noise), and noise from tip leakage/backflow. Which of these sources dominates is dependent on the specific system (inflow turbulence, tip gap size etc.), as well as the operating point and frequency [56][88][7].

Caro and Moreau [10], focused on the relevance of inflow turbulence, interacting with the rotor blades, as well as acoustic waves shed from the blade trailing edge due to Kutta condition; referred to as Fukano's self-noise in their study [26]. These two mechanisms are similar to widely studied airfoil noise sources: turbulence interaction noise and turbulent boundary trailing edge noise. The two are shown in Fig. 2-10.

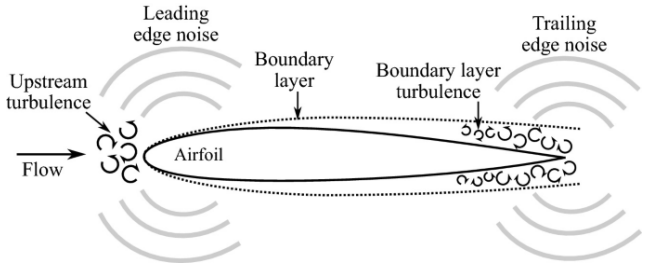

Figure 2-10 Airfoil noise sources (from [18])

Turbulence interaction noise
When a turbulent eddy or upstream gust reaches the leading edge, the random (velocity) fluctuations will create an unsteady pressure on the airfoil surface. This unsteady pressure results in an unsteady lift (loading), which is a source of (dipolar) noise. The phenomenon was investigated by numerous authors. Notably Paterson and Amiet [66] and later Moreau and Roger [55] showed that noise is especially dominant at low frequencies.

Amiet developed a model to calculate noise radiation from this source [4][6], showing that the radiation pattern depends on the acoustic compactness of the airfoil.

Turbulent boundary layer trailing edge noise
Airfoil self-noise is the noise created at the trailing edge of an airfoil in a turbulent boundary layer. Turbulent eddies of different sizes result in surface pressure fluctuations on the surface of the airfoil. The source is most notably investigated by Amiet [4].

Fukano described the source as vortex shedding at the trailing edge, causing the lift coefficient to vary, resulting in broadband noise. Fukano found that the wake width at the trailing edge (sum of blade thickness and boundary layer displacement thickness) was one of the controlling factors for fan broadband noise.

Tip leakage flow
Longhouse [46] investigated tip clearance noise in detail. He found an increase in broadband noise with larger tip clearance and suspected that the blade tip vortex interacted with the blade trailing edge and the next blade leading edge. The effects of tip clearance have since been extensively studied (by e.g. Fukano et al[25],[41],[24], Kameier and Neisse, [42], Magne et al [50], and Zhu and Carolus [90],[91]), and is well-understood. Due to an inevitable clearance between the blades and shroud, a gap will exist at the tip of the rotor. Due to the pressure difference between the pressure and suction side, an airflow through this opening will be created. This is flow going from the pressure side (back side) to the front of the rotor (suction side). Hence, outside of the ring, a negative axial velocity is present. Since on the inside of the fan ring, a positive axial velocity is present, a rotation is created around the fan ring. Now since the rotor has an azimuthal velocity, the vortex that is created will start rotating in the direction of the blades but at a lower azimuthal velocity (30% of tip velocity was found by Zhu et al [91]. A visualization of this rotating vortex is shown in Fig. 2-11.

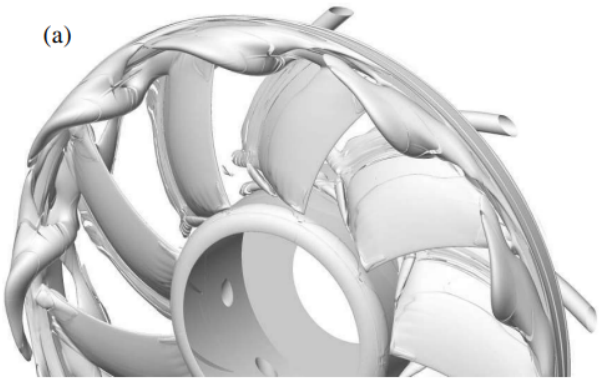

Figure 2-11 Tip leakage vortex [54]

This vortex will interact with the blades, will increase broadband noise, and introduce humps in the spectrum at frequencies below the BPF. They cause humps due to the spread in the rotating frequency of the vortices [91]. The effect of this noise source tends to be more dominant at low flow rates since the pressure difference, in this case, is higher. Nevertheless, the phenomenon has also been observed at design conditions.

2.3 Noise assessment and annoyance

Noise levels are characterized in Sound Pressure Level (SPL), measured in dB, which is a function of frequency and is calculated using Equation 2-5:

$$SPL = 10log_{10}\left(\frac{p_{rms}^2}{p_{ref}^2}\right) \tag{2-5}$$

Where p_{rms} is the root mean square of pressure fluctuations, and p_{ref} is a reference pressure of $2 * 10^-5Pa$, the threshold level of human hearing. Sound is assessed in the frequency domain. Humans can hear sounds with frequencies between 20Hz and 20 kHz, so this is the maximum range of interest.

However, SPL does not automatically reflect how the human perceives the sound. One measure that is commonly used is weighing, where the spectrum is weighted according to how humans perceive it. This comes down to scaling down lower frequencies, as higher frequencies are perceived as more annoying. Examples of weighting are shown in Fig. 2-12, of which A-weighing is the one most commonly used in the automotive industry.

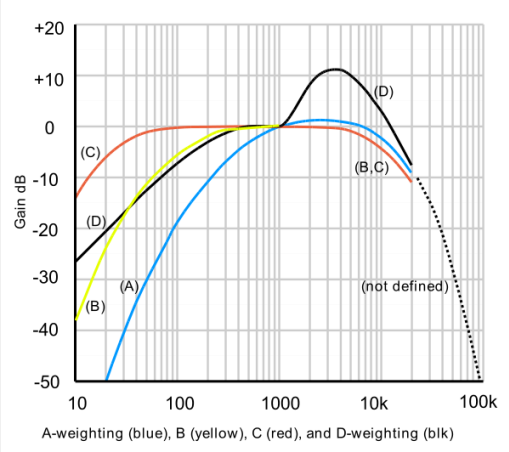

Figure 2-12 Weighing of noise [5]

It is convenient to get a single-value sound level metric (at a certain location), to compare different designs

quantitatively. Usually, the Overall Sound Pressure Level (OSPL) is used for this. This is a logarithmic sum over the entire audible frequency range of the (A-weighted) SPL spectrum.

Tonality
Still, OSPL does not always reflect the noise annoyance well. Psychoacoustics aims to quantify noise nuisance based on Sound Quality Metrics (SQM). The most common SQM's are: loudness, sharpness, fluctuation strength, roughness and tonality [74]. The difficulty with these metrics is that no universally agreed-upon definition is present, and standardization is lacking. The best-known Psychoacoustic Annoyance (PA) metric, combining different SQM's was established by Fastl and Swicker [22], and has been adapted by Di et al [15], as well as Schneider and Feldmann [74], to also include tonality.

In automotive fans, the annoyance mainly comes from the high tonality of the noise. Anghinolfi et al [8] did an optimization of blade spacing with solely tone-to-noise ratio (TNR) as a psychoacoustic minimization metric. Tone-to-noise ratio is the amount a tone stands out from the broadband spectrum, measured in dB. It is a quick and fair way to compare the annoyance due to tones. Furthermore, the focus of the thesis is to reduce tonal noise, and no significant changes to the broadband noise is expected.

Therefore, in this thesis, the OSPL and summed TNR will be the integral quantities used to compare and judge design options and results.

2.4 Industry standard

In this section, the design of a current industry standard fan module will be investigated. The focus will be on a few noise suppression mechanisms that have shown to be successful in the literature and have therefore been implemented. See also Fig. 2-2 for an overview of the fan studied in this thesis.

Ring fan
Noise from tip leakage (Sec. 2.2.2) can be effectively reduced by using a ring at the outer radius of the blades. Longhouse [46] was the first to find this and called it 'rotating shrouds'. This ring reduces the roll-up of vortices and by doing so reduces tip noise significantly. Rings are now nearly always used in automotive fans, and the tip gap between the ring and shroud is minimized in design. This is usually restricted by mechanical vibrations of the fan, where a clearance ensures the fan does not hit the shroud. For the fan in this thesis, the tip gap is 5mm.

Blade and stator vane spacing and numbering
Since the main source in an axial fan occurs at BPF, research has been conducted on altering the spacing and numbering of the blades to cancel out pressure fluctuations. For an evenly-spaced rotor, the period of pressure fluctuation caused by a passing blade is constant. Therefore, the tonal peaks each of the blades creates are basically in phase and constructively interfere at the BPF. By introducing uneven spacing, the BPF and harmonics can be significantly reduced, since now some destructive interference takes place. However, tones at all other harmonics of the rotational frequency are introduced. Since tonal noise is perceived as more annoying, spreading out the noise over different frequencies is desirable in terms of annoyance. An example of uneven spacing is shown in Fig. 2-13a, with the resulting differences in the spectrum demonstrated in Fig. 2-13b.

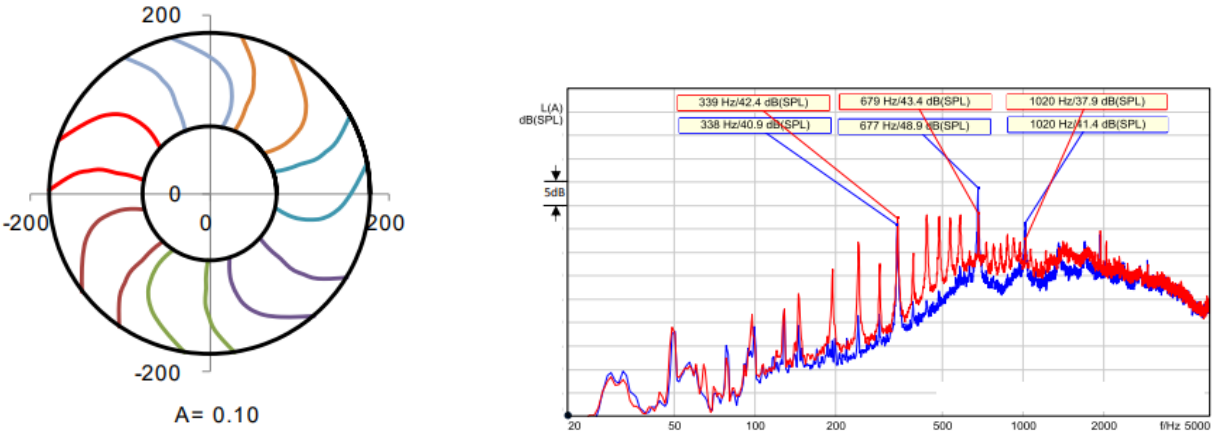

(A) Uneven blade spacing [68]

(B) Spectrum for even (blue) vs uneven (red) blade spacing [68]

FIGURE 2-13 Uneven blade spacing

Numerous authors focused on optimizing blade spacing in terms of annoyance or OSPL. Well-known examples are the works of Ewald et al [20], Duncan and Dawson [19], and Dobrzynski [17]. In most of these optimization, the blade forces are assumed independent of spacing, whereas Wu [86] applied a correction on the force fluctuation depending on the distance to the previous blade. Anghinolfi [8] showed that to achieve significant reductions on the BPF, relatively large angular differences are needed ($> 30\%$ of mean angular spacing). In spacing design, proper balancing of the fans inertia has to be taken into account, which limits the degrees of freedom.

In terms of blade numbering, often prime numbers of blades are chosen. In this way the constructive interference of blades at certain multiples of the rotational frequency is limited. The fan in the current study has 7 blades, which are unevenly spaced. The angles vary between 47 and 55 °.

It was furthermore shown by for example Peng et al [68] that uneven spacing of stators can also reduce tonal noise. This effectively spreads out the force fluctuations over multiple force modes. Normally a different number of stators and rotors is also employed, to avoid the strong radiating mode $q = nB$, as explained in Sec. 2.2.1. The fan in this study has 9 stator vanes with an unequal spacing.

Blade sweep

Blade sweep has been applied to fans for numerous reasons. As was shown by Corsini et al [12] and Herold et al [39], it can delay stall, ensuring a larger operating regime. It can furthermore reduce broadband noise levels, by effectively redirecting streamlines along the blade [64], which is shown in Fig. 2-14.

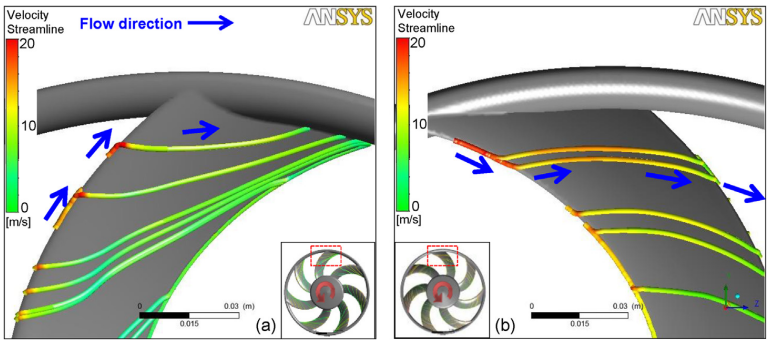

FIGURE 2-14 Velocity streamlines backward and forward sweep [64]

Backward and forward sweep has been shown to reduce noise by Park et al [64] and Zenger and Herold [87][39]. Which of the two works better is not entirely conclusive. At design condition, all authors found forward sweep to reduce the noise most. However, forward sweep is more susceptible to inflow turbulence; the noise increase is larger in this case. On the fan module studied in this thesis forward sweep is used.

2.5 Noise reduction using flow obstructions

In the antecedent literature study of this thesis [27], the noise reduction mechanisms researched in the past were assessed and reviewed in an extensive comparison study. A trade-off that took into account the following criteria was then performed: noise reduction potential, design intrusiveness (is the design retrofittable or does the entire fan (module) have to be altered), the aerodynamic penalty, and the research potential (are there identifiable research gaps).

From this trade-off, the concept of flow obstructions was found to be the winning concept. The relatively large tonal noise reductions for a small aerodynamic penalty made it an attractive design option. Furthermore, the fact that these obstructions are retrofittable is a large advantage in the context of this thesis. Finally, the application of the concept on current industry standards, where fan modules have upstream radiators and condensers, and an unequal spacing of stator vanes and rotor blades is new, showing the concept has research gaps to be filled.

2.5.1 Working mechanism

The concept of flow obstructions is to place an obstruction of a particular shape (examples shown in Fig. 2-15) upstream of the fan (and possibly radiator), having a certain number of periodic occurrences in the circumference N: in the example figure $N = 6$. (for sinusoidal obstructions this number is referred to as the number of lobes)

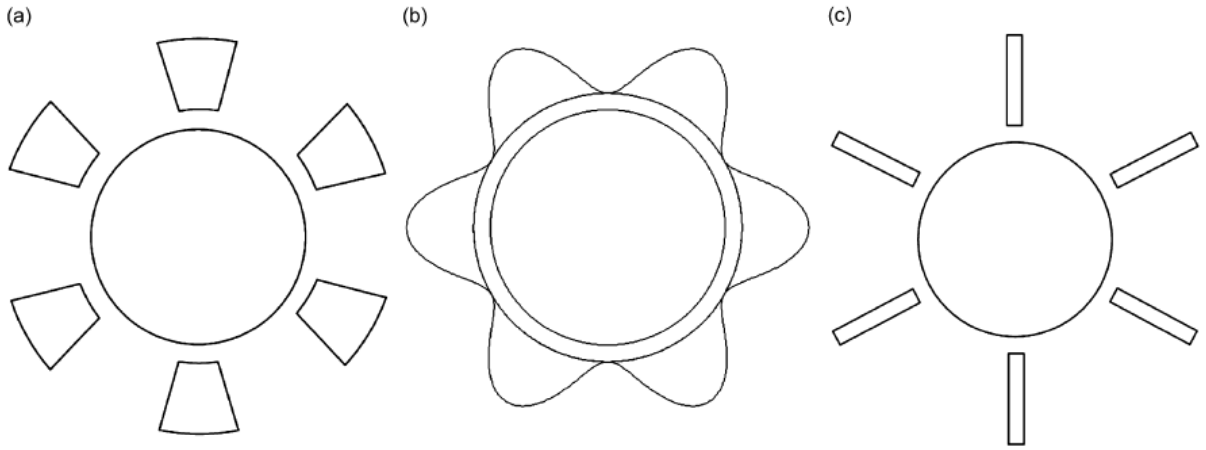

Figure 2-15 Examples of flow obstruction shapes [32]

The purpose of the obstruction is to generate a harmonically selective wake. In the reference frame of the fan, this non-uniform wake imposes a force fluctuation of Fourier order $s = N$ on the blade. By placing the obstruction in anti-phase with the primary non-uniformity in the inflow, the unsteady force fluctuation of that particular order can be eliminated, and the corresponding pressure modes (noise) with it.

As was explained in Sec. 2.2.1, the main noise contributor (away from the rotor plane) at BPF and harmonics is the pressure mode 0, which arises from a force fluctuation of the order $s = nB$, hence the number of blades of the rotor for BPF1. The obvious choice is therefore to design an obstruction with the number of lobes equal to the number of blades of the rotor. However, resulting from radial or tangential force fluctuations, or rotor-stator interaction modes (Tyler-Sofrin modes), other pressure modes can also be dominant [81] and this has to be studied on a case-to-case basis.

2.5.2 Previous work

Polacsek [71] was one of the first to use obstructions. He used cylindrical rods to reduce fan tonal noise from rotor-stator interaction by 6dB. Kota and Wright [44] applied it to a ducted fan, controlling up to three different duct modes. Farrell[21] patented a slightly different approach. Instead of using an upstream obstruction, he varied the inner radius of the shroud to create a sinusoidal loading.

Goth et al [36] tested both centrifugal and axial fans for industrial applications. They tested multiple obstruction shapes where the obstruction is on the outer radius. The most effective was sinusoidal, as shown in Fig. 2-16.

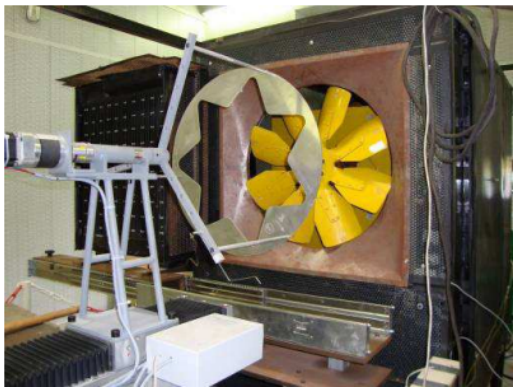

Figure 2-16 Obstruction used in [36]

They managed to reduce the peak at BPF by 10dB, resulting in an OSPL decrease of 1.8dB. They furthermore showed that at optimal position (distance obstruction to fan and relative angle of the obstruction), noise reductions are seen for a large range of RPM's. Only when going below 55% duty cycly, they started seeing minor noise increases, but in this regime noise is a lot lower. It should be noted the obstruction did yield a loss of flow rate, compensating for this flow rate would result in a 0.9 dB(A) noise increase. In short, the overall noise attenuation in this paper was limited. However, with little understanding of flow mechanisms and potential obstruction shape improvements, more reduction is realistic. Furthermore, with the decrease in tonal character, the noise annoyance is likely larger than the overall sound pressure suggests.

Perot et al. [70][62] successfully applied obstructions at the outer radius to centrifugal fans, both numerically and experimentally. In general, obstructions at the inner radius are more convenient in axial fans, whereas the outer radius can be used in centrifugal fans [54].

Gerard et al [28][29][32][31][30] conducted a series of research focused on flow obstructions in low-speed axial fans. Some papers even focus on automotive fans. Whereas most research regarding obstruction was experimental, in [32], the authors develop an analytical model to estimate the noise from obstructions qualitatively. The purpose of this work is to design harmonically selective obstructions, that have a low harmonic content rate. The approach is therefore left qualitative. This approach is adopted and further developed in this thesis, so will be explained in more detail in Section 3.1.

The authors then experimentally investigated obstructions in [31]. They validated the model by measuring the harmonic content rate indirectly. Furthermore, they showed the distance obstruction to fan can influence the relative noise attenuation at the upstream and downstream half-space. Finally, they also tested the aerodynamic performance of the fan (pressure, flow rate, and efficiency) along the PQ curve and saw less than 1% loss of efficiency in all measured points.

In the aforementioned papers, obstructions with $N = B$ lobes were used, to target pressure mode 0 at the BPF. As explained in Sec. 2.2.1, this is the dominant radiator of sound, especially on the rotor axis. However, when tangential and radial force fluctuations are significant, other modes can be dominant as well, especially in the rotor plane, away from the axis. This is usually pressure mode 1 or -1, hence the lobe numbers are $B + 1$ or $B - 1$. In [30], the same authors therefore attempted to combine two obstructions into one, multi-modal obstruction, by simply superimposing the cosine waveforms. This is shown in Fig. 2-17.

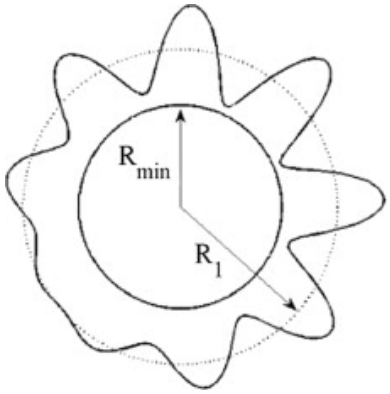

Figure 2-17 Multi-modal obstruction [30]

They showed that this is indeed possible, achieving larger noise reductions in the whole-space. The authors state it is possible to extend this to even more modes and also different tones, although aerodynamic penalties might become a larger concern.

In [29], the same authors developed a method to position the obstructions for maximum noise attenuation using a beat effect, by rotating the obstruction and analyzing the Hilbert transform of the band-pass filtered time signal. This approach was then used by Moreau et al [57] to come up with a numerical optimization procedure for obstruction design in PowerFLOW. He demonstrated the approach by eliminating the noise from rotor-stator interaction (with equal rotor blade and stator vane number) in a laboratory setting, both numerically and validating it with experiments. This is shown in Fig. 2-18.

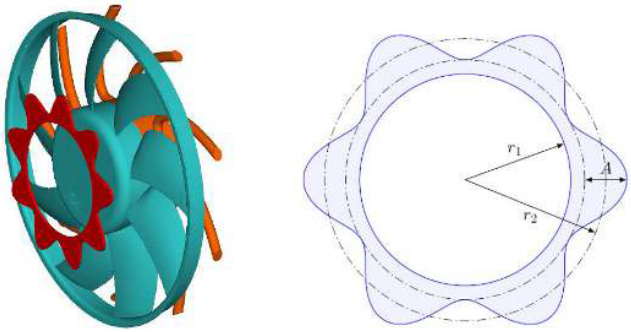

Figure 2-18 Sinusoidal flow obstruction [57]

3

Technical approach

In this chapter, the methodology of the thesis will be outlined. The approach consists of three main parts. In Section 3.1, the analytical model, programmed in Python will be explained. This code was used to predict periodic tonal noise, and was used to design obstructions with low computational costs. Next, in Section 3.2, the numerical setup in PowerFLOW is elaborated upon, which was used to understand the fan primary noise and to size and position the obstruction. Finally, the experimental setup is outlined in Section 3.3, which was used to validate the analytical and numerical results.

3.1 Analytical model

The analytical model intends to estimate the periodic, tonal noise generated by the fan loading. It is written in Python and consists of three main steps [53]: the definition of the inflow, or gust (Sec. 3.1.1), the unsteady blade force response to this excitation (Sec. 3.1.2), and the noise propagation due to this blade loading (Sec. 3.1.3). The approach outlined by Gerard et al [32] was largely used, with a few adaptions. The method is based on Blake [9] his work to calculate rotor unsteady loading noise.

The assumptions of the model are explained in each of the corresponding subsections, however, general assumptions are:

- Only the blade loading term is calculated (dipole term), the monopole term is ignored as it is small for these kind of blades
- The tonal noise from periodic fluctuations is calculated, broadband noise is not included.

The coordinate system that is used is the same as was used in Gerard his paper and is shown in Fig. 3-1.

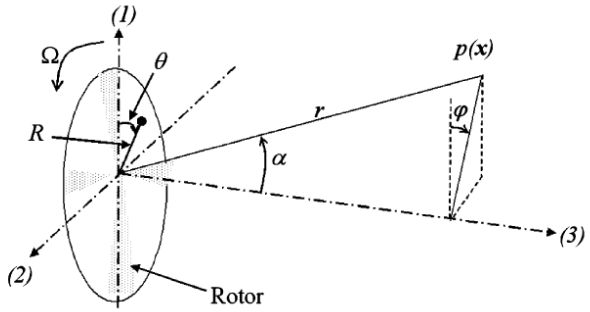

Figure 3-1 Coordinate system used [32]

3.1.1 Definition of the inflow

The first part of the model is to define the non-uniform inflow to the fan. This is defined separately for the primary and secondary (obstruction) noise. For the primary noise, the inflow of the fan has to be determined

from experimental or numerical methods. For the secondary noise (the obstruction) a Gaussian wake is assumed behind the obstruction. Still, some parameters (constants) defining this wake have to be determined experimentally or numerically. The inflow definition of the primary and secondary noise will be described separately below.

The assumptions in this part of the model are:

- The wake from an obstruction is Gaussian

Fan non-uniform inflow (primary noise)

As mentioned, the primary, non-uniform inflow field has to be extracted from simulations. In this case, the PowerFLOW LBM simulations are used which are also used for verification purposes. Axial slices (aligned with the rotor plane) are exported from the mean volume measurements, at numerous locations upstream of the rotor (1mm,2mm,3mm,5mm,10mm,15mm,20mm). This was done to see what location has the best correspondence with simulations, which is inconclusive in the literature. This will be explained in Section 4.2.

The measurement points that are exported align with the PowerFLOW grid. Since an integration will be done along the span of the blade in the model, these points are interpolated to a structured, cylindrical grid using a nearest-neighbor approach. Only the data between the rotor hub and tip is used, all the rest is ignored. An example of this process is shown in Fig. 3-2:

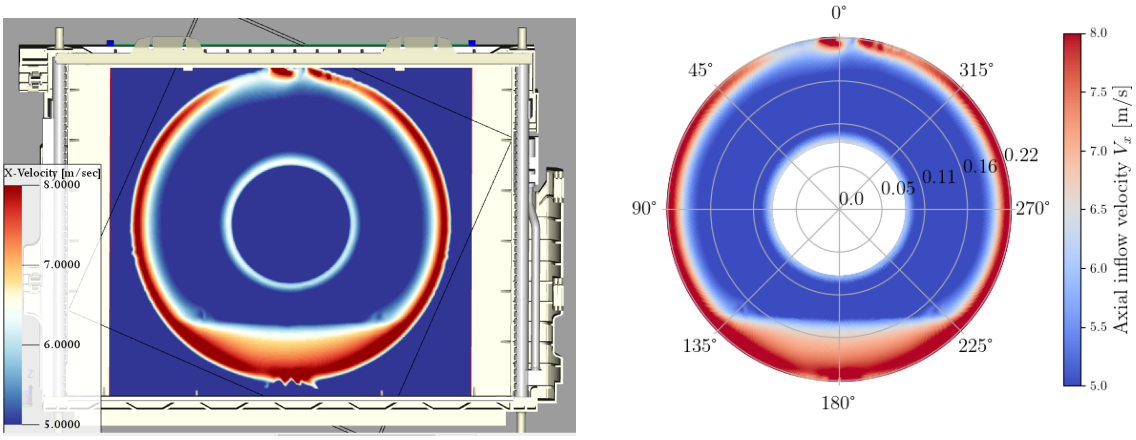

(A) PowerVIZ export

(B) Interpolated to cylindrical grid

Figure 3-2 Non-uniform inflow 3mm upstream of the fan

Obstruction wake definition (secondary noise)

The obstruction wake is assumed Gaussian, as was done in [32]. Gerard et al consider a cross-section of angular width $\Theta(R)$ as a function of spanwise location and define the wake deficit behind this section using Gaussian width parameters a_R, a and v_m. See Fig. 3-3 for clarification.

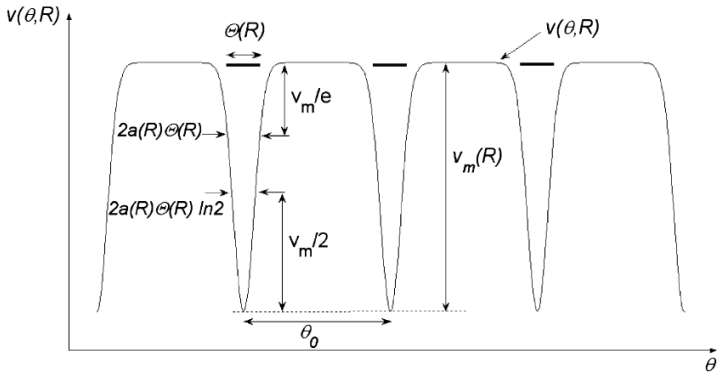

Figure 3-3 Wake velocity deficit from upstream angular segments $\Theta(R)$ [32]

$\Theta(R)$ is then defined for each obstruction shape separately. However, for this approach to work, the obstruction has to be periodic, with $\Theta(R)$ the same for each lobe at any circumferential location θ. Since in this thesis, multimodal obstructions are analyzed as well, a slightly different approach was used. The outer radius R_2 of the obstruction is defined as a function of angular coordinate θ, and some constants (which can be varied to obtain different obstruction designs).

$$R_2 = R_1 + \frac{B}{2} + \frac{A}{2} + \frac{A}{2}cos(L(\theta + \phi)) \tag{3-1}$$

Here R_1 is the base radius, defined as the middle of the base section with constant thickness B. A is the lobe amplitude, L is the number of lobes and ϕ is the angle of the obstruction compared to $\phi = 0$, which is defined upward. See Fig. 3-4 for clarification. The inner radius of the obstruction is $R_0 = R_1 - B/2$

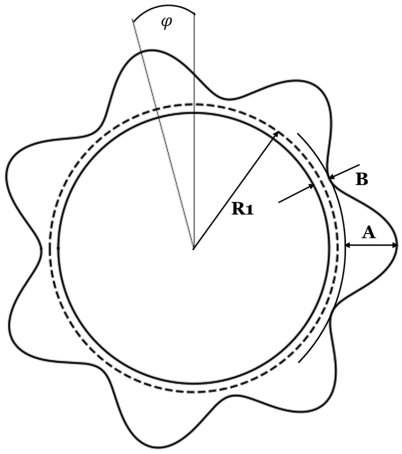

Figure 3-4 Clarification of variables used to define obstruction

Then, the velocity between R_0 and R_2 is set to v_m. Next, a Gaussian kernel filter is used to create the Gaussian wake. The Gaussian width parameters σ_R and σ_θ are used to define the wake in radial and circumferential direction separately. Since the approach is slightly different, it will be verified with the approach by Gerard in Chapter 4. An example of such a wake is shown in Fig. 3-5, with $v_m = 2$.

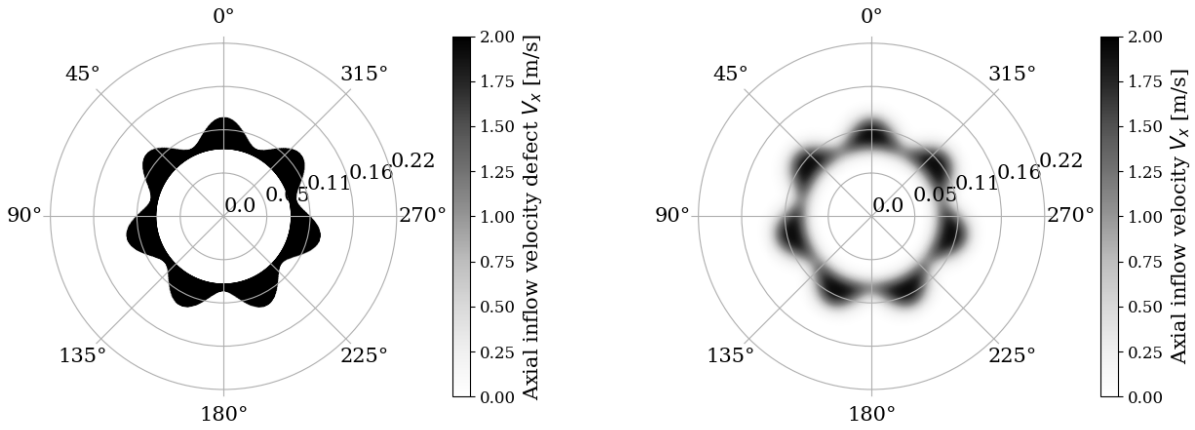

(A) Obstruction wake without filter

(B) Obstruction with Gaussian filter

Figure 3-5 Obstruction wake definition

These three parameters, v_m, σ_R, and σ_θ have to be altered to match the data from simulations (or Hot Wire measurements). Especially with the radiator and condenser upstream of the fan, and downstream of the obstruction, it is hard to make a prediction model for these parameters. The model will therefore remain semi-analytical, which was also the case for Gerard et al, where three parameters are needed to define the wake.

Fourier decomposition of transversal velocity

For both the primary non-uniform inflow and the obstruction wake definition, the transversal velocity (axial velocity) as a function of cylindrical coordinates is now obtained: $v(\theta, R)$. To calculate the resulting unsteady lift in the frequency domain, this inflow velocity is harmonically decomposed in circumferential direction (spatial decomposition), with Equation 3-2.

$$\tilde{V}(w, R) = \frac{1}{2\pi} \int_0^{2\pi} v(\theta, R) e^{-iw\theta} d\theta \tag{3-2}$$

In this equation, w is the circumferential order, $w = 1$ corresponding to a sine with one period along the circumference. $\tilde{V}(w, R)$ is the (complex) spectral velocity component at the given radius. Note that this step is different from the work of Gerard et al [32]. Since they were only interested in calculating the inflow from a flow obstruction, they derived the spectral velocity component analytically from the Gaussian wake formula's.

3.1.2 Blade (un)steady loading

To calculate the blade unsteady loading resulting from the non-uniform inflow, an unsteady Sears gust approach [75] is used. Steady loading is found using a Blade Element Momentum approach.

Assumptions

The assumptions used in this part of the model are:

- The gust is one-dimensional and periodic, with transversal velocity fluctuation in the reference frame of the blade.
- The blade is assumed to be a flat plate of infinitesimal thickness. No camber is taken into account, and the angle of attack is ignored.
- The chord and the sweep are assumed to vary linearly along the span of the blade

Unsteady loading (Sears gust problem)

For the gust problem to be one-dimensional (as opposed to a 2D oblique gust with radial and circumferential wavenumber), the blade is decomposed into infinitesimal radial strips along the span and is then integrated.

$$\begin{aligned}\tilde{L}(w) &= \int_{R_H}^{R_T} \frac{\mathrm{d}\tilde{L}(w,R)}{\mathrm{d}R}\,\mathrm{d}R \\ &= \pi\rho_0\Omega \int_{R_H}^{R_T} C(R)R\tilde{V}(w,R)\mathrm{e}^{\mathrm{i}w(-\theta_c(R))}S_c\left(\sigma_\theta, M_r\right)\mathrm{d}R\end{aligned} \tag{3-3}$$

In this equation $C(R)$, the chord as a function of radius, and $\theta_c(R)$, the sweep angle as a function of radius, are measured in CATIA, and are approximated by a linear estimation, given in Equation 3-4 and Equation 3-5, respectively. The Fourier velocity component $\tilde{V}(w,R)$ is a complex number and hence takes into account the phase/sweep of the gust. $S_c\left(\sigma_\theta, M_r\right)$ is the compressible Sears function.

$$C(R) = 0.0454 + 0.0496\frac{R}{R_T} \tag{3-4}$$

$$\theta_c(R) = (39.7\frac{R}{R_T} - 15.7)\frac{180}{\pi} \tag{3-5}$$

For $R = R_H$, this equation goes to zero, so the sweep at the root is defined as zero, which is arbitrary. Only the relative phase difference between the sweep and gust, for different spanwise locations, is important.

A compressible formulation is used since it is recommended when the time for an acoustic wave to travel the chord is no longer negligible when comparing it to the time it takes a blade to travel across a transversal gust [33]. Furthermore, it does not add complexity or computational time [32]. So, a compressible formulation developed by Amiet [5] is used, given in Equation 3-6. Zhong et al [89] also opted to use the compressible form in an automotive fan noise model.

$$S_c\left(\sigma_\theta, M_r\right) = \frac{S(\delta_\theta/\beta_r^2)}{\beta_r}\left[J_0(M_r^2\delta_\theta/\beta_r^2) + iJ_1(M_r^2\delta_\theta/\beta_r^2)\right]e^{-i\delta_\theta f(M_r)/\beta_r^2} \tag{3-6}$$

In this equation, J_0 and J_1 are the zeroth- and first-order ordinary Bessel functions. The rotational Mach number is a function of radius and given by $M_r = \Omega R/c_0$, and $\beta_r \equiv \sqrt{1-M_r^2}$. $\delta_\theta = wC/2R$ is the reduced frequency, and $f(M_r)$ is given by Equation 3-7. $S(\delta_\theta)$ is the compressible Sears function [49], and is given by Equation 3-8. Here, K_0 and K_1 and the zeroth-order and first-order modified Bessel functions.

$$f(M_r) \equiv (1-\beta_r)\ln M_r + \beta_r \ln(1+\beta_r) - \ln 2 \tag{3-7}$$

$$S(\delta_\theta) = \frac{1}{i\delta_\theta\left[K_0(i\delta_\theta) + K_1(i\delta_\theta)\right]} \tag{3-8}$$

Amiet [5], poses a criterion on the applicability of Equation 3-6, given by: $\delta_\theta M_r/\beta_r^2 < 1$, which comes down to $w < 2R(1-M_r^2)/CM_r$. For the current fan, the minimum is found at the tip, with $\Omega = 2180/60 * 2\pi$ rad/s, radius of 0.215 m, and chord of 9.5 cm, resulting in a maximum circumferential order of $w_{max} = 31$. This is not a problem, however, since for the frequencies where these order fluctuations are dominant sound radiators, the blade is no longer compact anyway. The summation over w, is limited to $-30 < w < 30$.

An overview of the 1D Sears problem is given in Fig. 3-6:

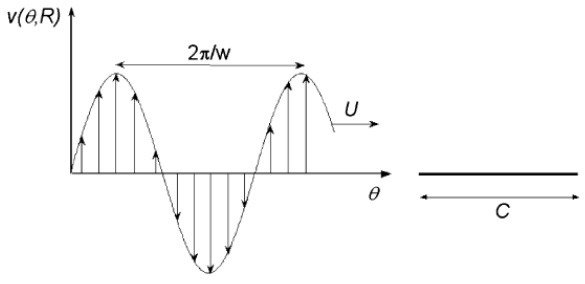

Figure 3-6 The blade section in a transversal Gust [32]

Steady loading
Gerard et al [32] did not include the steady loading of the blade, or $\tilde{L}(w=0)$. This was ignored, since the noise from steady loading is small compared to the unsteady loading for small, low Mach number fans, especially away from the rotor plane. Furthermore, they were only interested in calculating the noise from a flow obstruction (qualitatively).

Here, however, for completeness, the steady loading was included in the model. To retain to a completely analytical approach, a Blade Element Momentum algorithm can be used to calculate the average loading. Such a method was used here as well, adopted from Zhong et al [89], who used a BEM algorithm on an automotive fan with a lift and drag polar typical for automotive fan airfoil profiles. Results from this BEM approach are given in Appendix A.

However, since the pressure drop from the radiator and condenser is not accounted for in the approach, the axial loading is underestimated by about 0.4N, on each blade. For noise calculations, it is not important, however, as it was verified that the unsteady loading noise dominates the steady tones at all locations in the far-field. When information on the fan operating point is known (static pressure), the steady loading can also be estimated by multiplying the pressure jump with the rotor area, and dividing by the number of blades.

3.1.3 Far-field noise from blade loading

This subsection will explain how the far-field noise resulting from blade loading is obtained. The assumptions related to this part of the code will be listed first. Then the equations as presented by Gerard et al [32] for equally spaced fans are given, and the changes that were made to them to account for blade spacing variations are elaborated upon.

Assumptions
The assumptions used in this part of the model are:

- The blade is assumed acoustically compact in both the radius and chord. Practically, this means 1 rotating dipole per blade is used. This poses a constraint on the maximum frequencies that can be accurately predicted
- The observer is in the far-field: $r \gg R$
- Radial force fluctuations are smaller than axial and tangential force contributions and are therefore ignored
- Only the pressure modes $q_- = mB - w$ are taken into account q_+ modes are ignored, as they have a lower rotational velocity. See also Sec. 2.2.1.
- For an uneven spacing of rotor blades, the lift fluctuations on each of the blades remain the same. No aerodynamic effects due do varying blade spacing is taken into account

Equally spaced blades
To calculate the far-field noise, the approach in the classical work by Blake [9] was used as a base by Gerard et al [32]. The only difference is that Gerard et al take into account the phase of the gust and sweep of the blades in the complex circumferential decomposition of the unsteady lift (this is also done here). The sound pressure $p(\mathbf{x},t)$ from B equally spaced blades at location $\mathbf{x} = (r,\phi,\alpha)$ is found by integrating the product of the lift per unit span $\mathrm{d}\tilde{L}(w,R)/\mathrm{d}R$, for circumferential mode w, and the appropriate Green function for rotating dipolar sources in free field. When assuming the observer is in the far-field ($r \gg R$), the far-field pressure is given by:

$$p(\mathbf{x},t) = \sum_{m=-\infty}^{\infty} \sum_{w=-\infty}^{\infty} [P(\mathbf{x},\omega)]_{w,m} \mathrm{e}^{-\mathrm{i}mB\Omega t} \tag{3-9}$$

where $[P(\mathbf{x},\omega)]_{w,m}$ is,

$$[P(\mathbf{x},\omega)]_{w,m} = \underbrace{\frac{-\mathrm{i}k_0 B \mathrm{e}^{\mathrm{i}k_0 r}}{4\pi r}\mathrm{e}^{-\mathrm{i}(mB-w)(\pi/2-\varphi)}\delta(\omega - mB\Omega)}_{\text{Acoustic wave propagation}} \times \int_{R_H}^{R_T} \underbrace{J_{mB-w}\left(k_0 R \sin\alpha\right)}_{\text{Bessel function term}}$$
$$\times \underbrace{\frac{\mathrm{d}\tilde{L}(w,R)}{\mathrm{d}R}}_{\text{Unsteady lift per unit span}} \times \left[\underbrace{\cos\gamma(R)\cos\alpha}_{\substack{\text{Axial forces}\\ \text{contribution}}} + \underbrace{\frac{mB-w}{k_0 R}\sin\gamma(R)}_{\substack{\text{Tangential forces}\\ \text{contribution}}} \right] \mathrm{d}R \tag{3-10}$$

In this equation, $\omega = mB\Omega$, and the first summation represents the addition of the tones at different frequencies. The second summation is the addition of the circumferential harmonics w. The first term in Equation 3-10, is to describe the acoustic propagation, $k_0 = \omega/c_0$ is the corresponding wave number, of the pressure mode, that rotates with $mB\Omega/(mB-w)$. The Bessel function J_{mB-w} is a result of the Doppler effect between blade and observer, and results in a 'weighing', classifying the ability of the mode w to radiate sound at harmonic m of the BPF. The lift per unit span $\frac{\mathrm{d}\tilde{L}(w,R)}{\mathrm{d}R}$ is decomposed in axial and tangential forces, based on the pitch angle γ.

Note that the q_+ modes, as described in Sec. 2.2.1 are ignored in this method, as well as the radial forces. Furthermore, note that, when the summation over w is removed, and only $w = 0$ is considered, the equations reduce to an equivalent form of the work from Gutin [37] or Hanson [38], calculating steady loading noise. Hanson's helicoidal surface theory however also includes thickness noise, and a chordwise distribution of the loading. Furthermore, the Doppler effect due to the movement of the source (usually a propeller) to the observer is taken into account, shifting the directivity pattern, but this is irrelevant in fan applications.

If the length scale of the pressure fluctuations on the blade is smaller than the acoustic wavelength, the blade can be assumed compact. It can be reduced to a single rotating dipole at $R_m = 0.7R_T$ [49][9]. However, it is still important to take into account the relative phase of the blade sweep and the transversal gust in the integration of the lift along R, $\tilde{L}(w)$(Equation 3-3). Equation 3-10 can now be simplified to Equation 3-11:

$$\begin{aligned}[P(\mathbf{x},\omega)]_{w,m} \approx &\frac{-\mathrm{i}k_0 B \mathrm{e}^{\mathrm{i}k_0 r}}{4\pi r}\mathrm{e}^{-\mathrm{i}(mB-w)(\pi/2-\varphi)}\delta(\omega - mB\Omega) \times J_{mB-w}\left(k_0 R_m \sin\alpha\right) \\ &\times \tilde{L}(w) \times \left[\cos\gamma\cos\alpha + \frac{mB-w}{k_0 R_m}\sin\gamma\right]\end{aligned} \tag{3-11}$$

In this equation, γ is the pitch angle at $R = R_m$. Note that this equation is still exact when $a = 0$, hence on the fan axis, since here only pressure modes $q = 0$ contribute, which rotate in phase with infinite rotational velocity.

Unequally spaced blades

For uneven blade spacing, there no longer is a completely constructive interference at BPF and harmonics ($N = mB$), and destructive interference when $N \neq mB$. So now, instead of multiplying the noise response from a single blade loading with the number of blades, the phase angle has to be considered and a summation over all the blades is necessary. Furthermore, instead of only considering the BPF and harmonics ($N = mB$), tones will appear on all harmonics N of the rotational frequency.

Equation 3-11 therefore changes to Equation 3-12 for an unequally spaced fan:

$$\begin{aligned}[P(\mathbf{x},\omega)]_{w,N} = &\sum_{k=0}^{B-1} \frac{-\mathrm{i}k_0 \mathrm{e}^{\mathrm{i}k_0 r}}{4\pi r}\mathrm{e}^{-\mathrm{i}(N-w)(\pi/2-\varphi)}\mathrm{e}^{-\mathrm{i}N\theta_k}\delta(\omega - N\Omega) \times J_{N-w}\left(k_0 R_m \sin\alpha\right) \\ &\times \tilde{L}(w) \times \left[\cos\gamma\cos\alpha + \frac{N-w}{k_0 R_m}\sin\gamma\right]\end{aligned} \tag{3-12}$$

Where θ_k is the angle of the kth blade with respect to the first blade. Note that the lift fluctuation $\tilde{L}(w)$ is assumed independent of blade spacing. The validity of this assumption will be verified later.

Note that, for evenly spaced blades, $\sum_{k=0}^{B-1} \mathrm{e}^{-\mathrm{i}N\theta_k} = B$, when $N = mB$ and Equation 3-12 is equivalent to Equation 3-11. All harmonics N are now calculated instead of just BPF and harmonics, but all these will be zero since, $\sum_{k=0}^{B-1} \mathrm{e}^{-\mathrm{i}N\theta_k} = 0$, when $N \neq mB$.

The far-field sound pressure (for equal spaced fans Equation 3-9), now changes to Equation 3-13:

$$p(\mathbf{x}, t) = \sum_{N=-\infty}^{\infty} \sum_{w=-\infty}^{\infty} [P(\mathbf{x}, \omega)]_{w,N} \mathrm{e}^{-\mathrm{i}N\Omega t} \tag{3-13}$$

Effectively, the tones N with frequency $\omega = N\Omega$ are of interest in the frequency domain, which are calculated as sound pressure in decibels for each harmonic as:

$$SPL_N(\mathbf{x}) = 10log_{10}\left[\left(\frac{\sum_{w=-\infty}^{\infty}[P(\mathbf{x}, \omega)]_{w,N}}{p_{ref}}\right)^2\right] \tag{3-14}$$

Where p_{ref} is the reference pressure for hearing by humans, equal to $2e^{-5}$ Pa.

3.2 Numerical setup

In this section, the numerical method and setup are explained. PowerFLOW V6 from Dassault Systemes was used in this thesis, which uses a VLES/LBM (Very Large Eddy Simulation/Lattice Boltzmann Method) approach. A brief background of the solver is given in Sec. 3.2.1. The description of the case, in terms of boundary conditions, meshing etc. is given in Sec. 3.2.2. The mesh strategy is presented in Sec. 3.2.3,and an overview of the measurements that are stored is given in Sec. 3.2.4. Finally, the changes that are made to the setup when an obstruction is added are explained in Sec. 3.2.5.

3.2.1 Background solver

The modeling approach that is used in PowerFLOW is based on the (discretized) Lattice-Boltzmann equation:

$$f_i(x + c_i\delta t, t + \delta t) = f_i(x, t) + \frac{\delta t}{\tau_f}(f_i^{eq}(x, t) - f_i(x, t)) \tag{3-15}$$

In this equation, f_i is the distribution function in velocity direction i at node x and time t. The superscript eq denotes the equilibrium distribution function, and τ_f is the relaxation term related to the fluid viscocity. The method is based on a particle collision model instead of classical Navier-Stokes (NS) based models. With respect to NS approaches, the Lattice Boltzmann Method approach offers some advantages in this application.

- The solver is compressible. This means the acoustics can be resolved directly if the resolution is sufficient (in the near field) which is the case since the microphones are only 1m from the fan. Furthermore, acoustic feedback mechanisms can be captured.
- The solver is designed to run on parallel clusters. This means that large simulations can run a significantly quicker when multiple cores are available
- No structured grid has to be (manually) created

3.2.2 Case setup

The critical condition for the fan noise is when the car is charging, as discussed in Chapter 2. In this case, no inflow is generated from driving the car, and the fan has to operate at or close to the maximum duty cycle. This is therefore also the condition that is investigated in simulations. The details of the setup are given in Tab. 3-1.

Table 3-1 General case setup

Property	Value	Unit
Rotational speed	2180	RPM
Ambient pressure	101325	Pa
Ambient temperature	20	$°C$
Density	1.204	kg/m^3
Fan diameter	430	mm
Hub diameter	170	mm
Fan blade number	7	-
Blade average chord length	75	mm
Tip gap	5	mm
Distance fan centre to floor	1.2	m
Initiatilization time (rotations)	5	[-]
Measurement time (rotations)	10	[-]

The rotation is realized using a sliding-mesh approach. A Local Reference Frame (LRF) is created that encapsulates the rotating part of the fan. All solids within this LRF region rotate with respect to the other parts of the domain, at a specified rotational frequency. The LRF region is visualized in Fig. 3-7.

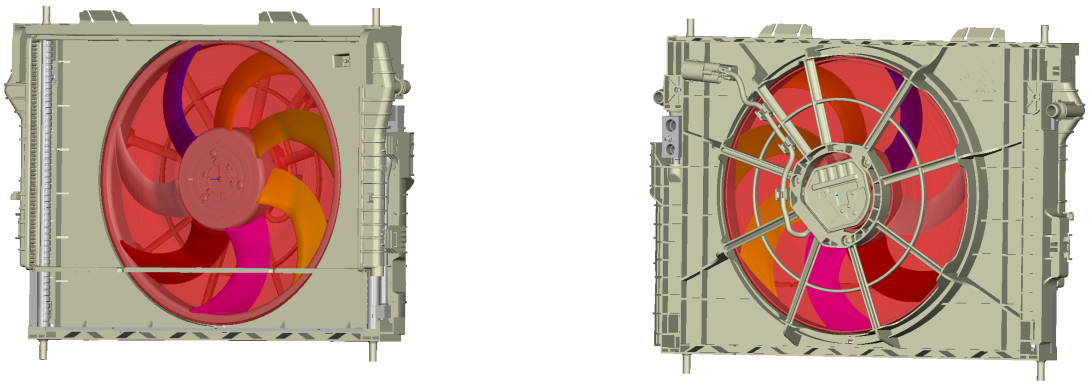

(a) LRF front view (b) LRF rear view

Figure 3-7 Rotor Local Reference Frame (in red)

Boundary conditions & initial conditions

The floor and all imported geometry (fan + shroud) impose a smooth wall boundary condition: no acoustic absorption is present and it has zero roughness. The ceiling, inlet, outlet, and the two walls have static pressure (ambient pressure), and free flow direction boundary conditions. They are 20m away from the fan in all directions. Hence, in practice, the fan is in an infinitely large room with a hard floor and no imposed inflow velocity/pressure difference. See also Fig. 3-8.

In a first, coarse simulation, the initial pressure is set to ambient pressure and the initial velocity to 0 m/s over the entire domain. From this simulation, the instantaneous flow quantities (density, pressure and velocity) at the end of the simulation are stored. In all subsequent simulations, the simulation is initialized with the pressure, density, and velocity of the previous simulation, a process called seeding. This reduces the required initialization time. The angle of the rotor has to match the previous simulation, hence an exact number of rotations is used.

Sponge zones

To dampen acoustic waves in the far-field, an anechoic outer layer is used. This is achieved by stepwise increasing the viscosity of the air in three 'sponge zones', as shown in Fig. 3-8. Sponge 1, has a viscosity over temperature $\nu/T = 0.05$, for zone two, $\nu/T = 0.1$. and the remainder of the simulation volume, or sponge zone 3 has a high viscosity of $\nu/T = 0.5$. Different steps are used for this since a sudden change in viscosity can cause some nonphysical pressure waves to occur.

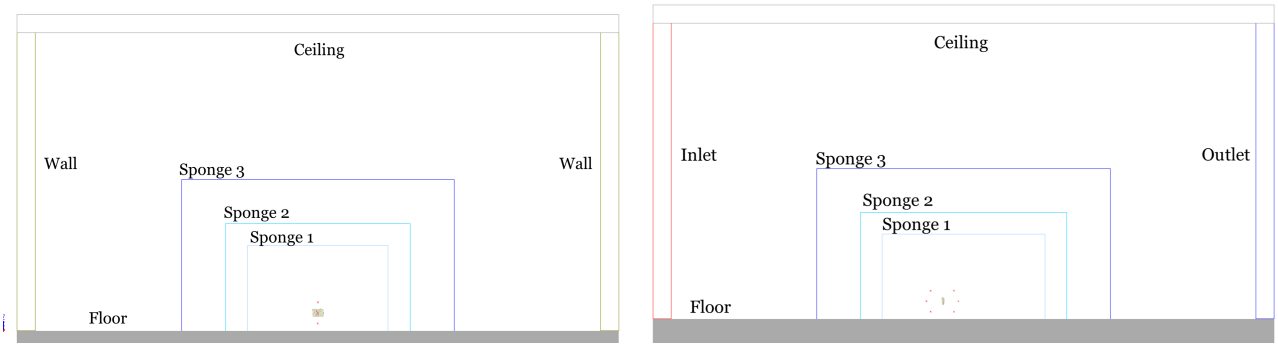

(A) Front view (B) Side view

Figure 3-8 Boundary conditions and sponge zones

Porous media

The condenser and radiator upstream of the fan contain a large number of small fins and holes, where the flow exchanges heat with these surfaces. Modeling these parts as an actual solid and fluid, would require an extremely fine mesh in those regions, resulting in an expensive and long simulation. Therefore, the heat exchangers are modeled as equivalent Porous Media (PM), which is illustrated in Fig. 3-9. The volume of the radiator/condenser that exchanges heat with the flow is modeled as a block of similar dimension and given porous media characteristics as described hereafter. Note that the radiator and condenser frame remain solid.

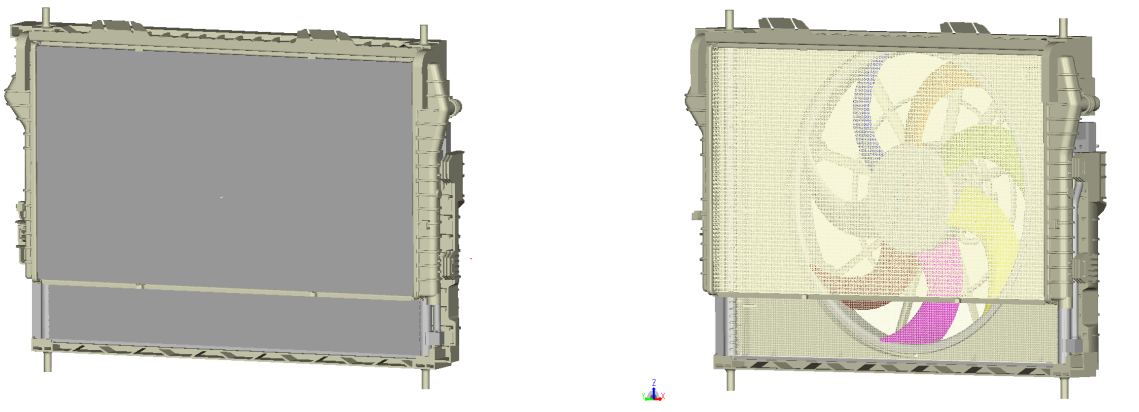

(A) Blocks (B) Porosity

Figure 3-9 Radiator/condenser modelling as porous media

The viscous resistance over this porous media, and resulting pressure flow rate and pressure drop are calculated using Darcy's law [77]. Note that, since the Reynolds number is high ($Re > 100$), the flow is turbulent and Darcy's law is no longer strictly valid. This is solved by allowing the resistance coefficient to be linear relation with velocity, resulting in a quadratic relation of pressure drop with flow velocity. The required input is the pressure drop over the heat exchanger as a function of mass flow. This information was experimentally obtained by the supplier and is given in Tab. 3-2. This data was obtained at 45 $^{\circ}C$ and an air density of 1.1097 kg/m^3.

Table 3-2 Porous media pressure drops

Flow rate [m/s]	Condenser pressure drop [Pa]	Flow rate [m/s]	Radiator pressure drop [Pa]
0	0	0	0
1.5	13.4	2.0	31.7
2.5	34.6	4.0	112.8
3.5	54.4	6.0	212.4
4.5	77.1	8.0	334.0

The resulting resistance curve is obtained using a quadratic curve fit by PowerFLOW, of the form:

$$\frac{1}{\rho}\frac{dp}{dx} = R_I V^2 + R_\nu V \tag{3-16}$$

The coefficients R_I (inertial resistance coefficient) and R_ν (viscous resistance coefficient) were obtained with the curve fit in PowerFLOW. For the condenser: $R_I = 120.15$ 1/m and $R_\nu = 435.19$ 1/s, and for the radiator: $R_I = 206.67$ 1/m and $R_\nu = 714.77$ 1/s.

In y and z directions, the viscous and inertial resistance are set to a value of $R_I = R_\nu = 1,000,000$, which is extremely high. Hence the flow is prevented from going in these directions.

3.2.3 Mesh strategy

In PowerFLOW, the fluid mesh is automatically created, based on the Variable Resolution (VR) regions, defined by the user. Cubic voxels are generated, where the voxel's edge length within each VR region is halved. In this setup, 10 VR regions are specified. The finest resolution region (VR10) is shown in Fig. 3-10a. It consists of an offset of 8 local voxels from the rotor, as well as a donut-shape around the tip of the propeller. VR9, as shown in Fig. 3-10b, consists of an offset of 6 local voxels from the radiator, condenser, shroud and fan, as well as a cone to cover the wake. VR8 is a box around the fan (orange box in Fig. 3-10b), VR7 is a sphere of 1.29m radius, and VR6 a sphere of 2m radius. VR5 up to VR0 (simulation volume) are increasingly large rectangular boxes as shown in Fig. 3-10c.

The finest voxel length has a resolution of 900 voxels per fan diameter, equivalent to ≈125 voxels per chord length (at the root), or 0.48mm. This was determined after a grid convergence study, detailed in Section 4.1.

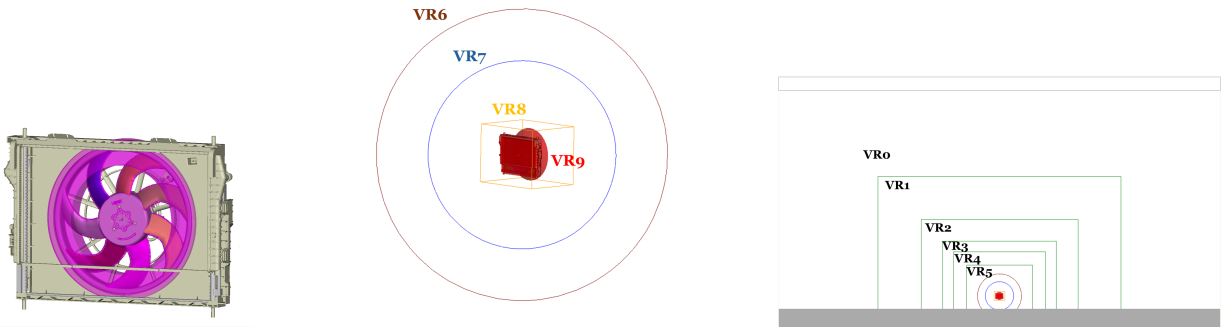

(a) VR10 (b) VR6 to VR9 (c) VR0 to VR5

Figure 3-10 VR regions

3.2.4 Measurements

In PowerCASE, the measurements that are stored during the simulation are specified. Three different categories are used, namely probe measurements, surface measurements, and volume measurements. A summary of the measurements taken and their respective purpose is given below. For a complete overview of the measurements, including their measurement time, interval, averaging etc is given in Appendix B.

- Probe measurements
  - Microphone 1 to 6 as shown in Fig. 3-11b
  - Circular array 10 mics, shown in Fig. 3-11b

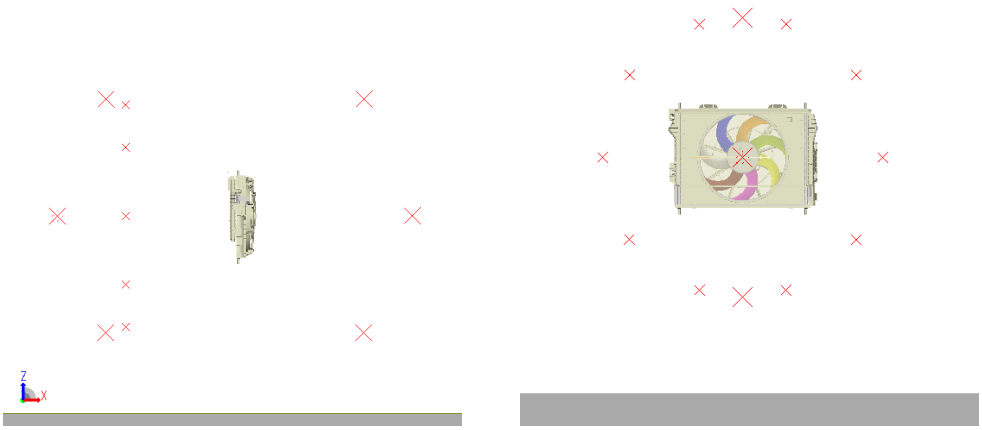

(A) 6 microphones (B) Circular microphones

Figure 3-11 Microphone location

- Surface measurements
  - Rotor+ shroud surface:
  - Modal plane measurement
- Composite measurement
  - Rotor forces: The force over time is measured at a frequency of 20kHz. Each of the blades, the hub, and the outer ring are measured separately.
- Volume measurements
  - Box around fan, shown in green/blue in Fig. 3-12a
  - X,Y and Z plane: the red planes in Fig. 3-12b

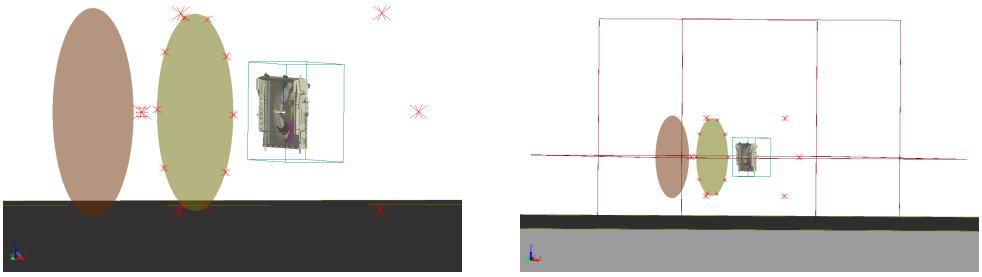

(A) Modal planes and volume measurement (B) x,y, and z plane

Figure 3-12 Simulation measurements

3.2.5 Numerical setup with obstruction

For the simulations with obstruction, a few adaptations are made to the setup. Another LRF is added for the obstruction, allowing for the obstruction to rotate, which is shown in orange in Fig. 3-13a. Furthermore, a

VR10 offset is added on the obstruction and a VR9 to cover the wake of the obstruction shown in Fig. 3-13b and Fig. 3-13c, respectively.

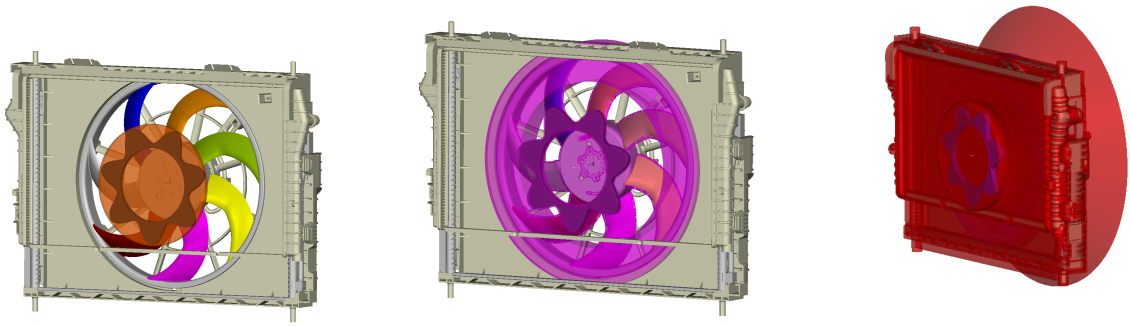

(A) LRF obstruction (B) VR10 obstruction (C) VR9 obstruction

Figure 3-13 Added LRF and VR regions with obstruction

To optimize the amplitude and phase of the obstruction, the method outlined by Moreau et al [57] was used, which makes use of a beat effect [29].

First, to determine the optimal lobe amplitude, the obstruction is rotated in the opposite direction of the fan rotation with a frequency of 200rpm. In doing so, the obstruction will create a secondary tone on the frequency BPF + LPF (Lobe Pass Frequency), which, for an obstruction with seven lobes and fan rotational frequency of 2180rpm and 7 blades results in: $(2180 * 7 + 200 * 7)/60 = 277.667Hz$. The lobe amplitude is then varied until the secondary tone is as loud as the primary tone on BPF.

Secondly, with the lobe amplitude determined from these simulations, the obstruction is rotated with a much lower frequency (30rpm). Now the primary and secondary tone match (when using a slightly larger bandwidth) and the variation of the BPF tone amplitude over time can be extrapolated. This can be done by evaluating the temporal fluctuations of the Hilbert transform. The obstruction angle should be corrected for its rotation using Equation 3-17 [57]:

$$\phi_c = 2\pi\Omega_o D/V_\infty \tag{3-17}$$

Finally, the obstruction surface is added to the high-frequency wall-pressure measurements, so the noise that is created on the obstruction surface itself can also be evaluated with the acoustic analogy.

3.3 Experimental validation setup

This section will describe the experimental setup that was used for validation purposes. First, in Sec. 3.3.1, the test location is described. Focus is put on potential differences with the simulation setup. Then, in Sec. 3.3.2, the electronics used to power and control the fan are explained, as well as the data acquisition system. Finally, in Sec. 3.3.3, the measurement campaign is described.

3.3.1 Test location

The tests are conducted in the TU Delft Anechoic Chamber. The room is anechoically treated and has a dimension of 8x8x8 m, large enough to measure the low-frequency noise with wavelengths over a meter. The room has a 'floating' floor, meaning there are also no reflections from the floor. This does introduce a difference with the simulations, both aerodynamically and acoustically. In terms of aerodynamics, the re-circulation from the fan is not restricted in the same way in experiment and simulation, which might lead to a slightly different inflow, especially in the bottom half of the fan. Nevertheless, the fan was placed at the same height with respect to the 'grid' floor in the experiment, to allow for recirculating flow. See Fig. 3-14 for an overview of the setup.

Acoustically, no pressure waves are reflected from the floor in the experiment, as opposed to the simulations. This discrepancy can be circumvented by using the FWH analogy to compute the noise at microphone locations. It was already verified that this aligns well with numerical probe data. Aside from the missing reflective surface,

the measurements were done following the ISO3745 standard [1], eg in terms of background noise, room volume, measurement frequencies etc.

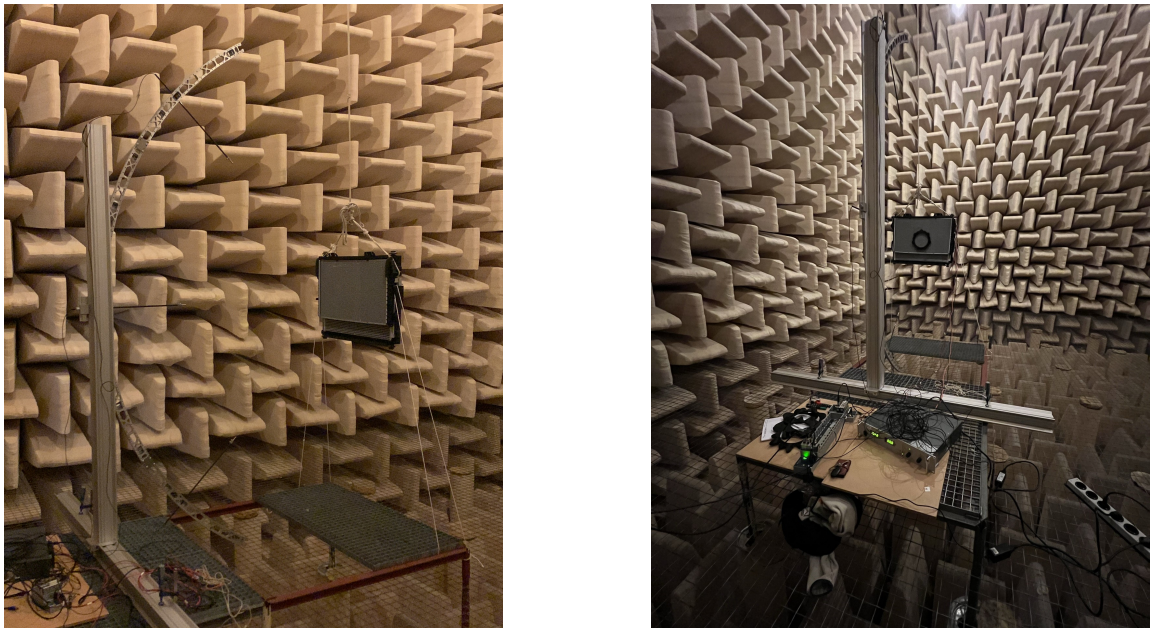

(A) Side view (B) Front view

Figure 3-14 Experimental test setup

3.3.2 Electronics & data acquisition

The fan is powered with a Delta Elektronika SM15-100[1] power supply. The fan supply voltage is 13.5V with a maximum expected current of around 35A. To control the RPM of the fan a PWM signal of 5V with a 200Hz frequency was generated in LabVIEW and sent to the fan using a NI CompactDAQ chassis and a NI-9401 digital I/O module. By varying the pulse width (duty cycle), the RPM of the fan could be changed.

Texas Instruments data acquisition was used with GRAS microphones. Three microphones were placed upstream using an arc, at a 1m radius, one on the fan axis, and at an angle of 45° upward and downward. The arc with microphones is also shown in Fig. 3-14a. To connect both the PWM and data acquisition chassis with a laptop, NI max software was used. The microphones were calibrated using the reported variance in mV/Pa in the accompanying data sheets for each microphone. The recorder voltage signal is converted to a pressure-time signal and stored, together with information regarding the measurement (measurement name, configuration, rpm, comments) in an HDF5 file using MATLAB.

3.3.3 Measurement campaign

A table of the complete test matrix is given in Appendix D. All measurements were conducted for 60 seconds, with a sampling rate of 51.2 kHz, resulting in a maximum frequency following the Nyquist criterion of 25.6 kHz, which is above the human hearing threshold.

Tests were conducted on three consecutive days. Background noise measurements were taken on the first and last day. Furthermore, tests without obstruction (baseline tests) were done on both these days, at four different duty cycles: 35%, 55%, 75%, and 95%. This configuration is shown in Fig. 3-15a.

[1] https://www.delta-elektronika.nl/products/sm1500-series

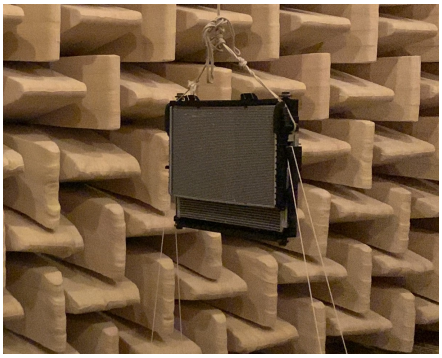

(A) With radiator

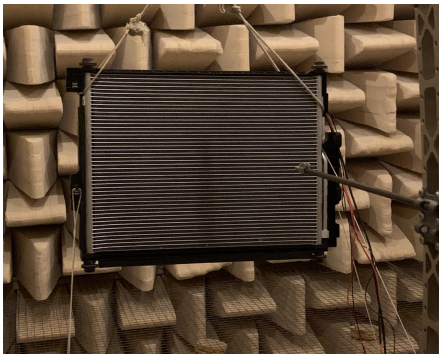

(B) Radiator removed

Figure 3-15 Fan module with and without radiator

A series of tests were done at these same duty cycles where the radiator was removed from the setup (condenser still in place), shown in Fig. 3-15b. This was done to assess the effect of the radiator on both tonal and broadband noise.

For tests with obstruction, an angle sweep was done for each obstruction. The obstruction could be rotated at set intervals of 3°. This was achieved by installing a ring on the radiator with a few pins (Fig. 3-16a), on which the obstruction with 120 evenly spaced holes (Fig. 3-16b) can slide onto. This is shown in Fig. 3-16c.

(A) Attachment ring on radiator

(B) Obstruction with 120 holes

(C) Obstruction on ring

Figure 3-16 Installation of the obstruction

Since the obstructions are N-periodic with $N = B = 7$, only obstruction angles ranging from 0 to $360/7 \approx 51.4°$ have to be measured. This results in a total of $51.4/3 = 18$ (rounded up) measurements per obstruction.

A few different obstructions were tested. The first was the one equivalent to the one used in simulations, with $N = 7$ and a lobe amplitude of $A = 40[mm]$. An angle sweep was conducted at 95% duty cycle. It was quickly seen during testing that the secondary tone from this obstruction was significantly larger than the primary tone, which resulted in a noise increase rather than a decrease (this will be explained further in Section 4.3). A smaller obstruction with $A = 30[mm]$ was then printed and another angle sweep was conducted at 95% duty cycle. The results were better but the obstruction was still too large, so the process was repeated once more with $A = 20[mm]$, and this yielded satisfactory results.

Then, repeat tests were conducted at the obstruction angle with maximum reduction. Furthermore, for this angle and the obstruction in place, measurements were done at a lower duty cycle to investigate the effect of the obstruction when a lower RPM is used. Furthermore, an angle sweep at 75% duty cycle was performed to compare the interference pattern at a different RPM.

Finally, on day three, some testing time was left. This time was used to see if it is possible to control two tones using a superposition of sine waves. Since the interference angle for both BPF1 and 2 could be retrieved from previous tests, these two tones were chosen as the tones to be controlled (the relative angle shift for maximum reduction between the two tones is needed for printing). This resulted in obstruction shapes shown in Fig. 3-17. For a full overview of the tests that were conducted see Appendix D.

Figure 3-17 Double cosine, 7 and 14 lobes superimposed

4

Grid convergence, verification and validation

In this chapter, the grid convergence and sensitivity and verification and validation for both the analytical and numerical work is described. First, in Section 4.1, the numerical grid refinement study is detailed, focussing on the convergence of integral parameters, and verifying to what extent the observed aerodynamic and acoustic phenomena are mesh-independent. Next, in Section 4.2, the analytical model is verified using simulation data, which is split up into the model's separate parts. Finally, in Section 4.3, both the analytical tool and numerical simulations are compared to experimentally obtained results.

4.1 Grid refinement study

In this section, the grid refinement study is described, which was done to investigate for which mesh refinement the results converge and are mesh-independent. A total of four mesh refinements were simulated, referred to as coarse, medium, fine, and very fine. Each mesh size was a refinement of 1.5x the previous mesh. A summary of these four simulations is given in Tab. 4-1.

Table 4-1 Mesh resolution, number of elements and computational time

Mesh	Resolution [voxels/ diameter]	Resolution [voxels/ chordlength]	Blade y+	Voxels (10^6)	FEV (10^6)	FES (10^6)	Time-step (10^{-7})[s]	CPUH [hours]
Coarse	400	75	22-120	47.7	15.6	3.2	18.08	1361
Medium	600	110	15-85	148	47.9	17.3	12.06	5360
Fine	900	160	10-55	476	152.9	37.9	8.04	16460
Very fine	1350	240	6-40	1542	484.8	93.3	5.36	81328

In Sec. 4.1.1, the convergence of selected integral parameters is analyzed and discussed. Then, the convergence of the aerodynamics and aeroacoustics is investigated separately in Sec. 4.1.2 and Sec. 4.1.3, respectively.

4.1.1 Integral parameter convergence

A mesh study was carried out to verify the convergence of the numerical simulations. Four resolutions were investigated as described in Tab. 4-1. Each simulation was 1.5x refined compared to the coarser simulation. The total mean thrust of one revolution is plotted versus the grid factor $N^{-2/3}$ in Fig. 4-1, where N is the total number of voxels. The total thrust is presented in absolute value since the simulated fan is to scale.

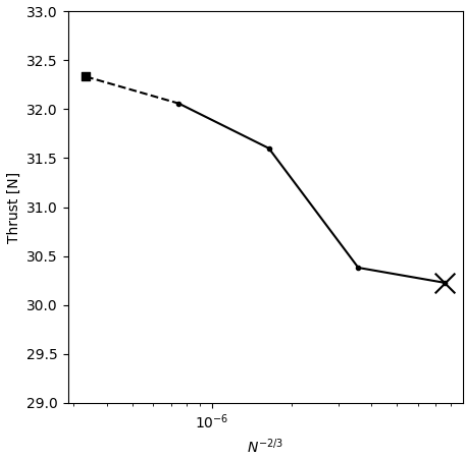

Figure 4-1 Richardson extrapolation total thrust

The dashed line in the figure shows the Richardson extrapolation using the medium, fine, and very fine mesh, disregarding the coarse mesh. The order of convergence $p = 2.42$ was found, lower than the theoretical value of $p = 3$. The refinement ratio is $r = 1.5$. The extrapolation shows the axial force is converging to $32.3N$. The Grid Convergence Index (GCI), defined by Roache [73], for the fine and very fine mesh are $GCI_{2,3} = 2.894\%$ and $GCI_{1,2} = 1.072\%$ respectively. Their ratio, as calculated in Equation 4-1, is close to one, indicating both the grids are within the asymptotic range of convergence [73].

$$\frac{GCI_{2,3}}{r^p GCI_{1,2}} = 1.02 \approx 1 \tag{4-1}$$

4.1.2 Convergence of the aerodynamics

This subsection will describe the convergence of the aerodynamics with respect to mesh size. The section will focus on the differences that were observed when refining the mesh. Additional comparisons that were made but did not show notable changes are presented in Appendix C. Averaged parameters on an x-aligned plane, that is moved in axial direction were compared for the different mesh sizes. This could show the axial velocity development and the static and total pressure drop/rise across the porous media and fan respectively. It was seen that both the axial velocity and pressure drop were increasing slightly, in line with the observations in Sec. 4.1.1.

Furthermore, averaged axial and tangential velocities across the fan radius (line plot), at different axial locations were compared between mesh sizes. No significant changes worth mentioning are noticed, but the plots can be found in Appendix C.

For both these analyses, only the coarse mesh showed significant differences.

Blade pressure coefficient

The mean pressure coefficient along the radius of one of the blades was compared between mesh refinements. This is shown at three locations along the radius in Fig. 4-2.

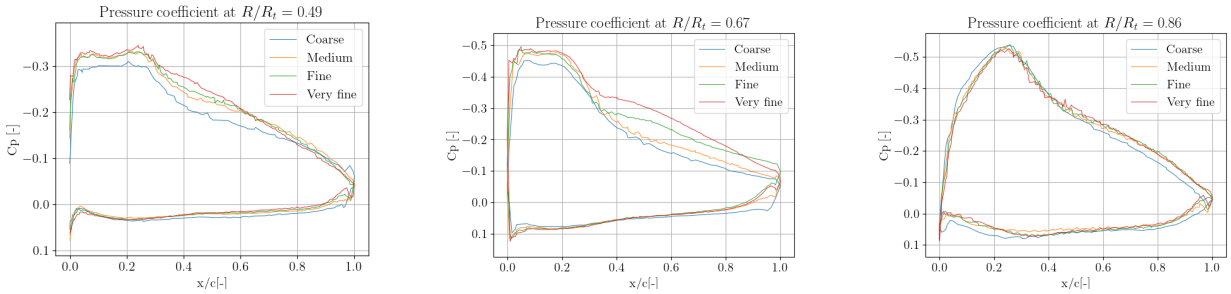

(A) Cp at blade root (B) Cp at blade midpsan (C) Cp at blade tip

FIGURE 4-2 Cp at three blade locations

As can be seen in the figure, differences are seen in the mid-section of the blade. When refining the mesh, the suction side pressure decreases, especially in the very fine mesh. This could point to a separation of the blade that is not predicted in all mesh refinements, which might mean the results are not mesh-independent. This was therefore investigated in more detail.

Separation blade midspan

As was already shown in the blade cross-sectional pressure coefficient, a discrepancy between different mesh refinements was found around the mid-span of the blades. When analyzing the transient flow at these locations, it was seen that the blade separated in this area (see also Appendix C for skin friction comparisons). It was observed that this separation occurred on only a part of the blade rotation, which is shown in Fig. 4-3.

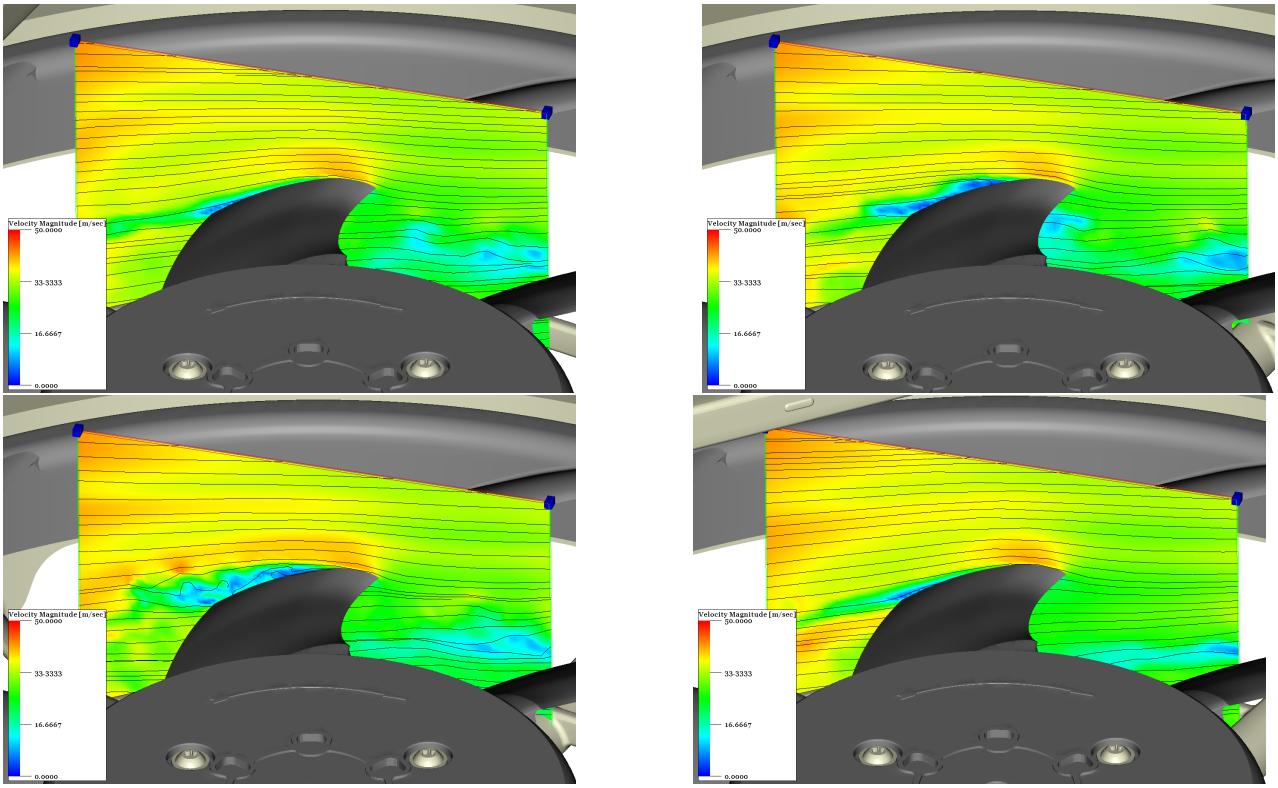

FIGURE 4-3 Instantaneous velocity magnitude (+streamlines) along blade rotation (in rotating reference frame)

The reason for this is most likely the presence of the radiator. The radiator does not cover the entire rotor disk, resulting in a non-uniform axial flow velocity, as was shown in for example Fig. 3-2.

This results in a significant change in the local angle of attack, following Equation A-2 and Equation 4-3.

$$\Phi = \arctan \frac{V_x}{2\pi\Omega R} \tag{4-2}$$

$$\alpha = \gamma - \Phi \tag{4-3}$$

In these equations, ϕ is the inflow angle, V_x is the axial inflow exported from PowerFLOW. Ω is the fan rotational frequency, R is the spanwise coordinate, α is the angle of attack and γ the twist angle. The rotation of the flow is ignored in this analysis. This may yield a small error in the absolute angle of attack, but the relative difference in the angle of attack on different circumferential locations is unchanged. This resulted in a local angle of attack map as shown in Fig. 4-4. It was observed that the location of separation corresponds well, where separation occurs at the top of the rotation, and only reattaches after passing the lower part, where the angle of attack is low.

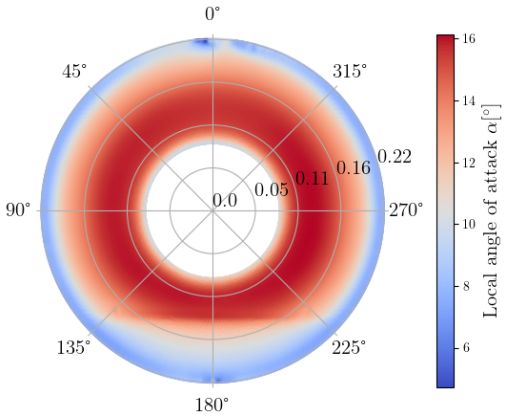

Figure 4-4 Estimated local angle of attack

As shown in the figure, the local angle of attack on the midspan behind the radiator is around 15 °, whereas, in the bottom part with the radiator absent, the angle is around 10 °.

In the context of this section, understanding the differences in separation prediction between mesh sizes is important. Following previous observations, it is more relevant to compare the local pressure coefficient distribution at different circumferential positions for different meshes. This way, it can be understood where the discrepancy in separation is evident. To do so, a phase-locked average of the transient data was taken: this averages the instantaneous measurement when the blade is in the same azimuthal position. E.g. when 10 rotations are measured, the 10 frames where the fan is in (or very close to) the same position are averaged.

It was observed that the differences between the fine and very fine mesh were mainly present in the top part of the rotation (blades 5,6 and 7 in Fig. 4-5a), which is shown in Fig. 4-5b and Fig. 4-5c. For the other part of the fan rotation, the agreement between fine and very fine was good, see also Appendix C.

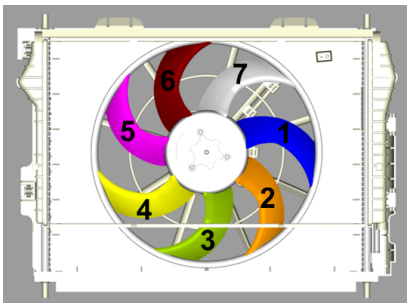

(a) Rotor numbering

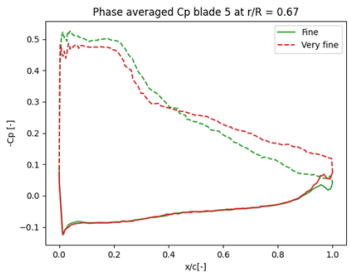

(b) Phased-locked average blade 5

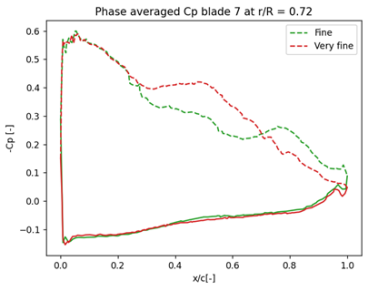

(c) Phase locked average blade 7

Figure 4-5 Phase locked average pressure coefficient

The reason more separation is predicted in the very fine simulation could be the value of $y+$ at these locations. PowerFLOW uses wall modeling in the viscous sublayer and logarithmic region. Casalino et al [11] needed a $y+$ below 10 on the entire blade to accurately resolve a transitional boundary layer, which is computationally infeasible in this study.

To assess the importance of this discrepancy on the total loading of the fan, the sectional lift at different location was compared between mesh resolutions to assess convergence, which is shown in Fig. 4-6. Similar to the plots in Sec. 4.1.1, the finest mesh is on the left.

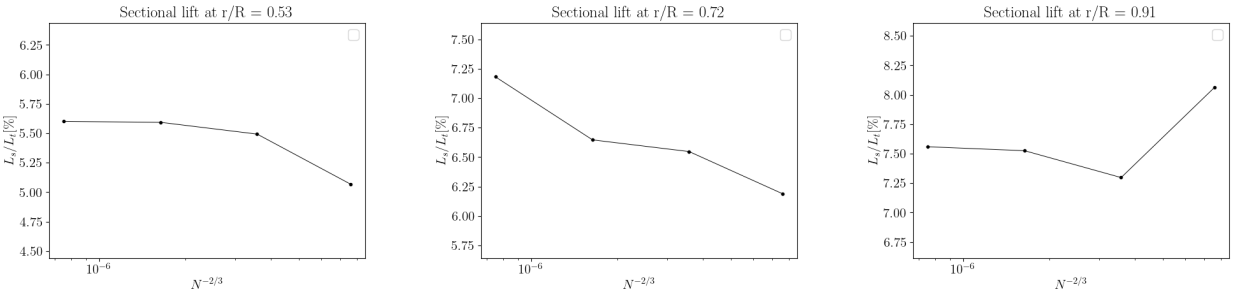

(A) Sectional lift blade root (B) Sectional lift blade midpsan (C) Sectional lift blade tip

Figure 4-6 Sectional lift (percentage total lift) for different mesh sizes

As can be seen in the figure, convergence is achieved at the root and tip of the blade, but no convergence is found around the midspan (to see all sections please see Appendix C). Nevertheless, the percentile change in lift of the total lift is only 0.5%.

4.1.3 Convergence of the acoustics

OSPL directivity

The Overall Sound Pressure Level, calculated at 1m from the fan center using the FWH analogy is shown in

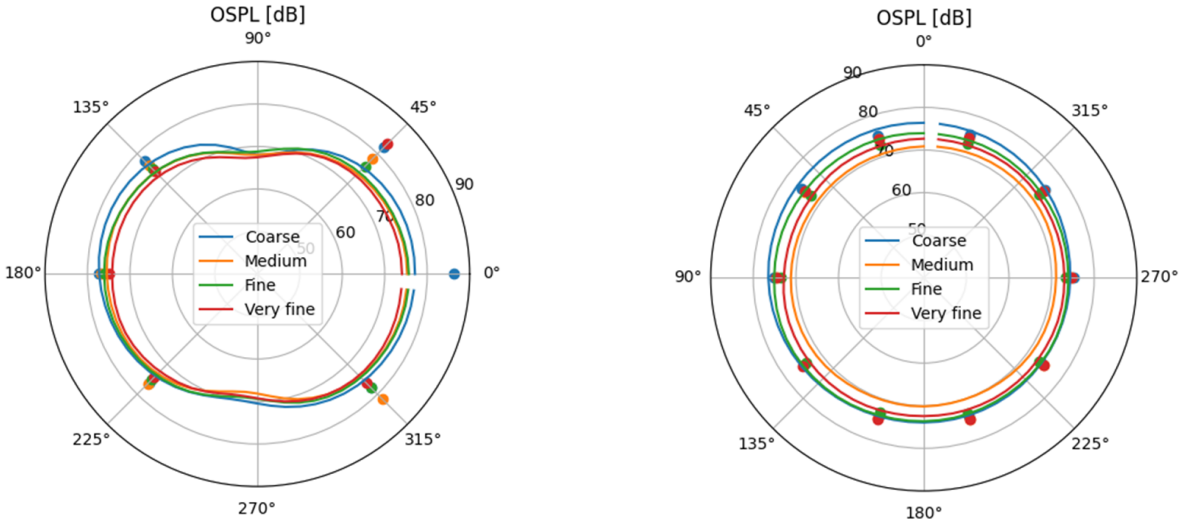

(A) OSPL perpendicular to rotor (B) OSPL parallel to rotor, 1m upstream

Figure 4-7 Cp at three blade stations

As can be seen in the figure, the OSPL is only off for the coarse case. Fine and very fine are close. Furthermore, the agreement with upstream microphones is good, the OSPL is overestimated in the wake of the fan, due to the hydrodynamic fluctuations.

Low-frequency tonal noise

The main interest for the thesis is in the magnitude of the low-frequency tones (150-3000Hz), especially the BPF and first harmonics. The unsteadiness of these tones in time poses a difficulty in comparing their magnitude in different simulations. Since simulating is computationally expensive, obtaining narrow-band tonal peaks with statistical convergence is difficult.

The narrowband spectrum is shown in Fig. 4-27, with the convergence of the BPF tone shown in Fig. 4-8b.

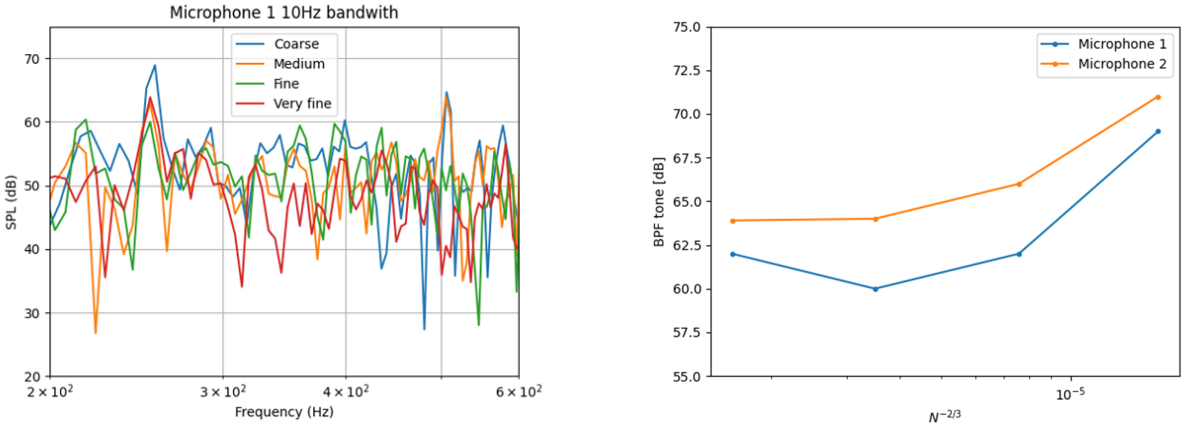

(A) Narrowband spectrum low frequency

(B) Convergence of tone at BPF

Figure 4-8 Convergence of low-frequency tonal noise

Broadband noise

The broadband spectrum measured by microphone 1 is shown in Fig. 4-29, presented in third-octave bands.

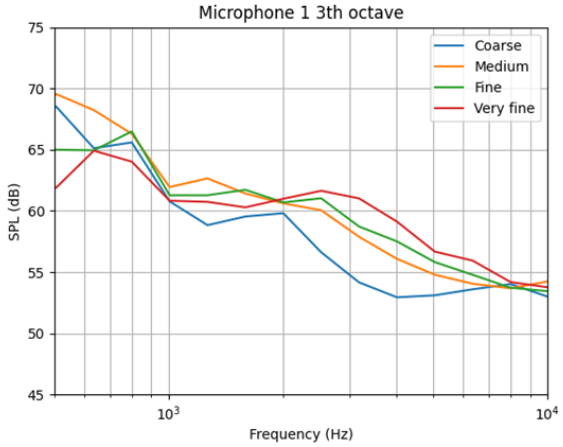

Figure 4-9 Broadband noise for different mesh sizes

As can be seen in the figure, the high-frequency noise is increasing with mesh resolution. This makes sense, as smaller structures are now also resolved. This is not important for this analysis, since the broadband spectrum is not affected by flow obstructions.

4.2 Verification of analytical model

With the convergence of the simulation verified, numerical results could be used to verify separate parts of the analytical model. In Sec. 4.2.1, the non-uniform inflow definition is verified. Next in Sec. 4.2.2, the loading

response (blade force) resulting from the inflow disturbance is correlated to numerical data. Finally, in Sec. 4.2.3, the noise propagation due to the blade's unsteady loading is verified.

4.2.1 Verification of inflow

To verify the definition of the inflow, two comparisons were made. First of all, the method used in this thesis was compared to the method used by Gerard et al [32]. Next, the wake definition will be compared to the wake as found in the simulation. This data will also be used to tune the parameters v_m, σ_R and σ_θ

Comparison with Gerard

As was explained in Sec. 3.1.1, Gerard et al [32] use a Gaussian wake where obstruction periodicity is required. To verify the approach in this thesis, it was compared to their approach. Their approach involves using the Poisson summation formula to come up with an equation for the transversal gust velocity. Please see their paper for a complete outline of the method.

A comparison between their method and the one used here is shown in Fig. 4-10. As can be seen in the figure, with proper tuning of the wake parameters in each of the models (which are free variables), a good agreement of the wake can be generated.

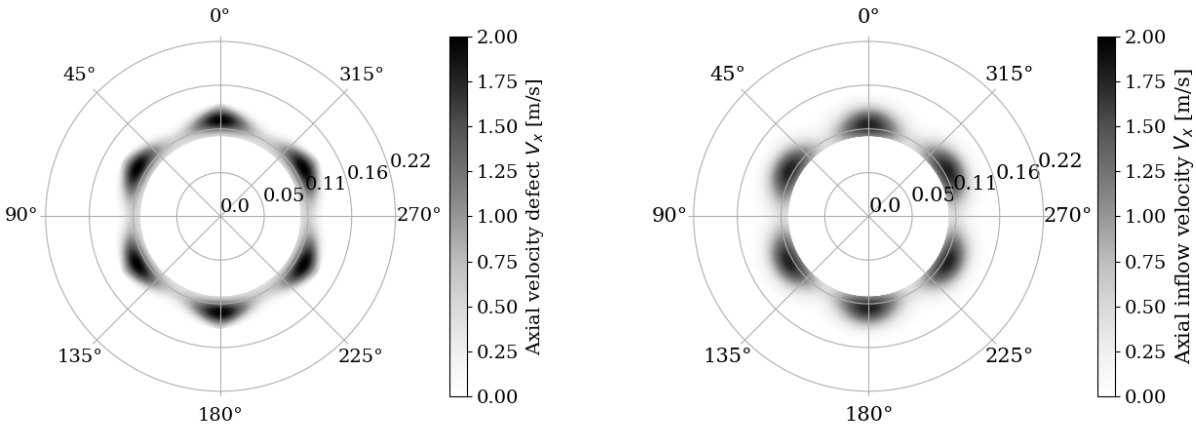

(A) Wake using Gerard [32] method

(B) Wake using current method

FIGURE 4-10 Comparison wake definition methods

Correlation to simulation data

Next, the obstruction wake was extracted from simulations. This was done by subtracting the mean flow from a simulation including static obstruction, with a simulation without obstruction. This results in just the difference between the two, which is shown in Fig. 4-11a. This wake definition was then used to tune the wake parameters in the model. The following yielded the result as shown in Fig. 4-11b: $v_m = 0.68$ m/s, $\sigma_R = 20$ and $\sigma_\theta = 20$.

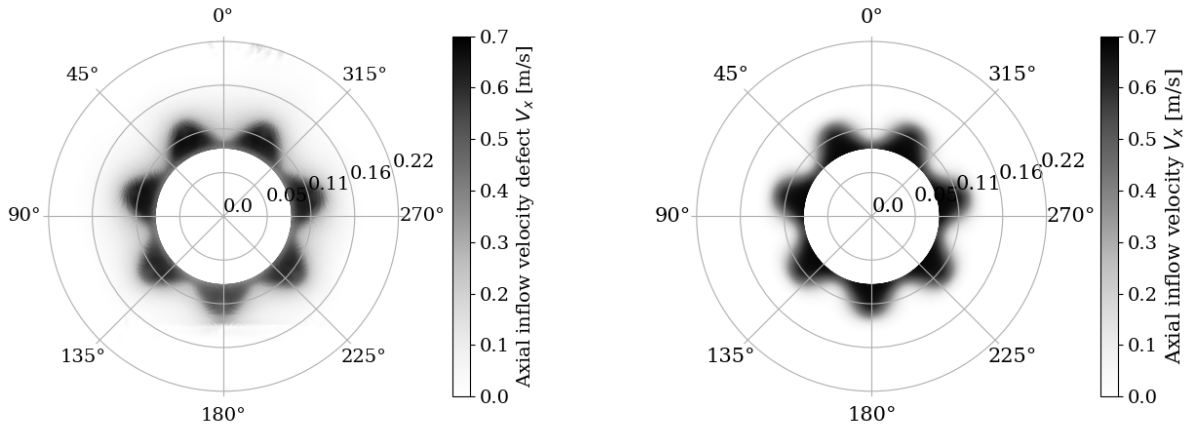

(A) Obstruction wake from simulation

(B) Model wake definition

Figure 4-11 Verification of obstruction wake definition

4.2.2 Verification of blade loading response

To verify the calculation of the blade loading resulting from the stationary, non-uniform inflow, simulation data was used. A slice of the mean flow in the axial direction upstream of the fan was exported from the simulation. This data was then interpolated to a grid in cylindrical coordinates, to be used as input to the analytical tool, as was described in Sec. 3.1.1. The resulting, fluctuation force modes from this inflow are then calculated using the model as described in Sec. 3.1.2.

The data that was used to verify this part of the model is the actual measured force on the rotor blades (composite measurement in PowerFLOW). The force measurement was divided over all the blades, the hub, and the ring, hence data for each blade is present.

First, the blade force measured over 7 rotations was averaged in a phase-locked manner. This yields the average blade force over one fan rotation, which is shown in Fig. 4-12a. The grey region indicates one standard deviation from the mean.

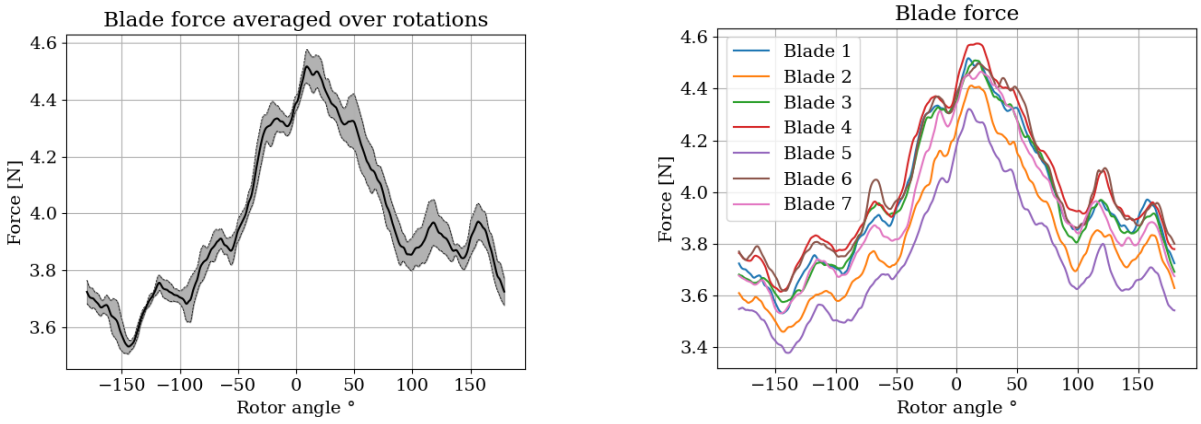

(A) Force fluctuation blade 1, 1 standard deviation indicated

(B) Force fluctuation different blades

Figure 4-12 Phase-locked force fluctuation

It was observed that the force over each of the blades was not completely the same, as shown in Fig. 4-12b, which is an assumption of the model. Nevertheless, this mainly impacted the low-order circumferential modes (especially the mean force, or mode 0).

Next, the mean was subtracted from this fluctuating force, since the fluctuations are calculated using the model. This was averaged over all the blades. The total standard deviation was calculated as:

$$\sigma_{tot} = \sqrt{\sigma_{B1}^2 + \sigma_{B2}^2 + ... + \sigma_{B7}^2} \tag{4-4}$$

Which resulted in the average blade force fluctuation from simulation given in Fig. 4-13. The grey area indicates the summed standard deviation.

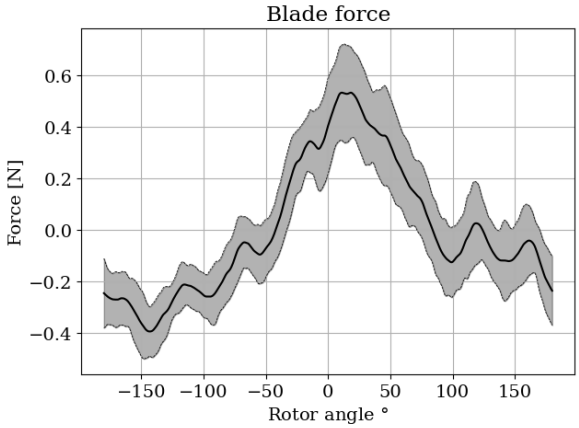

Figure 4-13 Force averaged over all blades, σ_{tot} in grey

Since a qualitative comparison is easier in the time/space-domain, the Force Fourier components, calculated in the model, were converted back to the force over azimuth using Equation 4-5:

$$F(\theta) = \sum_{w=-\infty}^{w=\infty} \tilde{L}(w) e^{iw\theta} \tag{4-5}$$

First, a grid sensitivity was done for the Python tool. As mentioned, the simulation measurements are interpolated to a cylindrical grid. Especially the number of points in circumferential direction can influence the results, shown in Fig. 4-14:

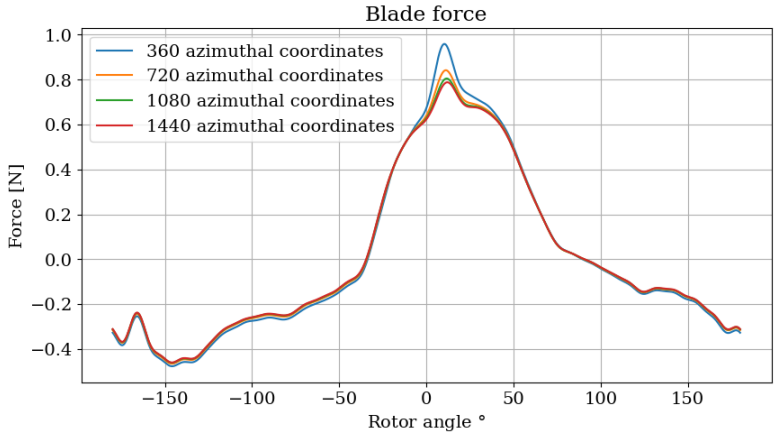

Figure 4-14 Convergence with azimuthal coordinates

As can be seen in the figure, from around 1000 azimuthal points the solutions converge. This makes sense, as the number of mesh coordinates in the simulation is around 1100 (grid size of 0.48m). In radial direction, 400 points were used, which also matched the simulation, and convergence was verified.

Next, the sensitivity to the location of the plane at which the inflow velocity is extracted was investigated. This is shown in Fig. 4-15:

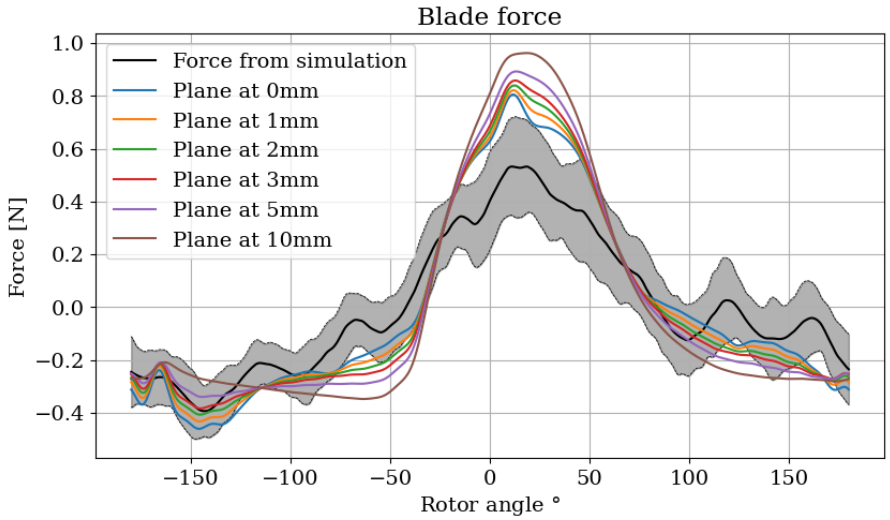

Figure 4-15 Force fluctuation different plane locations

As can be seen in the figure, the closer to the rotor, the better the force fluctuation matches simulation. This is in line with Sturm [79], but opposes what Renaud [72] found, who took a slice at 5cm upstream of the impeller. However, Renaud saw a potential effect of the rotor on the inflow distortion, which can be avoided by averaging the results for an exact number of rotations.

Furthermore, it was observed that the chord length has a significant contribution impact on the force fluctuation found by Equation 3-3, which makes sense at this relation is linear. As was explained in Sec. 3.1.2, the chord was estimated from CATIA at the root and tip and a linear relation between the two was used. In reality, when looking at for example Fig. 4-5a, the chord remains constant up to about mid span, after which the chord starts increasing towards the tip. Therefore, to assess the sensitivity to the chord, a second chord approximation was used, which is shown in Fig. 4-16a. The resulting force fluctuation is shown in Fig. 4-16b.

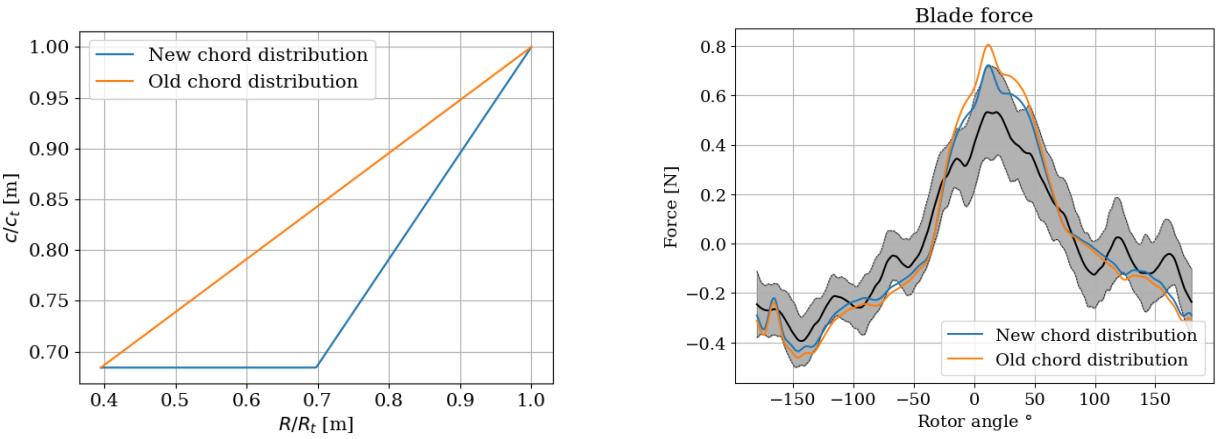

(a) Estimation of chord length

(b) Resulting force fluctuation

Figure 4-16 Sensitivity of chord distribution

As can be seen in the figure, a better agreement with the simulation data is found when using this chord distribution. Therefore, it is recommended an accurate stage-wise chord measurement is done, allowing for an interpolation of the chord at each radial position.

The force $F(\theta)$ from simulation was then decomposed in its Fourier modes using Equation 4-6. Since this was data from a longer time simulation, and not an exactly periodic signal, a Hanning window was first applied to $F(\theta)$.

$$\tilde{L}(w) = \frac{1}{2\pi} \int_0^{2\pi} F(\theta) e^{-iw\theta} d\theta \tag{4-6}$$

The resulting Fourier decomposed Force modes are presented in Fig. 4-17, comparing the force as found by the model using the inflow distortion to the actual measured force, where one standard deviation is indicated with error bars.

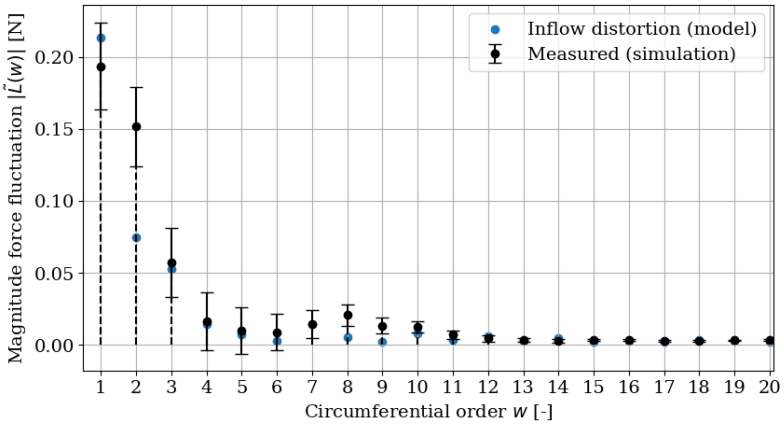

Figure 4-17 Magnitude of Fourier force decomposition

Generally the agreement between the two is good. However, the low-order modes do have some discrepancies, of which mode two is significant. Since these orders do not generate a lot of noise, this is not problematic. What can furthermore be noted is a clear under prediction of modes 8 and 9, and to a lesser extent order 10. This is likely due to the presence of the stators. A total of 9 stators are present, causing fluctuations in the force, which are best visual in Fig. 4-12. Since the stators are unequally spaced, instead of only affecting order 9, they also affect orders 8 and 10. In the model, only the inflow distortion is used, hence the potential effect of the stators cannot be captured. It is therefore recommended to implement some effect of the stator on the rotor force, taking into account the distance to the stator, and the width of the stator.

4.2.3 Verification of noise propagation

In this subsection, the part of the model that calculates the far-field noise based on the blade's unsteady loading is verified. Data obtained from the PowerFLOW simulations were used to do so. The input to this part of the model are the force modes obtained from simulations and Fourier decomposed as was shown in the previous section (black dots in Fig. 4-17). These force modes were used as input to Equation 3-12, to calculate the tonal, far-field sound generated by a single blade.

As verification, this was compared to the Far-Field Analysis tool in PowerACOUSTICS. In this tool, the far-field acoustics is calculated based on the measured surface pressure over time. A Curle formulation of the Fhowks-Williams-Hawking analogy is used to do so. A solid formulation is used as the pressure is measured on the surface. This method differs in a few ways from the approach adopted here. Most importantly:

- In PA, the monopole and dipole contribution is calculated, instead of just the dipole here. This is not expected to change the results, as the loading term is dominant at this Mach number and these types of blades
- A distribution of monopoles and dipoles is used in PA, whereas a single, rotating dipole is used in this approach, which is located at $R_m = 0.7R_t$. This means blade compactness has to be considered when comparing the (higher frequency) results.
- The radial component of the force is ignored in the analytical approach, as it is assumed to be negligible compared to the axial and tangential forces.
- In the analytical approach, only the tonal (periodic) noise is calculated, whereas a continuous spectrum is calculated based on the wall pressure fluctuations in PA. This is because only the stationary part of the flow is considered in the analytical approach.

First, the results for a single blade are shown, after which the summation over the blades taking into account phase interference is shown.

Single blade

The acoustic results from the model are compared to the simulation results in Fig. 4-18 and Fig. 4-19, where the averaged FFA (Far-Field-Analysis) for the blades is used as verification. This is the result on the fan axis, and on 45° away from the fan axis, respectively.

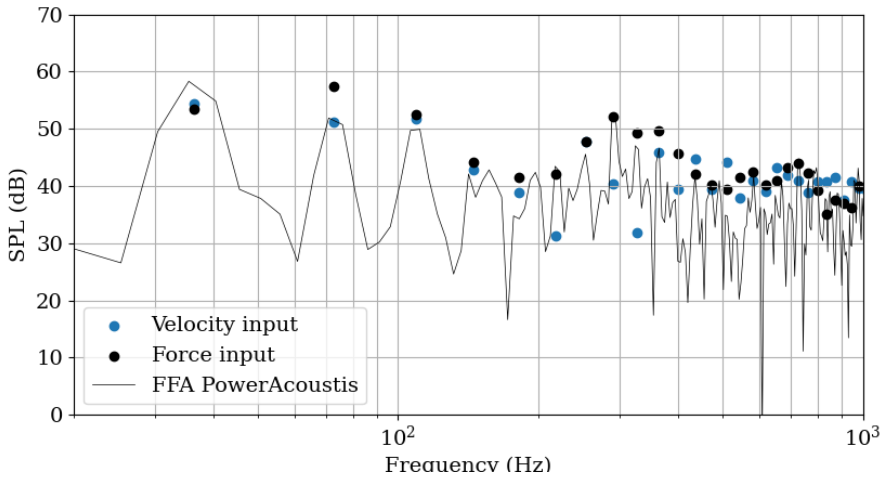

Figure 4-18 Acoustic verification one blade (on axis)

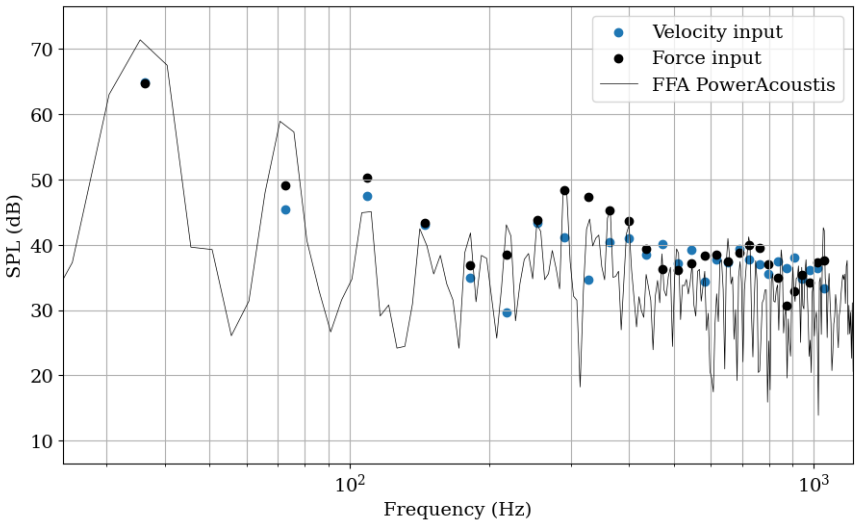

Figure 4-19 Acoustic verification one blade (45° from axis)

As can be seen in the figures, when the measured force is used in the model, the results correlate well to simulation, indicating the noise propagation is correctly calculated. What can also be seen is that the tones corresponding to force modes 8 and 9 (at approximately 300 and 330Hz) are underestimated when the inflow velocity is used as input, which is expected.

What is furthermore good to note is that the compactness assumption still seems valid up to 1kHz, even though the Helmholtz number is already larger than 1 (when using the blade radius as characteristic length). Therefore, this shows that the fluctuations happen on a small portion of the blade, close to the tip.

Entire rotor

When summing the contributions of each blade to get the spectrum for the entire rotor, it was observed that the results are extremely sensitive to the angular positions of the blades. To demonstrate this, the angular positions as measured in CATIA were each given a random change in the range of ±1.0°, while ensuring that the total angle spacing was still equal to 360°. This was done three times (three different, slightly altered spacing), and the resulting noise spectrum is shown in Fig. 4-20.

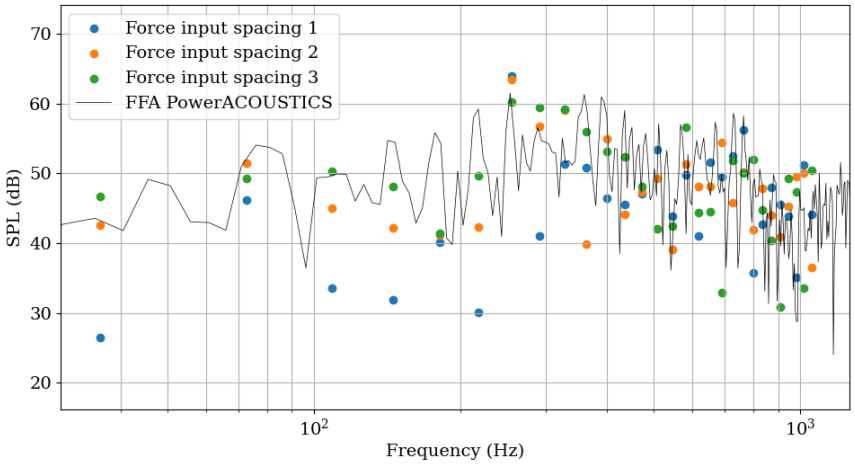

Figure 4-20 Acoustic results entire rotor with varying blade spacing

As can be seen in the figure, the magnitude of the tones varies significantly with small changes of angular spacing. Since the actual rotor blade spacing can't be measured with an accuracy of less than 1° in CATIA, it is not possible to accurately predict all tones using the equations given in Sec. 3.1.3. An exact, accurate blade spacing from the fan supplier is needed to get satisfactory results.

What is seen, however, is that the tones at BPF and harmonics vary only slightly, since the destructive interference (with the small angular variations in the current rotor design) is limited. It is therefore possible to predict the BPF tone of the entire rotor within around 5dB accuracy.

One further verification step that was done was to give the rotor an equal spacing of blades. When doing so all tones except for multiples of BPF should cancel, which is shown in Fig. 4-21. The tones are also higher than the simulation results, which should be the case since now total constructive interference takes place.

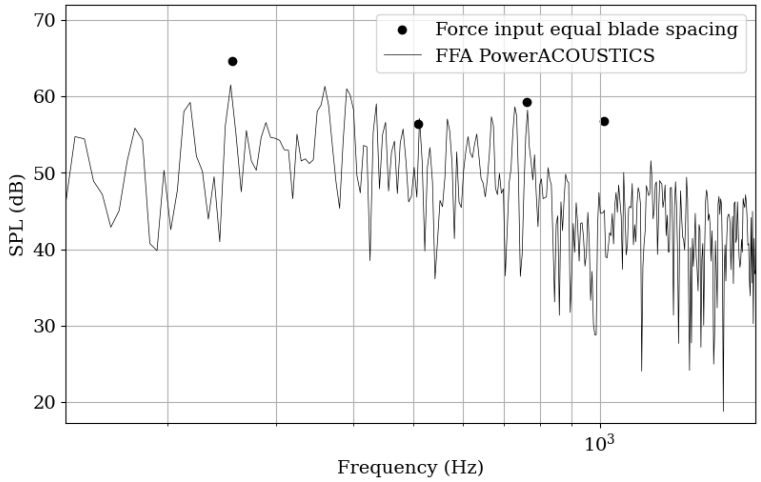

Figure 4-21 Results with equal blade spacing

4.3 Experimental validation

In this section, the simulation data will be validated with experimentally obtained data. Since the measurement time in experiment is 2 orders larger, it is important to understand the stability of the tones when comparing these results, which is done in Sec. 4.3.1. The acoustic comparison of the fan without obstruction is then done in Sec. 4.3.2. Comparisons of the noise with obstructions will be presented later, in Chapter 5.

4.3.1 Stability of tones

Before comparing the results from simulation to experiments, it should be noted that the tones can fluctuate in time quite significantly, with around 2-4dB according to Sturm et al [80]. Since the simulation measurement time is much shorter than in experiment, it is useful to know the unsteadiness of the tones over time. This is also important to assess to what degree a tone can be controlled, according to Moreau and Magne [57]. The more stable the tone, the better control is possible. An indication of the stability of the noise over time can be obtained by inspecting the spectrogram, as shown in Fig. 4-22.

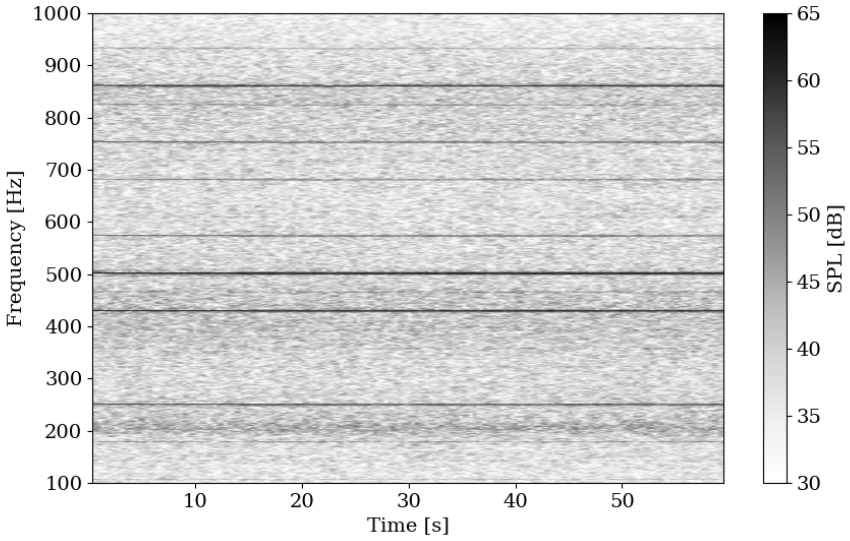

Figure 4-22 Spectrogram of experimental measurement

It can be seen in the figure that the tones indeed vary over time. However, it is hard to see the amplitude of these fluctuations. It is therefore better to inspect this for different tones separately. This was analyzed for both simulation and experiment.

An approach would be to slice the spectrogram at the frequency (bin) of the tone of interest. However,in the simulation, the limited measurement time (around 0.2 seconds) imposes a constraint on the minimum frequency resolution $df_{min} = 1/T$ of the spectrogram. A compromise has to be found between the frequency resolution (Equation 4-7) and the temporal resolution (Equation 4-8), when picking the block size.

$$df = \frac{f_s}{N} \tag{4-7}$$

$$dt = \frac{N}{fs}(1 - O) \tag{4-8}$$

Here f_s is the sampling frequency, N is the block size, and O is the overlap coefficient. This means dt and df are inversely proportional. With an overlap of 50%, and a bandwidth of for example 20Hz, dt is around 0.025s, meaning only about 10 timesteps in a simulation. It was seen that this is insufficient to analyze the fluctuations of the tones with adequate frequency and time resolution.

This constraint is physical, using another method still poses a compromise. However, since N has to be a multiple of 2, using the method presented hereafter provides more freedom in the bandwidth chosen. More importantly, the center frequency of the bands investigated can be chosen, which was found to be important to accurately capture the fluctuations of a tone.

Demodulation using the Hilbert transform

Therefore, a different approach was used, which was also done by for example Moreau et al [57] and Gerard et al [30]. To find the temporal fluctuations of a tone, the Hilbert transform was used. The signal was first band-filtered around the tone's frequency, using a second order Butterworth filter. The mean was subtracted and the signal was zero-padded to reduce the filter-induced transient response at the beginning and end of the signal.

The Hilbert transform was then taken, showing the temporal fluctuations of both the amplitude and frequency modulation of the signal, effectively demodulating the signal. An example of the bandpass-filtered pressure and corresponding Hilbert transform amplitude is shown in Fig. 4-23. The thin black line indicates the band-filtered pressure and the thick line indicates the amplitude of the Hilbert transform.

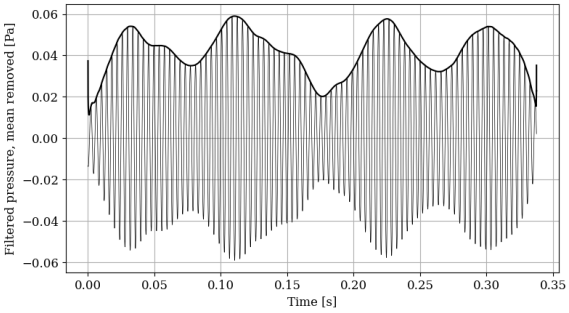

Figure 4-23 Band-filtered pressure and corresponding Hilbert amplitude

It was then investigated what the effect of the bandwidth on the fluctuations is, which is shown in Fig. 4-24. The band-filtered pressure around BPF is now converted to SPL, and the corresponding instantaneous frequency is shown as well. A 5-second window from an experimental measurement is shown here, around halfway the measurement.

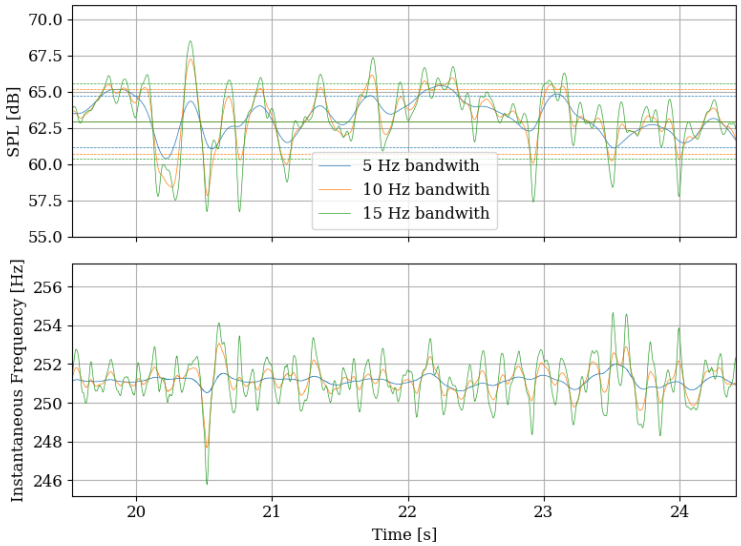

Figure 4-24 Effect of the bandwidth on Hilbert demodulation, dotted line indicates 1 standard deviation

As can be seen in the figure, taking a larger bandwidth will show more fluctuations in the resulting Hilbert

transform. This also results in a larger standard deviation for wider bandwidths, indicated with the dotted line. This can be explained by the slight variations in the frequency of the BPF (for example slight variations in the non-uniform inflow). A compromise has to be made, however; taking a too-wide bandwidth might include noise other than the intended tone. Especially for tones that do not stand out from the broadband spectrum as much, increasing the bandwidth further resulted in an overestimation of the tones

A bandwidth of 10 Hz was therefore decided to be used in further analysis. This does capture the fluctuations of the SPL to a satisfactory extent, while limiting the frequency variations to 10Hz, which is feasible.

Stability in experiment
The Hilbert transform was then taken for each of the harmonics of rotational frequency. This is then plotted together with the Fourier decomposed spectrum in Fig. 4-25. The mean of the Hilbert transform is indicated with dots, and the error bars indicate one standard deviation from the mean, which is a measure of the stability of the tone.

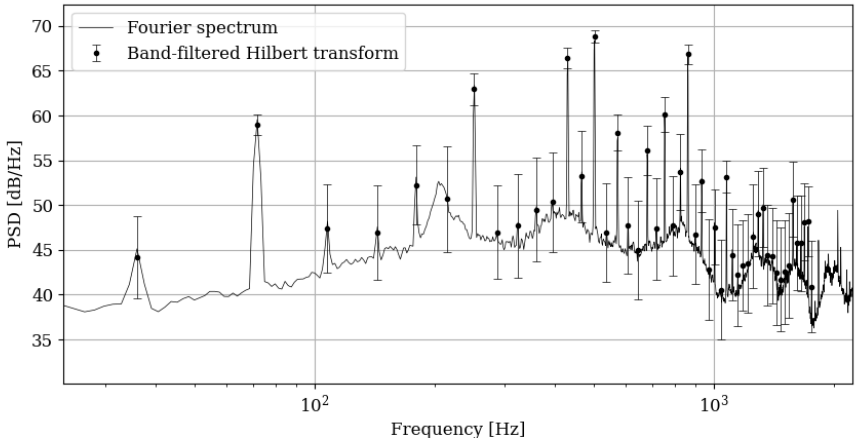

Figure 4-25 Tones found by Hilbert transform, errorbar indicates standard deviation

As can be seen in the figure, in general, the higher tones are more stable, but still, a standard deviation of 2-3 dB is seen for most of the tones.

Conclusions on tone stability
The tones fluctuate with 3-5dB around their mean value, which was also seen in the simulation (but for a much shorter time). This will make the control of the tone with an obstruction harder. However, noise reductions should still be possible, especially on the fan axis. The reason for the fluctuations is not evident, no periodicity could be retrieved, so it is likely due to random variations in the non-uniform inflow. When comparing simulation to experiment (with a different measurement time), this instability should be taken into account for a fair comparison.

4.3.2 Primary noise

The fan's primary noise, (fan noise without obstruction/baseline), is first compared to the simulation results. Next, the broadband spectrum is correlated.

Overall Sound Pressure Level
The OSPL is shown in Fig. 4-26. As can be seen in the figure, the OSPL is estimated within 1.5dB accuracy at the three microphone locations.

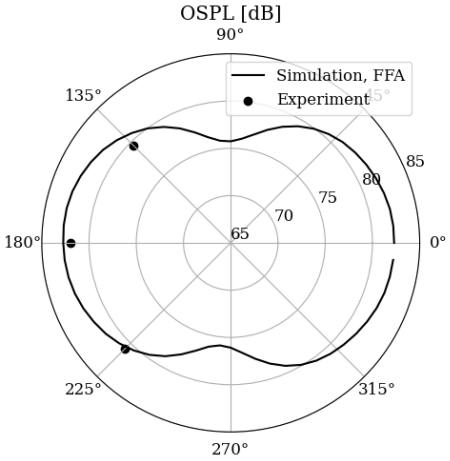

Figure 4-26 OSPL experiment vs simulation

Tonal noise

The narrowband spectrum up to 2kHz is shown in Fig. 4-27 in Power Spectral Density with a bandwidth of 10Hz, which was the finest the simulations can go, following Nyquist and a measurement time of 0.2s.

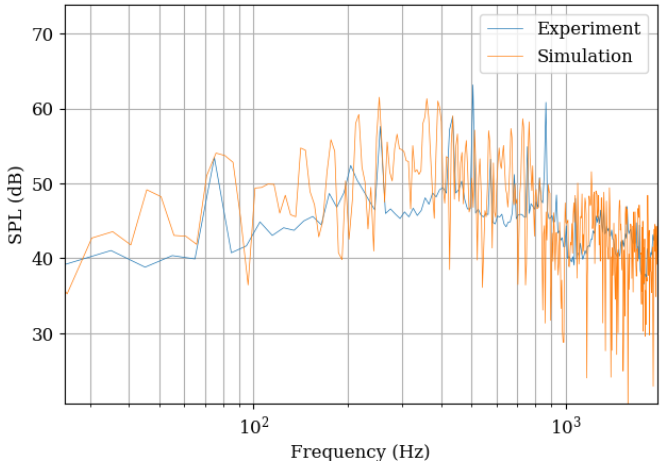

Figure 4-27 Narrowband (10Hz) spectrum

As observed in the figure, it is hard to distinguish the tones in this bandwidth. Furthermore, as we know the tones can vary in the range of 5dB (Fig. 4-24), and the measurement time of the two is not equal, it is useful to compare the band-filtered signal.

To make a fair comparison between simulation and experiment, the Confidence Interval (CI) was used. To do so the data was first down-sampled so the sampling rate of the simulation and experiment match. A sampling rate of 50 Hz was verified as sufficient to capture the fluctuations of the tones. Then, the Standard Error (SE) of the mean is found by:

$$SE = \frac{\sigma}{\sqrt{n}} \tag{4-9}$$

Where σ is the standard deviation and n is the number of samples.

The Confidence Interval (CI) is then found by:

$$CI = \overline{SPL} \pm SE * Z_c \tag{4-10}$$

Here, $\overline{SPL}$ is the mean sound pressure of the tone, and Z_c is the critical value, following the normal values for confidence intervals. [1]. $Z_c = 1.96$ was chosen, corresponding to a 95% confidence interval.

The tones, including the confidence interval of 95% indicated with error bars, is then shown in Fig. 4-28. They are presented as frequency harmonics, since the RPM in experiment was observed to be slightly lower compared to the simulation (2153 vs 2180 rpm).

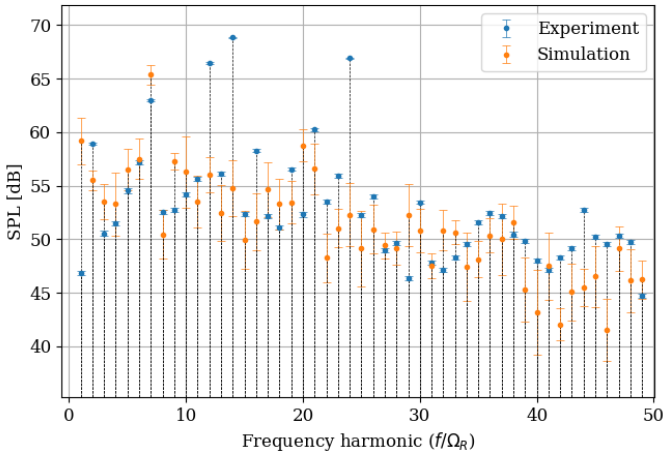

Figure 4-28 Tones in simulation vs experiment, error-bar indicating 95% confidence interval, microphone on axis

As can be seen in the figure, the confidence interval is much larger in simulation. This is mainly attributed to the measurement time, which influences the number of samples n. The standard deviation was in the same order of magnitude. This demonstrates that the uncertainty of the predicted tone compared to using a longer simulation is relatively large, around 3dB for most tones.

Most of the tones are predicted within 5dB accuracy, especially when taking into account the confidence interval. Nevertheless, outliers of over 10dB difference are also observed, see for example harmonic 12, 14, or 24. The simulation also shows a similar 'trend' in the magnitude of the tones, however, it is not able to predict the dominant tones. In the simulation, the BPF was the largest, whereas higher harmonics were louder in the experiment.

No evident reason for this discrepancy was found. A possible reason is the difference in setup, where no hard floor was present in the experiments. This might change the re-circulation around the fan, slightly changing the non-uniform inflow and hence tonal noise. A second possible reason could be differences in the geometry. As was previously shown, the blade spacing can have a significant impact on the acoustic results. The fan may have a slightly different blade spacing in simulation and experiment. Finally, small differences in force fluctuations can cause significant differences in acoustics. It is possible that not all force fluctuations can be predicted with sufficient accuracy in simulation.

Broadband spectrum

The broadband spectrum comparing simulation to experiment is shown in Fig. 4-29, presented in 12th-octave bands.

[1] URL:http://www.ltcconline.net/greenl/courses/201/estimation/smallConfLevelTable.htm

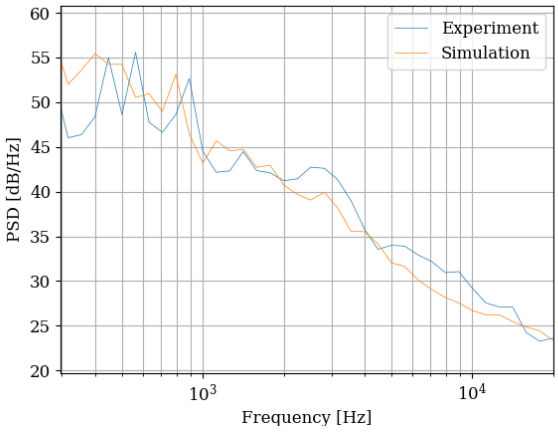

Figure 4-29 Broadband spectrum in 12th octave

As can be seen in the figure, the correlation is quite good, however, the simulations underpredict the noise above 2kHz. It was observed in Sec. 4.1.3, that this region was still increasing with mesh size, so the very fine mesh correlates better in this region, see also Appendix C. However, this is not the focus of this study.

5 Results

This chapter will present the results of the thesis. First, the primary fan noise, or noise without obstruction, is analyzed in Section 5.1. Next, the design of flow obstructions is discussed in Section 5.2. Finally, Section 5.3 will explain the optimization and resulting noise reductions from flow obstructions.

5.1 Analysis of the fan primary noise

5.1.1 Distinguish noise sources

Since the FWH solution and the probe measurements in the simulation correlate well, it is possible to distinguish the contribution of different surfaces on the far-field noise, using the FWH analogy. This is shown in Fig. 5-1. Both the narrowband spectrum is shown at lower frequencies, and the broadband spectrum.

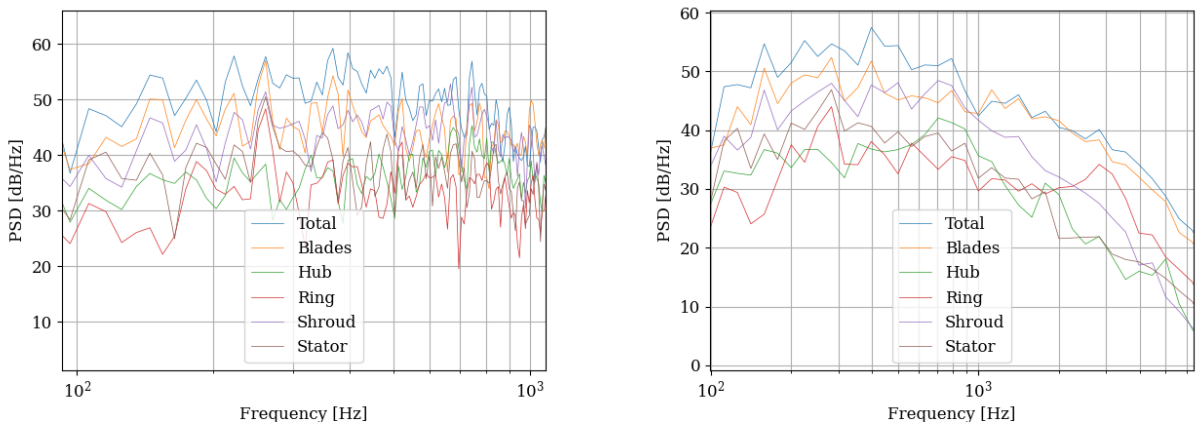

(A) Narrowband

(B) Broadband (12th octave)

Figure 5-1 Noise spectra divided

From the figures, it is clear that most of the noise is generated on the blade surfaces, followed by the shroud surface. Both the tonal noises at lower frequencies, but also high-frequency broadband noise, which is in line with the literature described in Section 2.2.

To better understand where on the blade the noise at BPF is predicted in simulation, the rotating power spectrum is used. Power spectrum results are calculated separately for a number of angular sectors of rotation, averaging the total number of rotations. Transient results for each band are recorded for a single rotation by linear interpolation as a measurement cell passes through each overlapping angular segment. A movie of the averaged fluctuation along the circumference is then created, which allows to show the angular dependence of

frequency band results. In this case, the noise at BPF is shown, and a snapshot of the front and rear of the generated movie is shown in Fig. 5-2.

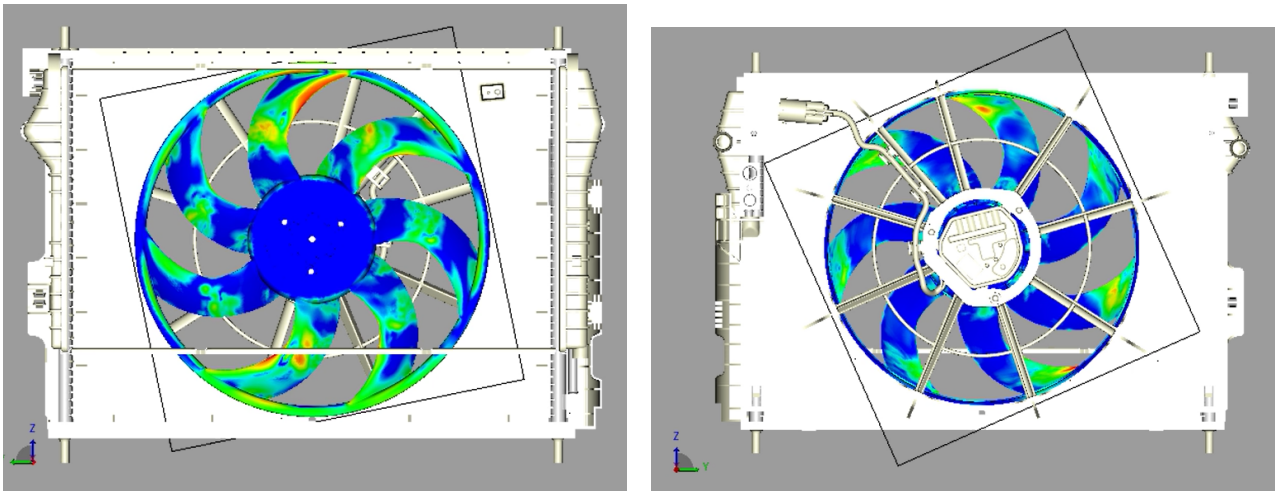

(A) Front (B) Rear

Figure 5-2 Rotating dB spectrum

As can be seen in the figure, both at the tip of the fan and in the transition from radiator to no radiator, fluctuations are high suggesting the noise is originating from these locations.

It was furthermore investigated what the velocity of the tip vortices is, which is shown with an isosurface in Fig. 5-3. This would result in the subharmonic humps around 180Hz, which could be the corresponding peak in Fig. 5-1a, but this is uncertain.

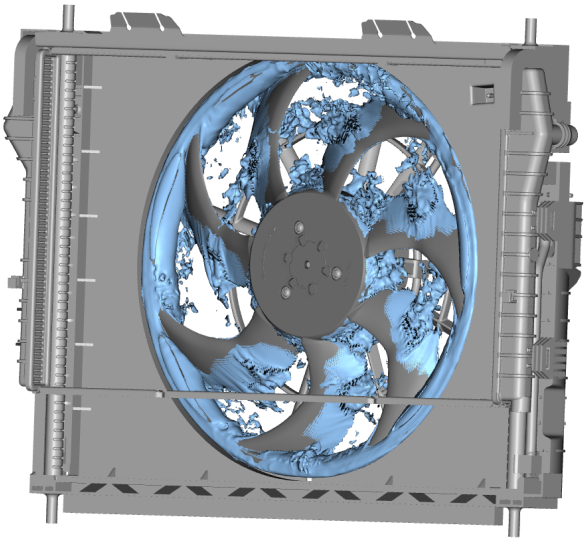

Figure 5-3 Iso-surface velocity magnitude 15m/s

5.1.2 Modal analysis

Flow obstructions are designed to target specific acoustic (azimuthal) pressure modes. It is therefore important to know the dominance of each of these modes on different frequency harmonics, which can be achieved using a modal analysis.

Practically, this was done in two ways. First of all, using an array of microphones and employing a 2D-DFT (two-dimensional Discrete Fourier Transform), given in Equation 5-1.

$$P_{q,n} = \frac{1}{M}\sum_{j=0}^{M-1}\frac{1}{N}\sum_{k=0}^{N-1} p(\theta_j, t_k)e^{-2i\pi(jq/M - kn/N)} \tag{5-1}$$

In this equation, j indicates the microphone, k indicates the timestep, M the number of microphones, N the number of timesteps, q the pressure mode order and n the frequency harmonic. In this case, the sound on an array of 60 microphones 1.5m upstream of the fan (radius 1m) is obtained using the FWH analogy, after which Equation 5-1 is used to decompose the signal in time and space. The advantage of this is that the location of the modal analysis can still be determined after simulating.

The resulting modal decomposition at the BPF is shown in Fig. 5-4a and a complete modal map is shown Fig. 5-4b, visualizing the composition on all harmonics of the rotational frequency.

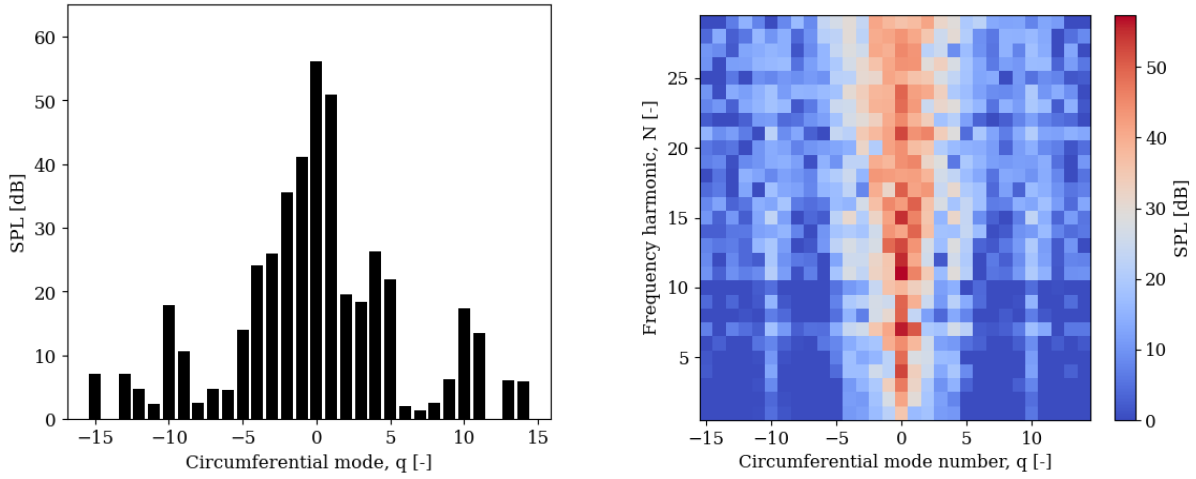

(A) Modal decomposition at BPF

(B) Modal map

Figure 5-4 Modal analysis using FFA microphone array

As can be seen in the figure, when in the far-field, pressure mode zero is almost always the dominant sound radiator. This is valuable information, as it aids in the choice of lobe number when targeting specific tones in unequally spaced fans, when no modal analysis is feasible: using the same number of lobes as the targeted harmonic ($q = N - s = 0$) will likely yield decent noise reduction.

Secondly, the circular plane measurements, described in Sec. 3.2.4, were used to get a modal decomposition along azimuth and radius. In the results below, only 1 radial station is specified, since only the circumferential decomposition is of interest in this application. The modal decomposition of three upstream planes is shown in Fig. 5-5.

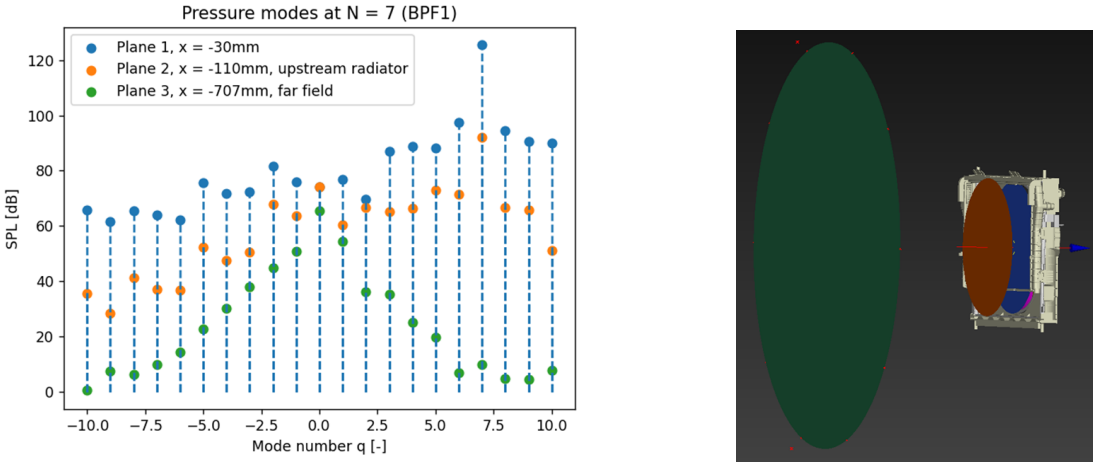

(A) Modal decomposition

(B) Measurement planes used

Figure 5-5 Modal analysis of different upstream planes

As can be seen in the figure, in the near-field of the fan, pressure more $q = 7$ has a strong contribution. This contribution is hydrodynamic however, it is created in the vicinity of the blades but does not travel upstream, as can be seen for the modal decomposition of plane 3. The mode arises from the steady blade loading $q = N - s = 7 - 0 = 7$, and rotates along with the blade. It can be visualized by bandpass filtering the time derivative of pressure at the BPF, as shown in Fig. 5-6. From Fig. 5-5a, it is clear that the propagation of the modes is related to the mode number, as explained in Sec. 2.2.1. The lower the mode number, the more efficient the propagation.

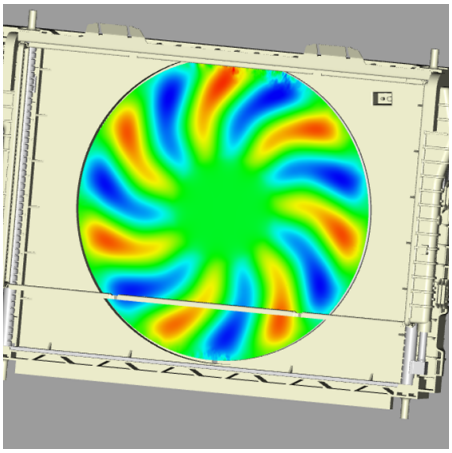

Figure 5-6 Time derivative of pressure bandpassed at BPF

5.1.3 Experimental results primary noise

Whereas the advantage of CFD is the possibility to visualize the flow and understand the physical phenomena better, the disadvantage is that only short measurement times are feasible. Experimental results therefore provide a noise spectrum with a much finer frequency resolution, which gives some additional insights, given in Fig. 5-7.

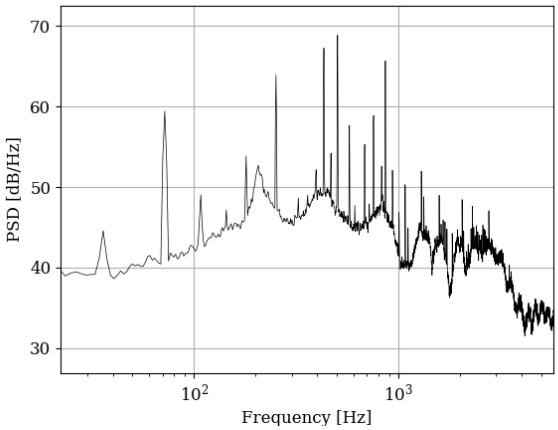

Figure 5-7 Experimentally obtained spectrum

With this fine resolution, the tones now clearly stand out from the broadband spectrum. This also reveals the presence of the tip-leakage noise frequency 'hump' at around 210Hz, slightly higher than in the simulation. This also seems to have some harmonics, although these fluctuations can also be due to interference which will be discussed shortly when comparing different duty cycles.

Varying duty cycle

The effect on the Overall Sound Pressure Level when changing the duty cycle (and hence RPM), is shown in Fig. 5-8a. As can be seen in the figure the OSPL varies almost linear with fan rotational frequency.

In Fig. 5-8b, the noise spectra for these four duty cycles are shown.

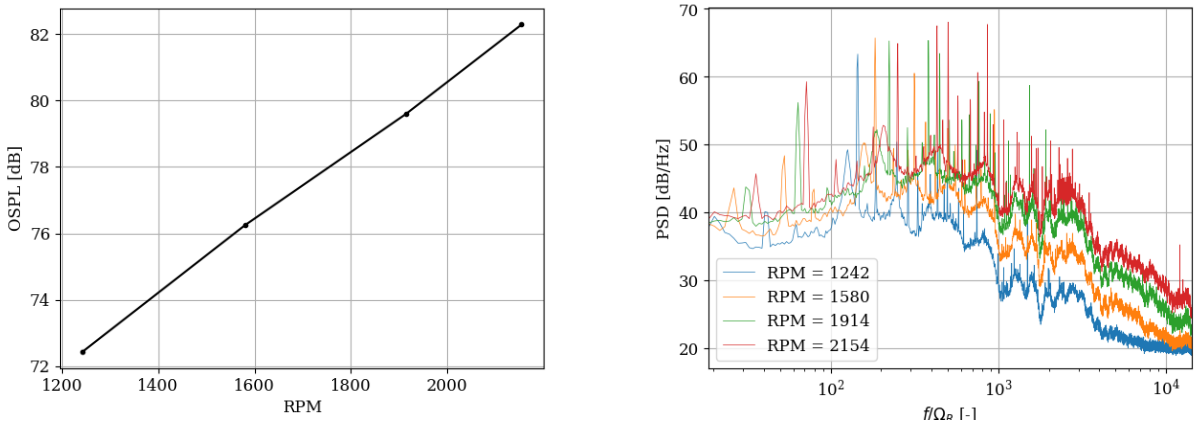

(a) OSPL vs RPM

(b) Noise spectra varying RPM

Figure 5-8 Effect of RPM on noise

A few things can be observed from this spectrum. In terms of tones, the BPF remains strong at low duty cycle, whereas tones at higher harmonics are prominent for the maximum duty cycle case.

What can furthermore be noted is that the fluctuations in the higher frequencies are constant for different duty cycles. This points at a likely interference happening, possibly from the arc or the structure on the ground. Since the hump in the spectrum that was previously attributed to tip-leakage noise shifts with rotational frequency, this indeed confirms that this is an aerodynamic noise source, and no interference.

Removing radiator

Removing the radiator alters the noise in a few ways, which is demonstrated in Fig. 5-9 below.

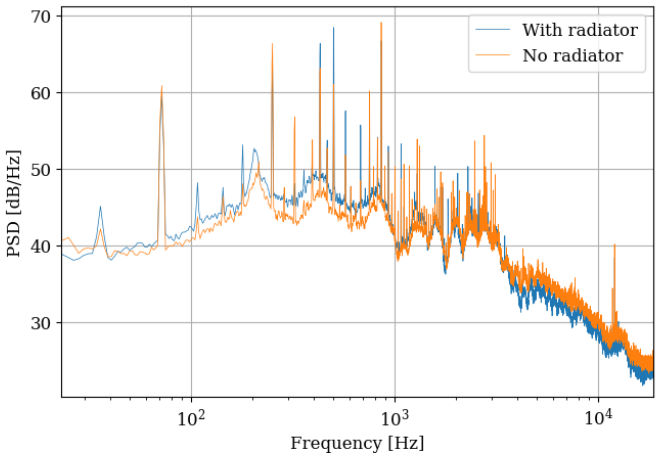

Figure 5-9 Effect of removing the radiator

The low-frequency broadband noise (up to around 1kHz) is increased with a radiator in place, in line with Czwielong [13] and Park [65]. Most notably the tip-leakage hump in the spectrum is higher with the upstream radiator. This is likely due to the higher pressure difference, resulting in more backflow. The high-frequency noise is lower with a radiator in place. This could be due to the lower flow rate, resulting in less trailing edge noise. Alternatively, it could be due to some acoustic transmission loss across the radiator as shown by Allam and Albon [2]. The tones are also affected by the radiator. Whereas some tones are reduced with the upstream radiator (as was also found by Wu et al[85]), most tones are increased, similar to what Park et al [65] observed. This shows that the radiator introduces some non-uniformities in the stationary inflow and reduces some non-uniformities.

5.2 Obstruction design

The design of the obstruction was done using the analytical model in Python. The design objectives are as follows:

- The produced tone should be as loud as possible, with respect to mass flow loss
- The obstruction should affect 1 tone (specifically mode) without affecting its harmonics. In other words, the obstruction's harmonic content rate should be as low as possible.

Since in the literature, sinusoidal obstructions are the most harmonically selective [32][31] and effective [36], compared to for example cylindrical or trapezoidal obstructions, this was the design direction that was chosen.

Instead of using a single sine on the outer radius of the hub (Fig. 5-10a), a double-sine design was considered, which is shown in Fig. 5-29b. The idea of this design was to check if it allows for an even more selective tone. Furthermore, placing the obstruction on the outer radius was investigated, shown in Fig. 5-10c.

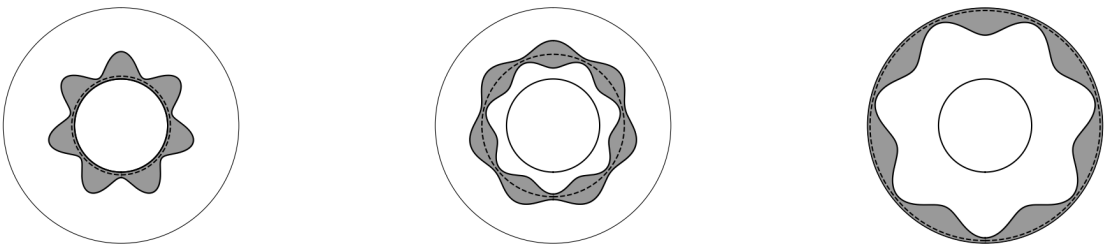

(A) Sine on the hub (inner sine) (B) Double sine (C) Sine at tip (outer sine)

Figure 5-10 Considered obstruction geometries

These designs were then qualitatively compared on the criteria mentioned above. The mass flow loss is found by integrating the wake deficit and multiplying it with the rotor area (tip-hub) to obtain the flow rate loss due to the obstruction, Q_{loss}. It is presented as a percentage of the total flow rate Q_{tot}, which is known from supplier data.

The harmonic selectivity is quantified using the harmonic content rate D, which is given by Equation 5-2. This is a slightly adapted version from [32], as in the current approach all harmonics are calculated, instead of only multiples of B.

$$D(\%) = \sqrt{\frac{\sum_{w=0}^{w_{max}} |\tilde{L}(w)|^2 - |\tilde{L}(w=7)|^2}{\sum_{w=0}^{w_{max}} |\tilde{L}(w)|^2}} * 100 \tag{5-2}$$

So, the lower the harmonic content rate, the better, as it indicates less energy is contained in the harmonics. The resulting design parameters, shown as a function of the lobe amplitude, are then given in Fig. 5-11.

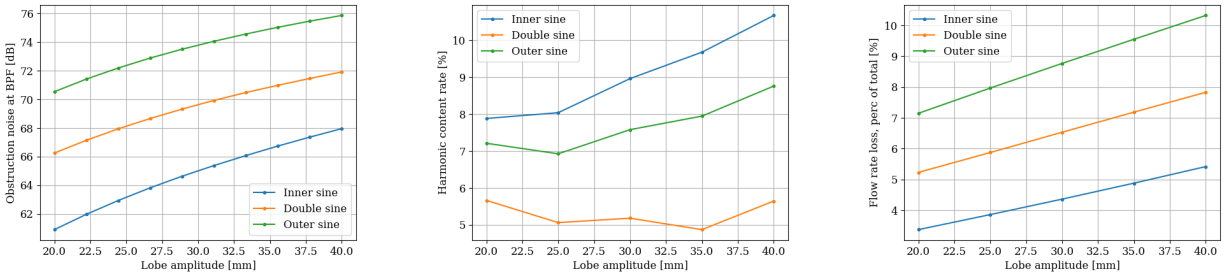

(A) Obstruction noise (B) Harmonic content rate (C) Flow loss

Figure 5-11 Design parameters as a function of lobe amplitude

As can be seen in the figure, the outer-sine obstruction creates a much louder tone, but it also generates a bigger loss in flow rate at a given lobe amplitude. What is also good to note is that the relation between lobe amplitude and noise is almost linear, in line with [57]. It was observed however that this line decays for bigger lobes. The hypothesis is that when approaching half of the fan radius, adding extra amplitude does not have as much effect.

In terms of harmonic content rate, the double-sine does indeed perform well, although all of them have a very low content rate of below 10%. It should be noted that the content rate is very sensitive to the Gaussian wake parameter σ_θ, which was estimated from the simulation data.

To make a fair comparison between the different designs, it is better to plot the amplitude of the generated tone versus the flow loss, which is shown in Fig. 5-12.

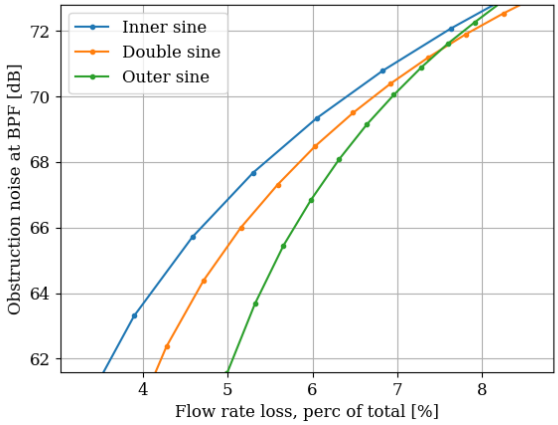

Figure 5-12 Noise from obstruction vs flow loss

As can be seen in the figure, the inner sine has the lowest loss in flow rate for a given desired tone amplitude. Since the harmonic content rate was still satisfactory low, this was also the design that was chosen for simulating and testing.

Using a double sine design could still be useful when targeting multiple modes/tones, an example is shown in Fig. 5-13, targeting mode 7 and 10. This will be explained further in Sec. 5.3.7.

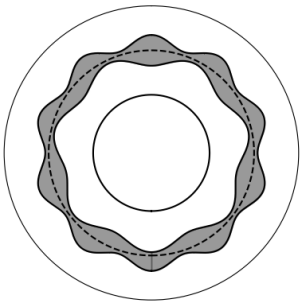

Figure 5-13 Double sine with different lobe number on inner and outer radius

5.3 Flow obstruction results and optimization

This section will present the effects that were observed on the noise when using flow obstructions. Results from the model, simulation and experiments will be presented simultaneously. First, Sec. 5.3.1 will show the optimization of the lobe amplitude, while the phase (angle) optimization is explained in Sec. 5.3.2. Next, the aerodynamic penalty from the obstruction is assessed in Sec. 5.3.5, after which the effect of the obstruction in lower fan duty cycles is researched in Sec. 5.3.6. Finally, Sec. 5.3.7 will expand on the design of multimodal obstructions.

5.3.1 Optimization of obstruction lobe amplitude

To find the optimal lobe amplitude and angle numerically, the method outlined by Moreau [57] was used, as explained in Sec. 3.2.5. To quickly recap, the obstruction was rotated at 200rpm in opposite direction of the fan, effectively generating a secondary tone at Blade Pass Frequency + Lobe Pass Frequency.

The two lobe amplitudes that were simulated were 20 and 40 mm, respectively. The acoustic results showing the tone amplitude of the BPF and the secondary tone induced by the obstruction are shown in Fig. 5-14.

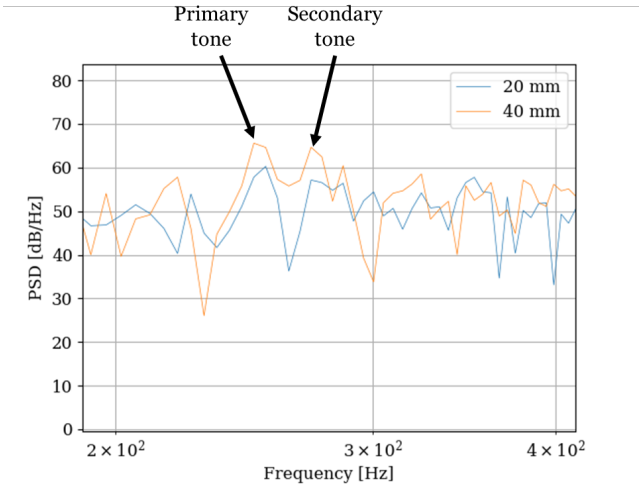

Figure 5-14 Noise at BPF and secondary tone

It was unexpected that the BPF tone changes with a larger obstruction. Nevertheless, the 40mm lobe amplitude matches the secondary tone quite well, and this was then used in further simulations.

Later, finding the magnitude of the tones using the Hilbert transform of the band filtered signal at the BPF and BPF+LPF, revealed some more insights. This is shown in Fig. 5-15.

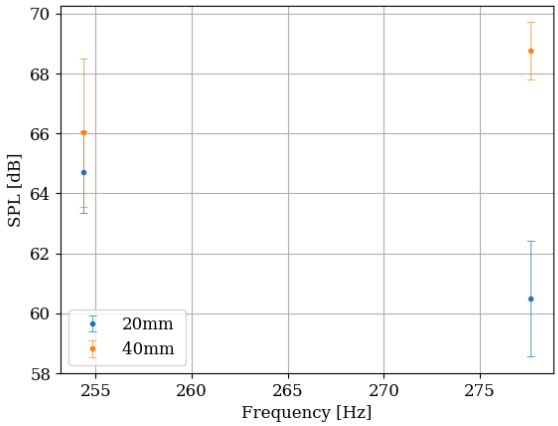

Figure 5-15 BPF and secondary tone from band filtered signal

As can be seen in the figure, the BPF tone for both simulations is within the 95% confidence interval, indicated with error bars. This suggests that the higher tone found in the 40mm case is coincidental: the fluctuations in the tone are randomly higher, due to the relatively short simulation time.

What can furthermore be seen is that the secondary tone is too high with a 40mm obstruction. A better approximation is given in Fig. 5-16. The black line is the primary tone, which was taken as the average of the values found in the simulation without obstruction, and with 20 and 40 mm rotating obstruction.

Using a linear interpolation between the band-filtered results at the specific frequency, a lobe amplitude of $32 \pm 5mm$ is likely better. Furthermore, the analytical tool predicts a 27mm obstruction would yield the desired tone amplitude.

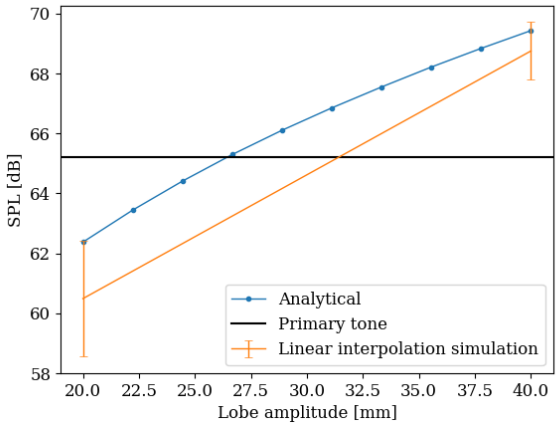

Figure 5-16 Finding the optimal lobe amplitude

This analysis was done after deciding on the lobe amplitude of 40mm, based on the spectral results shown in Fig. 5-14. Hence, the 40 mm obstruction was used in the following simulations.

Experimentally, it is more difficult to optimize the lobe amplitude, without a device to rotate the obstruction. It was done by performing an entire angle sweep and finding the interference pattern. Based on maximum constructive and destructive interference an estimate of the noise from the obstruction could be made. A few alterations were needed, but in the end, a 20mm obstruction was sufficient to cancel the BPF tone of 61 dB.

5.3.2 Optimization of obstruction angle

Analytically, the angle was found by superimposing the obstruction wake definition onto the non-uniform inflow measured in the simulation. By then calculating the BPF tone for a range of obstruction angles, the optimal angle could be found.

In simulation, the optimization of the angle was done by slowly rotating the obstruction (30rpm) in the opposite direction of the fan. By then taking the band-filtered signal containing the BPF (254.3Hz) and BPF+LPF (257.8Hz), the magnitude of the tone can be found over time.

Rotating the obstruction will result in a periodicity of $P = 60/(L * RPM_{obstruction})$, since the obstruction is L periodic. A total of 3 of these periods were simulated and were averaged, the standard deviation is also included.

Since the obstruction is rotating, the angle has to be corrected with Equation 3-17. Since the wake is restricted to rotate through the condenser and radiator, a distance D of 4cm was used, as this is the obstruction to rotor distance minus the thickness of the condenser and radiator. Note that this equation does pose some uncertainty, especially for low rotation velocities [57], but the correction is in the range of 2-3 °, hence relatively small.

Experimentally, the angle optimization was done by simply placing the obstruction in a range of angles and measuring the noise.

Since the primary tone did not always correspond well between simulation and experiment, the data is presented as ΔSPL, for a better comparison. This is shown in Fig. 5-17. Furthermore note that the obstruction in the experiment is also smaller, as the primary tone was lower in the experiment, hence no good interference pattern is achieved with a larger obstruction, making it hard to compare the methods.

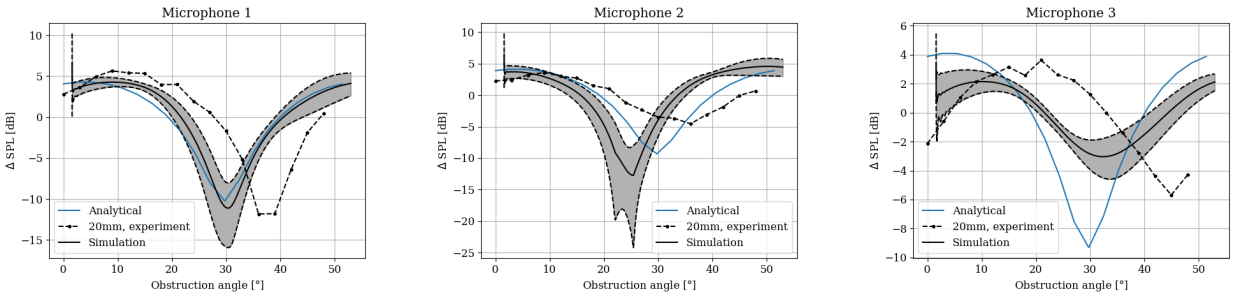

(A) Microphone 1: on axis (B) Microphone 2: 45° (C) Microphone 3: -45°

Figure 5-17 Tone at BPF for different obstruction angles

A few observations can be made from the figures. First of all, the angle of maximum interference is not predicted correctly in simulation, it is off by about 10 °. This is likely because the phase of the corresponding velocity fluctuation (order 7) is not accurately predicted in the simulation. Moreau [57] did find a good agreement of the obstruction angle between experiment and simulation. However, here the primary noise was a very strong tone due to rotor-stator interaction, and hence the phase of this disturbance is evident. Magne et al [51] also saw discrepancies in the angle determination for obstructions in circumferential fans.

What can furthermore be noted is that the analytical tool predicts a similar reduction on all microphone locations (the largest on the axis), which happens at the same angle (30°). This makes sense, as in this model the specific force fluctuation of order 7, or pressure mode 0 (on the BPF) is targeted. However, when comparing this to the other microphones, both the angle of maximum reduction and the magnitude of this reduction change significantly. This hints at the idea that the obstruction also affects pressure modes 1 and -1 (fluctuations of order 6 and 8), besides the intended mode. This may lead to additional attenuation, or a reduction in the noise abatement, depending on the respective phase of the targeted mode. This also explains why the correlation to the analytical model is best on the axis; here only pressure mode 0 propagates sound.

5.3.3 Noise reduction and effect on spectrum

To see the effect of the obstruction on the rest of the spectrum and quantify the noise reduction from the obstruction, experimentally obtained data is presented.

Effect on harmonics of the BPF

It is known that the obstruction has some effect on its harmonics. This was also visible in the experiment, even more than expected based on the low harmonic content rates predicted in Section 5.2. The BPF together with BPF2 is plotted for the microphone on the axis, with lobe amplitudes 20, 30 and 40mm. The effect on BPF3 was negligible, so is not included in the figures. Here the tone without obstruction is subtracted from the result, hence 0 indicates as loud as having no obstruction.

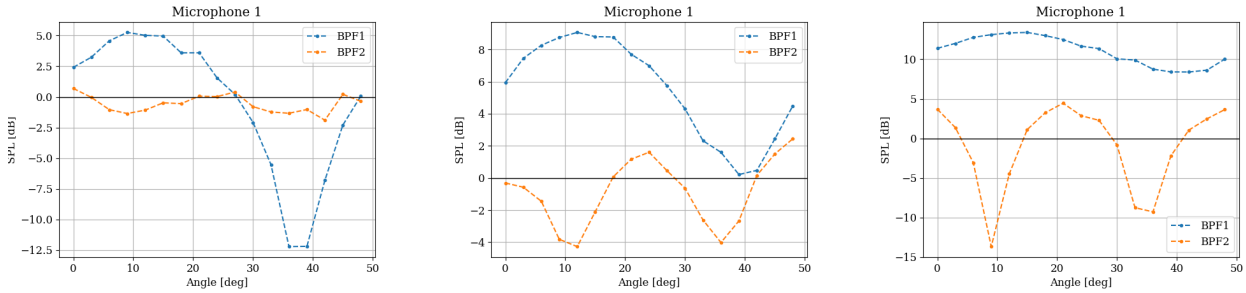

(A) 20mm lobe amplitude (B) 30 mm lobe amplitude (C) 40 mm lobe amplitude

Figure 5-18 Effect on harmonic of the BPF for different lobe amplitudes

As can be seen in the figure, when the obstruction is properly sized to target the intended tone (like the 20mm case), little effect is seen on BPF2. However, for larger obstructions, the second harmonic is quite heavily affected. As expected, the period of the noise as a function of angular position is halved. In this particular case, the harmonic of the BPF is almost in phase with the BPF. This means that a noise reduction is also seen on BPF2 at the optimal angular position. Note that this is often the case as some step non-uniformity in the inflow will cause these harmonics to be in phase. However, this is not necessarily true, when for example considering rotor-stator interaction.

Effect on the rest of the spectrum

Based on Fig. 5-17, the optimal obstruction angle was found to be 39 °, yielding maximum attenuation at microphone 1 and 2, while also reducing the noise at microphone 3. The spectra without obstruction and with obstruction for this position are then compared in Fig. 5-19. As can be seen in the figure, aside from some minor changes to BPF2, the spectrum is left entirely unchanged.

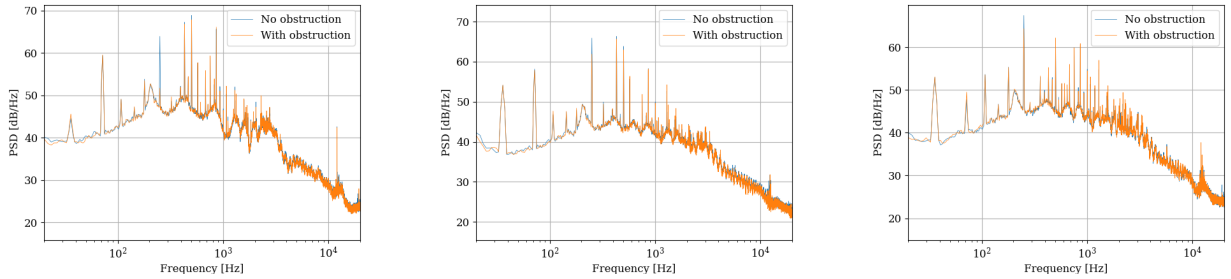

(A) Microphone 1: on axis (B) Microphone 2: 45° (C) Microphone 3: -45°

Figure 5-19 Spectra no obstruction and with obstruction for different mic positions

OSPL and tonal reduction

The reduction in OSPL for microphone 1,2 and 3 is: 0.40, 0.56, and 0.18 dB. However, to make a fair comparison, the fan would have to spin faster to compensate for the loss in mass flow rate. This was done by assuming a linear extrapolation of the OSPL vs RPM (Fig. 5-8a), and assuming a 1% loss in flow rate (for an obstruction of 20mm, this will be explained in Sec. 5.3.5), and assuming the relation between RPM and flowrate is also linear. Compensating for this would then result in a 0.17, 0.33, and -0.05 reduction in OSPL. The TNR is

reduced, for each microphone: 17 to 4dB for microphone 1, 21 to 16 dB for microphone 2, and 22 to 18 dB for microphone 3.

When summing the Tone to Noise Ratio of all the tones that stand out from the broadband spectrum by more than 5dB, the following is found: Microphone 1 goes from 148 to 131 dB penalty, microphone 2 from 143 to 138dB, and microphone 3 from 158 to 154 dB.

5.3.4 Aerodynamics of flow obstruction

The wake of the obstruction is visualized in Fig. 5-20. An isosurface of axial velocity is shown, as well as a slice upstream of the fan.

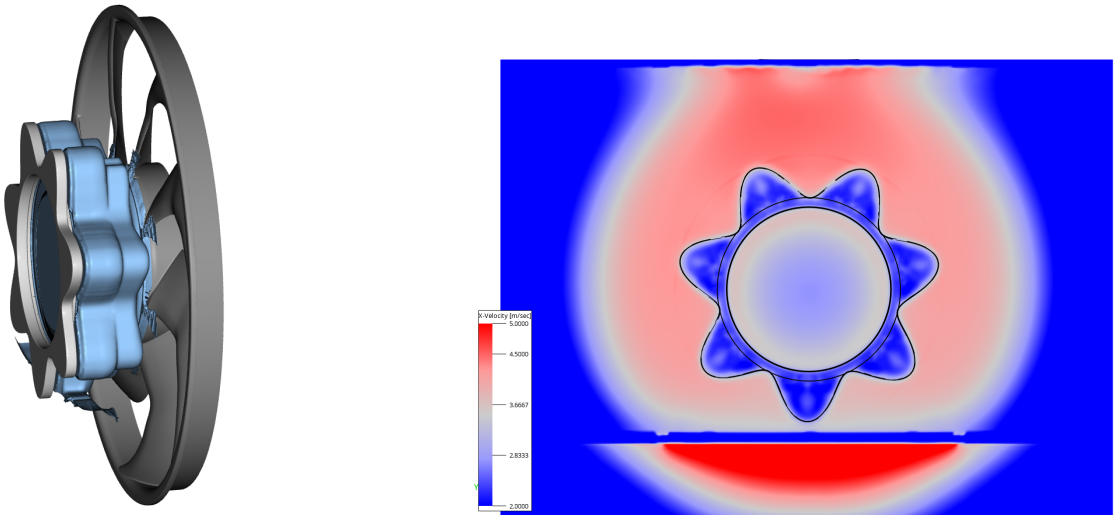

(A) Axial velocity isosurface

(B) Slice 1cm upstream of the rotor

Figure 5-20 Visualization of the obstruction wake

Furthermore, it was observed how the wake propagates through the condenser and radiator. This is shown in Fig. 5-21, where the porous media are the black/grey region.

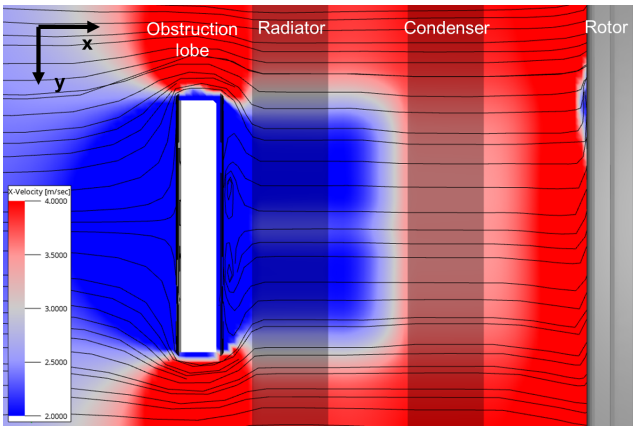

Figure 5-21 Axial velocity obstruction wake, horizontal slice

As can be seen in the figure, the wake is prohibited from rotating through the porous media and is forced straight in, leading to a quick contraction of the streamlines downstream of the lobe. The region of separation (visible with the streamlines) is also small when compared to simulations by Moreau et al [57] where no radiator is present. Furthermore, some stepwise changes are noticeable near the porous media, which was also seen in Fig. 5-20a. It seems that mainly the flow just upstream of the porous media is affected.

Some more observations can be made when inspecting the propagation of the wake in axial direction. This is shown in Fig. 5-22. The axial velocity here is obtained by subtracting a slice from a simulation without obstruction from one with obstruction.

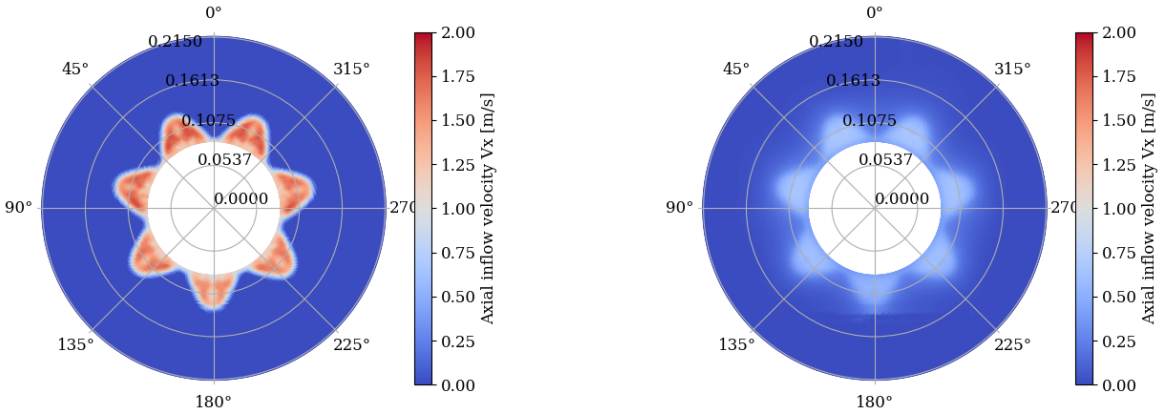

(A) Wake upstream of the radiator

(B) Wake downstream of the condenser

Figure 5-22 Obstruction wake propagation porous media

It can be seen that the velocity defect v_m decreases significantly from just behind the obstruction to downstream of the condenser. The wake is however very defined in both these locations, not a lot of mixing of the wake has occurred. The wake closer to the rotor is visualized in Fig. 5-23. Note that Fig. 5-22b and Fig. 5-23a are the same plot with a different axis range.

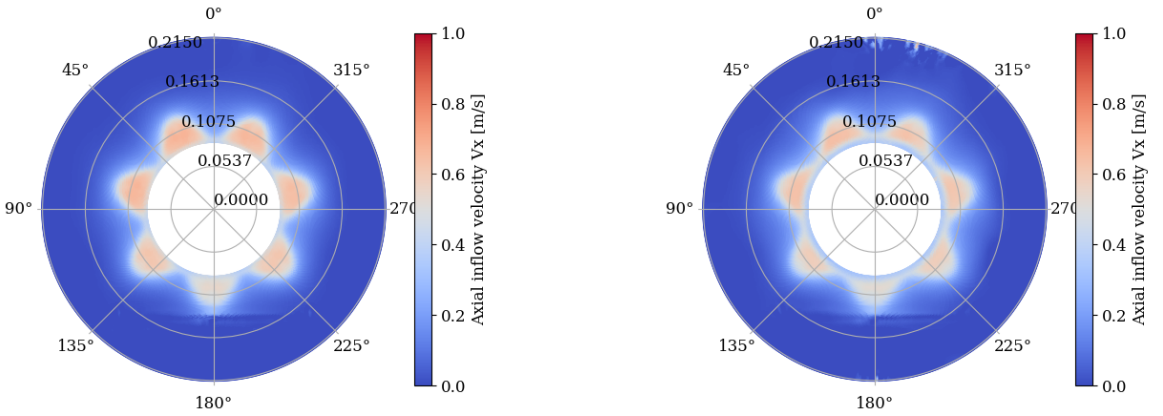

(A) Wake downstream of the condenser

(B) Wake 3mm upstream of the rotor

Figure 5-23 Obstruction wake propagation near rotor

Here it can be observed that the wake velocity defect v_m does not decrease a lot anymore, but the wake does start to mix; it is less defined compared to further upstream.

From these observations, it can be concluded that the porous media do affect the obstruction wake, but do not prevent the wake from propagating to the rotor. It does underline that the wake parameters have to be measured from simulation or experiment as of now.

5.3.5 Aerodynamic penalty from flow obstruction

Using a flow obstruction imposes an inevitable aerodynamic penalty. Since the experiments were not conducted in a separated upstream and downstream chamber, and no inflow was generated, it was not possible to extract

any pressure drop or mass flow loss from the experiments.

In simulation, the pressure and velocity over the actuator plane can be measured and compared, which is shown in Fig. 5-24.

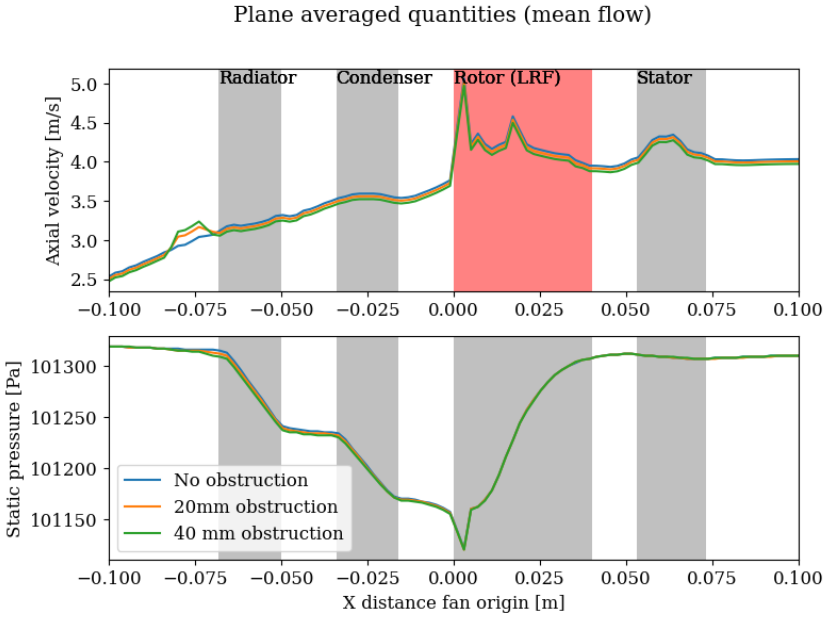

Figure 5-24 Plane-averaged axial velocity and static pressure

As shown in the figure, there is a pressure drop at the obstruction location, but this is 'corrected' by the fan. A lower axial velocity, and hence mass flow, is observed throughout the domain, however.

This is about 0.95% and 1.93% for the 20mm and 40mm obstruction, respectively, which is similar to what was experimentally seen in literature [31], [30] [57].

5.3.6 Obstruction at lower fan duty cycle

As was explained in Chapter 2, the maximum duty cycle (RPM) with no inflow is the investigated operating condition as this leads to the most noise disturbance. However, it is good to know what the effect of the obstruction is at lower RPM, as the obstruction is intended to be passive, and left in place all the time.

This was tested experimentally as it was the fastest and cheapest, with the set-up in place. Two different checks were done: First, the interference pattern (noise versus obstruction angle), was compared for a different duty cycle. This is shown in Fig. 5-25.

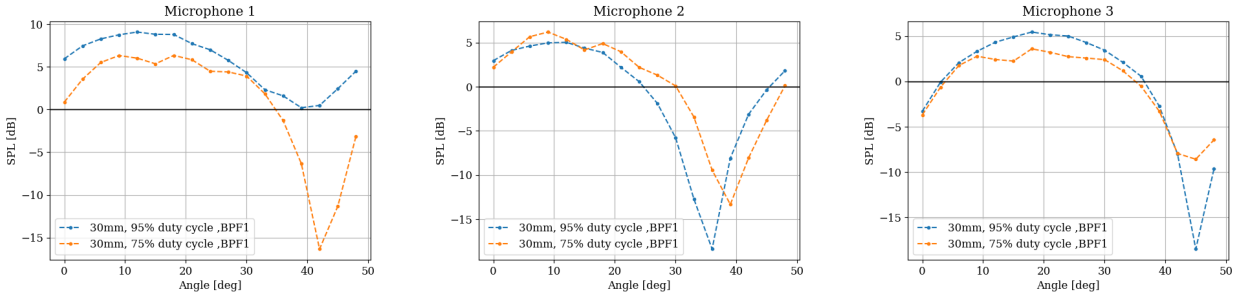

(a) Microphone 1: on axis **(b)** Microphone 2: 45° **(c)** Microphone 3: -45°

Figure 5-25 Interference pattern at lower duty cycle

As can be seen in the figure, the angle for maximum reduction varies only slightly, when going to a lower duty cycle. The changes that are seen could be due to a difference in pre-swirl.

Furthermore, with the obstruction at the optimal position for maximum interference, the duty cycle was reduced to 75%, 55%, and 35%, and the spectra were compared to tests without obstruction. This is shown in Fig. 5-26.

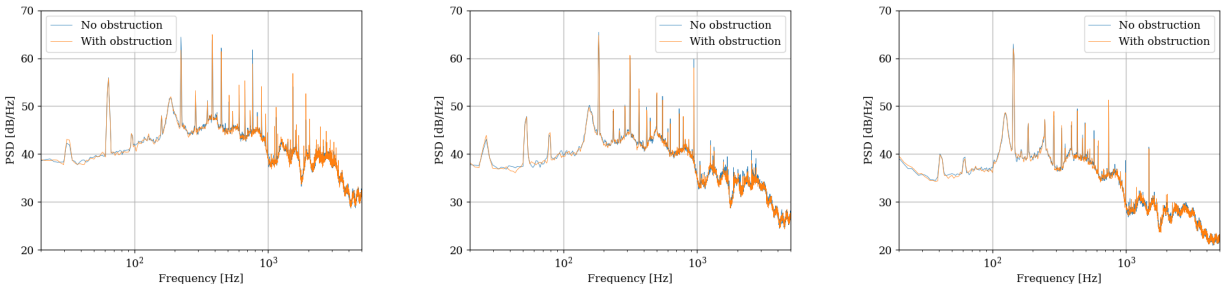

(A) 75% duty cycle (B) 55% duty cycle (C) 35% duty cycle

FIGURE 5-26 Obstruction at lower duty cycles

It can be seen that although the reductions get smaller, still tonal noise reduction is observed at lower duty cycles. Some reduction in the higher harmonics can now also be observed. The reductions in OSPL are around 0.2-0.4 dB. More importantly, the obstruction does not yield any noise increase.

5.3.7 Multi-modal obstructions

With the successful removal of one tone, it was investigated if multi-modal obstructions can attenuate multiple tones. Multi-modal obstructions were investigated before [30], but they were used to cancel multiple modes acting on the same tone (BPF). Since the uneven spacing introduces many tones, it is more useful to cancel or reduce multiple tones instead. This was briefly experimented with, and analyzed more using the python model. Adding a second mode is done using Fig. 2-17.

$$R_2 = R_1 + \frac{B}{2} + \frac{A_1 + A_2}{2} + \frac{A_1}{2} cos(L_1(\theta + \phi_1)) + \frac{A_2}{2} cos(L_2(\theta + \phi_2)) \tag{5-3}$$

Experimental
During experiments, there was some time to test with multi-modal obstructions. Since the phase of both BPF1 and BPF2 was known from previous experiments (Fig. 5-18), it was chosen to target those two modes. The fact that those tones are harmonics of each other and BPF2 is in fact louder than BPF1 does make the optimization more difficult. With tones that are not harmonics of one another, the lobe amplitude and phase optimization can be done separately, whereas here the obstruction to control BPF1 affects BPF2 as well. In the end, no relative phase difference was given to obstruction with lobe numbers 7 and 14, and both were given an amplitude of 10mm. In this way, on each $360/7^\circ$ interval, the combined amplitude was still 20mm, to properly cancel the BPF1 tone. The shape used in testing is shown in Fig. 5-27, and see also Fig. 3-17.

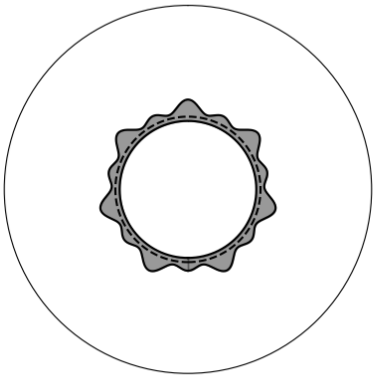

Figure 5-27 Multimodal obstruction shape in testing

An angle sweep was then again performed, and the 2BPF is now clearly affected more, as shown in Fig. 5-28.

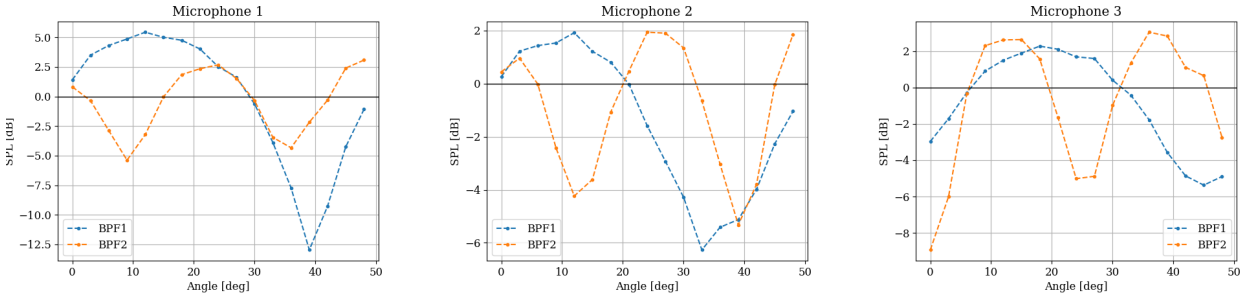

(a) Microphone 1: on axis (b) Microphone 2: 45° (c) Microphone 3: -45°

Figure 5-28 Phase interference for multi-modal obstruction

Although significant noise reductions are seen on all microphone locations for both BPF1 and BPF2 (demonstrating it is indeed possible to reduce multiple tones), further optimization is needed. First of all, as also seen before, the angle of maximum reduction differs for different microphones, hinting at an effect on other modes as well. When targeting just the intended mode (as on microphone 1), the angle of the maximum interference can be aligned by giving one of the lobe numbers a slight phase shift, as by Equation 5-3. Furthermore, the amplitude A_2 should have been larger, to have an even larger effect on BPF2. There was however no more testing time to implement further iterations.

Analytical

Further optimization was possible using the Python code, to see if the tones can match the recorded tones in the experiment. Two different designs were considered, one where the sines are superimposed onto each other, and one where they are on each side of a ring, shown in Fig. 5-29.

(A) One-sided obstruction (superposition) (B) Two-sided obstruction

Figure 5-29 Different multi-modal designs, targeting BPF1 and 2

For the one-sided obstruction, a slightly smaller loss in flow rate was again found. However, the two-sided obstruction does allow for better control of the individual tones, and (following that) has a smaller effect on the harmonics. This is shown in Fig. 5-30, where the spectra as calculated with the Python code is shown. Note that the tones match the experiment (see for example Fig. 5-7), demonstrating that this obstruction (with proper phase alignment) should be able to cancel both of the tones completely.

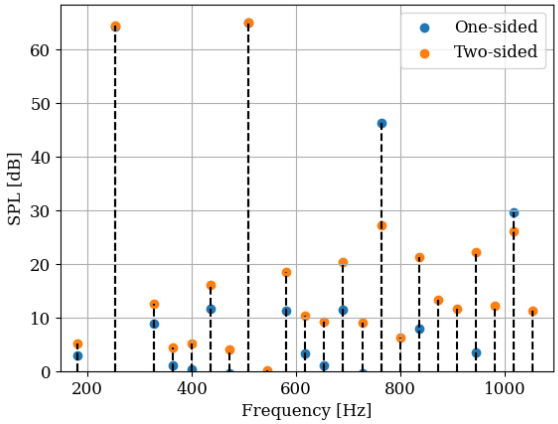

Figure 5-30 Tonal noise from multi-modal designs

Finally, it was verified that it is also possible to control tones that are not harmonics of each other. Since orders 12 and 14 were dominant tones in the experiment, these were used as illustrative example. Again, it is possible to superimpose them, or use a double-sided ring, as shown in Fig. 5-31.

(A) One-sided obstruction (superposition) (B) Two-sided obstruction

Figure 5-31 Different multi-modal designs, targeting order 12 and 14

The mass flow loss was again slightly smaller for the one-sided design. The tones that are created from this obstruction are then shown in Fig. 5-32.

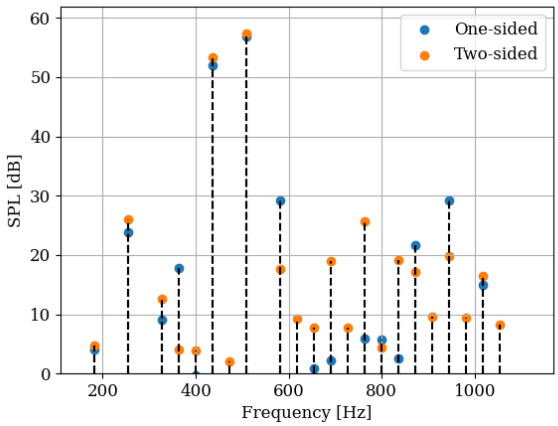

Figure 5-32 Tonal noise from multi-modal designs

As can be seen in the figure, indeed the intended tones are generated and can be used to control the primary tones. However, as with the previous design, more tones start to be generated with multi-modal obstructions.

Note that this is an example to show that multi-modal obstructions can control multiple tones. When applying it to a fan, the phases and amplitudes would first have to be found for each mode separately, after combining them into a single obstruction. It could also be extended to even more tones, with the caveat that the flow loss might become too large. Furthermore, controlling tones of higher frequency is more difficult, as the angular periodicity decreases, hence the (angular) placement of the obstruction has to be more accurate.

6

Discussion, conclusions and recommendations

This chapter finalizes the report. A discussion on the results, placing it in the larger context is given in Section 6.1. Following that, in Section 6.3, the main conclusions, answering the research questions formulated in the introduction are summarized. Finally, some recommendations for future research are suggested in Section 6.2.

6.1 Discussion

In this section, the results of the thesis are discussed in a larger context In Sec. 6.1.1, the results of this thesis are compared to similar works in the literature. Focus is put on the observed differences and hypotheses on why these occur.

6.1.1 Comparison to literature

The activities completed in this thesis continue on some ideas/papers found in the literature. Most notably, the work from Gerard et al [32][31], and Moreau et al [57]. This section therefore comments on how the results of this thesis compare to their findings.

First and foremost, this thesis confirms that flow obstructions are an effective means to control tonal noise in low Mach number, axial fan applications. The presence of upstream heat exchangers (which is different to the cited literature), does not diminish the noise reductions. What is furthermore good to note is that the primary noise was deliberately enhanced in the mentioned literature. Gerard et al [31] did this by placing a triangular obstruction between the stators, or using a small tape, enhancing the primary tone. This is shown in Fig. 6-1. Moreau et al [57] on the other hand deliberately chose the number of stators to be the same as the blade number, creating a rotor-stator interaction noise of over 80dB. In this thesis, the obstruction was used to control the primary noise as it is 'naturally' generated in the fan configuration, which is already designed for low noise.

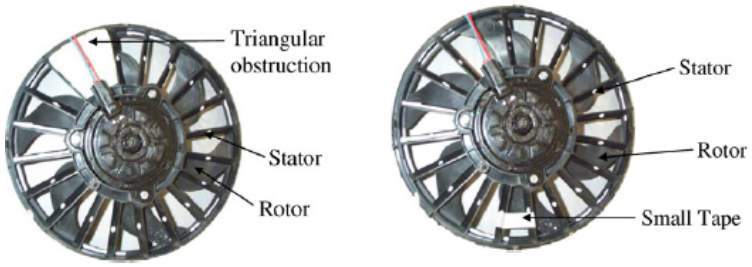

(A) Triangular obstruction (B) Small tape

Figure 6-1 Methods used to enhance primary noise by Gerard et al [31]

What was furthermore seen is that the whole-space is effected much more uniformly in the literature. In the current research, the reduction on axis are in the range of 10-15dB, whereas this is just 5dB away from the axis. Both Gerard et al [31] and Moreau et al [57] reported larger reduction away from the rotor axis. This is likely because in the current application other modes are also significant contributors to the noise. Hence when the one circumferential mode is diminished, other modes are now dominant. It should be noted that they also measured further away from the rotor (2m instead of 1m). It is known that pressure mode 0 propagates the most efficient, hence the further away the measurement, the more dominant pressure mode 0 becomes.

Prediction of the lobe amplitude and angle with PowerFLOW

The estimation of the lobe amplitude and phase by PowerFLOW corresponds better to experimental data in the work of Moreau et al [57].

One reason could be that the numerical setup is better or more refined. There is not really any evidence to back this up though. The smallest voxel reported by Moreau is 0.5mm ($\approx$ 770 voxels/diameter), whereas this is 0.48mm (900 voxels/diameter) in this research. The region of this smallest voxel does however cover the entire obstruction, rotor and stator, which is not completely the case here, see Section 3.2. The total number of voxels, timestep and CPUH's is also similar in both setups. A newer version of PowerFLOW (v6 vs v4) was used in this thesis. The total simulation time is longer in the work by Moreau et al [57]. However, statistical data was presented in this thesis and the predictions were still off considering the standard deviation. Still, in hindsight longer simulation times are recommended to simulate the obstruction angle. Given the cost of these simulations, doing this experimentally is the preferred option if possible.

A second explanation of this difference could be the fact that the configuration used by Moreau et al [57] is more simplified. It consists of only the rotor, stator and obstruction. In the setup in this application, the shroud, radiator and condenser make the setup more complex. This also means that almost all noise is generated in the single circumferential mode in the work of Moreau, which is not the case here. The phase of this fluctuation is also evident, by simply observing the angle of the stator. In this application, it was observed in the measured force fluctuations, that the phase of the fluctuation can vary over time, and between blades, which is shown in Fig. 6-2.

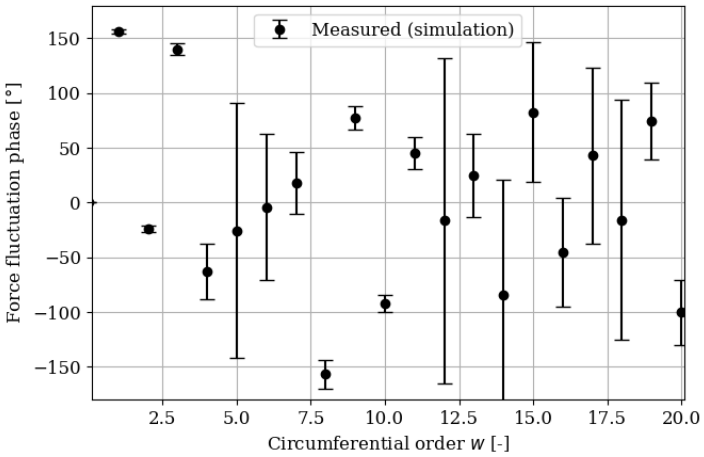

Figure 6-2 Angle of the primary force fluctuation, measured in simulation

The error-bars indicate one standard deviation. As can be seen in the figure, when the force fluctuation is strong (order 1-3 example), the phase angles are constant and clearly identifiable. However, when the fluctuations are smaller, large fluctuations in the relative phase are seen. When looking at mode 7, responsible for most of the generated noise on BPF, a standard deviation of around 50°is observed, which is very large. This also explains why identifying the correct phase angle using PowerFLOW in a more complex configuration is challenging.

Note that Magne et al [51] also found deviations in the obstruction angle optimization in simulations with a centrifugal fan. However, they did not provide a hypothesis as to why those discrepancies exist.

Obstruction noise at lower RPM

It was furthermore investigated what the effect of the obstruction is when the fan is operating at a different (lower) rotational velocity. This was not investigated by either Gerard et al [31] or Moreau et al[57]. Although they did look at the aerodynamic performance of the obstruction along the fan performance curve, no information is given on the acoustics. Goth et al [36] did test this for a large industrial fan, and saw noise reductions up to 55% duty cycle. Going lower would result in a noise increase, however it was reported that noise levels are already low at these rotational velocities.

In this research, noise reductions were seen for all investigated duty cycles, also going down to 35%. It was observed that the noise interference pattern (relation between the targeted tonal noise and obstruction angle) shifts slightly when going to a lower duty cycle. It was hypothesised that this has to do with the pre-swirl of the obstruction wake. With the relatively short distance of the obstruction to the fan, and the presence of heat exchangers which prohibit this rotation, the pre-swirl is limited in this application. So when, going to a lower duty cycle, the angle at which the wake reaches the fan blades remains relatively constant. In the work of Goth et al [36], the obstruction was placed at a considerable distance upstream of the fan, hence the preswirl is more pronounced, which could explain there observations. Furthermore, the change in the amplitude of the tonal noise could be more pronounced. When the primary tone at BPF reduces significantly (which was not the case in this research), the secondary tone introduced with the obstruction can be too loud and actually introduce noise.

Predictions with low-fidelity model

Two differences where furthermore seen when designing obstructions using the low-fidelity code.

First of all, the harmonic content rate is higher in literature (around 15% in literature vs 7% here). This is mainly affected by the Gaussian parameter in circumferential direction. The wake that was observed in simulation here was very 'clean', the velocity deficit was very pronounced. This is case-specific and dependent on the distance between the fan and obstruction, together with the presence of radiators, and the shape of the obstruction. A flat-top velocity profile could be considered to model the wake instead of the Gaussian assumption.

Secondly, the linear relation between lobe amplitude and noise, suggested by Moreau et al [57] was not found here. Although it was valid for small obstructions sized, when the obstruction approached half of the

radius of the fan, it was no longer valid. This was not commented on by Moreau et al [57] or Gerard et al [32]. Experiments would have to be carried out to validate if this is indeed true.

6.2 Conclusions

In this section, the conclusions drawn from this thesis will be summarized. This will be done by answering the research questions proposed in the introduction. For each, the sub-questions are addressed, after which the main research question is discussed.

1. (a) **A plane acoustic wave, or circumferential pressure mode 0, is dominant on nearly all tones in the majority of the far-field. On most tones, this mode is a result of a non-uniform inflow causing a periodic force fluctuations.**

   In the fan configuration with unequal blade spacing, tones are generated on all harmonics of the rotational frequency. Each tone is composed of rotating pressure modes, of which order 0 is usually dominant, especially moving further from the fan, and away from the rotor plane. This mode is generated from a blade force fluctuation having the same order as the tone's harmonic. For example, generally speaking, a force fluctuations of order $s = 12$ will be responsible for most of the noise on harmonic $N = 12$ of the rotational frequency.

   By calculating the force fluctuations from the fan inflow, it was observed that except for order 8-10, all force fluctuations were a result of the non-uniform inflow. In terms of acoustics, the fluctuations caused by rotor-stator interaction did not cause significant tones. The non-uniform flow was caused by the shroud design and positioning of the radiator.

   Since pressure mode 0 is nearly always the dominant sound radiator, initial obstruction design is possible with solely acoustic measurements. The obstruction lobe number should be chosen equal to the harmonic number N of the tone to be controlled. For equally spaced fans this will normally be the number of blades, as the BPF tone is dominant, but this is not necessarily the case for unequally spaced fans.

   (b) **Sinusoidal obstructions upstream of the inner part of the rotor minimize the mass flow loss for a given tone, while the harmonic content rate is sufficiently low.**

   From the investigated obstruction geometries given in Fig. 5-10, a sine on the hub was the most effective. The loss in flow rate was lowest for a given tone. This is likely because the axial velocity in this region is also lowest. Although a 'double-sine' design demonstrated even lower harmonic content rates, hence targeting a single tone more efficiently, this design showed an increased loss in flow rate.

   (c) **Heat exchangers do not compromise the noise reduction capabilities of flow obstructions.**

   Numerically, the wake of the obstruction was affected due to the presence of the porous media. Nevertheless, the secondary source was generated on the fan blades and interference patterns could be retrieved. In experiment, flow obstructions worked as intended and smaller lobe sizes than predicted were sufficient to generate the secondary tone.

   (d) **Targeting a single tone in an unequally spaced fan yields similar noise reductions on that tone when compared to equally spaced fans (literature). However, the reduction in OSPL or overall tonality is small, as more other tones exist.**

   Since the dominant pressure mode was still the plane wave on most harmonics, the obstructions can cancel or reduce the noise at a targeted tone similar to equally spaced fans. The overall reduction when doing so is however smaller. A reduction in OSPL of 0.3-0.5dB was seen, depending on the microphone location. In terms of total TNR, this was reduced from around 150 to 140dB, depending on the location.

   When comparing this to results from Moreau [57] and Gerard [31], the tonal reductions were of similar magnitude. However, the directivity of the reduction is smaller away from the axis in this study. A more uniform reduction was observed in their studies.

   (e) **Multi-modal obstructions are able to control multiple tones**

   Using a superposition of two cosines with a different order was successful in reducing two separate tones. Still, increased flow loss and introducing tones other than the targeted tone are a risk. The amount of tones to be controlled in unequally spaced fans is large (5-15 separate tones), so controlling all tones is not feasible with a superposition of obstructions.

(f) **An obstruction designed for maximum duty cycle, still reduces noise at lower fan RPM, but not as effective**

The angle for maximum interference changes slightly when spinning at a lower duty cycle. This, and the fact that the amplitude is not optimized for the operating condition results in a smaller effect of the obstruction. Still, no noise increase was observed at any duty cycle compared to having no obstruction. Goth et al [36] observed noise reduction above 55% duty cycle, below which the obstructions increased the noise.

This leads to answering the main research question:

In what way can flow obstruction reduce the tonal noise of the fan configuration while limiting aerodynamic losses, and why?

Placing a sinusoidal flow obstruction upstream of both the radiator and condenser reduces a tonal noise significantly. The lobe number has to be equal to the harmonic number of the tone to be controlled, and the sizing and angular positioning of the obstruction are important. The size has to be chosen to create a secondary force fluctuation with an equal magnitude of the primary force fluctuation of that particular order. The angle has to be chosen such that the fluctuation is in anti-phase with the primary fluctuation. Placing the sine on the inner radius of the rotor limits the mass flow loss as the flow rate is lower in this area. Using a superposition of sines, creating a multi-modal obstruction can also control multiple tones, and is recommended in fans with unequal blade spacing. The total noise reduction and summed Tonal Noise Ratio are larger compared to using 1 sine, but a balance must be struck to not compromise flow loss or introduce unwanted tones.

Now the conclusions related to the sub-questions of the second research question are addressed:

2. (a) **A Gaussian wake filter can be used to model the obstruction wake**

Using a 2D (cylindrical) Gaussian filter kernel was able to generate a similar wake as the method proposed by Gerard et al [32]. Furthermore, with proper tuning of the wake parameters, the wake definition was similar to a measured obstruction wake in high-fidelity simulations, with upstream radiator and condenser present.

(b) **A 1D Sears gust approach can predict unsteady blade loading within a standard deviation of force measurements in high-fidelity simulations, for most orders.**

The blade force fluctuations could be predicted with a 1D transversal gust. Force fluctuations due to rotor-stator interaction were not included. It was found that an accurate distribution of the chord along the blade span is needed for a correct prediction.

(c) **A single rotating dipole per blade correctly models the far-field tonal noise due to a force fluctuation. However, for unequally spaced fans, the relative blade angles have to be known with less than 1°accuracy**

A single rotating dipole at each blade, was a valid compactness assumption up to (at least) 1kHz. Tonal noise correlated well to an FWH formulation from the blade pressure fluctuations measured in high-fidelity simulation. When summing multiple blades it was found that the relative spacing has to be very accurate, as the interference is sensitive to small variations.

This leads to answering the second research question:

Are the assumptions in the model proposed by Gerard et al [32] valid on the fan configuration?

The assumptions in the model by Gerard et al [32] are valid on the fan configuration, and tonal noise predictions caused by a non-uniform inflow can be made when the inflow is known. When calculating the noise from a flow obstruction, information on the wake parameters is still needed. However, these are only needed from one simulation or experiment. For unequally spaced fans, the relative blade angles are needed with an accuracy under 1°.

6.3 Recommendations

From this thesis and it's conclusions, a few recommendations regarding future research are formulated, which are divided in a few categories:

Numerical

- **Aerodynamic optimization:** Aerodynamic optimization of the obstruction shape is recommended to minimize the aerodynamic loss further. Design variables could include obstruction thickness, chamfer, edge fillet, distance to fan etc. The analysis could be carried out with RANS equations since only the non-uniform stationary wake of the obstruction is of interest. The design objective should be to create a force fluctuation as strong as possible with minimal loss in flow rate, which can be assessed with the low-fidelity model.
- **Combine RANS with model:** It was shown that tonal noise can be predicted with just the axial inflow to the fan. It is therefore recommended to run a (cheaper) RANS simulation where the rotor is modeled as an actuator disk (source term in the momentum equation). It is recommended to take an axial slice from this (fine-mesh) simulation and calculate the tonal noise using this inflow analytically. This can then be correlated to the LBM simulations/experimental data. If this is possible, it allows for significantly cheaper obstruction design and optimization.

Experimental

- **Aerodynamic penalty and operating regime:** It is recommended to validate the aerodynamic penalty experimentally using two separate pressure chambers. Furthermore, the workings of the obstruction should be validated when a flow is present; during driving, the obstruction should not introduce unintentional noise.
- **Multi-modal obstructions/evenly spaced fan:** Larger noise reduction is realistic when going back to evenly spaced fans. Applying multimodal obstructions to reduce the first and second BPF should yield significant noise attenuation. It is also recommended to investigate if it is best to go back to equal stator spacing with the same number of stators as rotors. This effectively puts all the acoustic energy in a single mode, which can be controlled with an obstruction. The angular placement of the obstruction should be obvious in this case. The obstruction might however become too large and compromise the flow/efficiency, which should be investigated. It is recommended to use a circular arc upstream of the fan to allow for modal analysis of these experiments.

Analytical

- **Include stator effect:** The potential effect of the stator on the rotor should be accounted for in the calculation of the unsteady force.
- **Modeling of obstruction wakes:** It should be researched whether it is possible to model the wake of the obstruction without measuring the wake parameters from higher-fidelity methods. Factors that could influence this is the shape of the obstruction, the thickness, the chamfer and/or edge fillet, the distance to the fan and the size and rotational velocity of the fan. The presence of radiator and/or condenser should be included, possibly using Darcy's law.
- **Inclusion of angle of attack and camber:** Although a good agreement between the force fluctuations of low and high-fidelity models was found, it should be investigated if including the blade camber, angle of attack and thickness can further improve the aeroacoustic tonal predictions.
- **Incorporate blade spacing in the computation of force fluctuations:** It was observed in simulation that the force (fluctuations) vary between different blades (having a different spacing to the previous blade). It is therefore recommended to investigate if this can be included based on the respective blade angle, and if it influences the acoustic results.

References

[1] *Acoustics – Determination of sound power levels of noise sources using sound pressure – Comparison method in situ*. Standard ISO 3747:2000. Geneva, CH: International Organization for Standardization, 2000. URL: https://www.iso.org/standard/21749.html.

[2] Sabry Allam and Mats Åbom. *Acoustic modelling and characterization of plate heat exchangers*. Tech. rep. SAE Technical Paper, 2012.

[3] Sabry Allam and Mats Åbom. "Noise reduction for automotive radiator cooling fans". In: *configurations* 15 (2015), p. 17.

[4] Roy K Amiet. "Acoustic radiation from an airfoil in a turbulent stream". In: *Journal of Sound and vibration* 41.4 (1975), pp. 407–420.

[5] Roy K Amiet. "Compressibility effects in unsteady thin-airfoil theory". In: *AIAA Journal* 12.2 (1974), pp. 252–255.

[6] Roy K Amiet. *Noise produced by turbulent flow into a rotor: theory manual for noise calculation*. Tech. rep. 1989.

[7] O. Amoiridis et al. "Sound localization and quantification analysis of an automotive engine cooling module". In: *Journal of Sound and Vibration* 517 (Jan. 2022). Sound source localization, effect of radiator. ISSN: 10958568. DOI: 10.1016/J.JSV.2021.116534.

[8] Davide Anghinolfi et al. "Psychoacoustic optimization of the spacing of propellers, helicopter rotors, and axial fans". In: *Journal of Propulsion and Power* 32.6 (2016), pp. 1422–1432.

[9] William K Blake. *Mechanics of flow-induced sound and vibration, Volume 2: Complex flow-structure interactions*. Academic press, 2017.

[10] Stephane Caro and Stephane Moreau. "Aeroacoustic modelling of low pressure axial flow fans". In: *6th Aeroacoustics Conference and Exhibit*. 2000, p. 2094.

[11] Damiano Casalino et al. "Lattice-Boltzmann calculations of rotor aeroacoustics in transitional boundary layer regime". In: *Aerospace Science and Technology* 130 (2022), p. 107953.

[12] Alessandro Corsini and Franco Rispoli. "Using sweep to extend the stall-free operational range in axial fan rotors". In: *Proceedings of the Institution of Mechanical Engineers, Part A: Journal of Power and Energy* 218.3 (2004), pp. 129–139.

[13] Felix Czwielong et al. *Experimental investigation of the influence of different leading edge modifications on the sound emission of axial fans downstream of a heat exchanger*. Universitätsbibliothek der RWTH Aachen, 2019.

[14] A Fm' Deming. *Noise from propellers with symmetrical sections at zero blade angle, II*. Tech. rep. 1938.

[15] Guo-Qing Di et al. "Improvement of Zwicker's psychoacoustic annoyance model aiming at tonal noises". In: *Applied Acoustics* 105 (Apr. 2016), pp. 164–170. DOI: 10.1016/j.apacoust.2015.12.006. URL: https://doi.org/10.1016/j.apacoust.2015.12.006.

[16] PE Doak and PG Vaidya. "A note on the relative importance of discrete frequency and broad-band noise generating mechanisms in axial fans". In: *Journal of Sound and Vibration* 9.2 (1969), pp. 192–196.

[17] W Dobrzynski. "Propeller noise reduction by means of unsymmetrical blade-spacing". In: *Journal of sound and vibration* 163.1 (1993), pp. 123–126.

[18] Con Doolan and Danielle Moreau. *Flow Noise: Theory*. Springer Nature, 2022.

[19] PE Duncan and B Dawson. "Reduction of interaction tones from axial flow fans by non-uniform distribution of the stator vanes". In: *Journal of Sound and Vibration* 38.3 (1975), pp. 357–371.

[20] Donald Ewald, Armin Pavlovic, and John G. Bollinger. "Noise Reduction by Applying Modulation Principles". In: *The Journal of the Acoustical Society of America* 49 (5A May 1971), pp. 1381–1385. ISSN: 0001-4966. DOI: 10.1121/1.1912513.

[21] Kevin J Farrell and Walter S Gearhart. *Technique for reducing acoustic radiation in turbomachinery*. US Patent 6,375,416. Apr. 2002.

[22] H Fastl and E Zwicker. *Psychoacoustics: facts and models*. 3rd edition. Berlin, Germany: Springer Verlag, 2006.

[23] N Le S Filleul. "An investigation of axial flow fan noise". In: *Journal of sound and vibration* 3.2 (1966), pp. 147–165.

[24] T Fukano and C-M Jang. "Tip clearance noise of axial flow fans operating at design and off-design condition". In: *Journal of sound and vibration* 275.3-5 (2004), pp. 1027–1050.

[25] T Fukano, Y Takamatsu, and Y Kodama. "The effects of tip clearance on the noise of low pressure axial and mixed flow fans". In: *Journal of sound and vibration* 105.2 (1986), pp. 291–308.

[26] T. Fukano, Y. Kodama, and Y. Senoo. "Noise generated by low pressure axial flow fans, I: Modeling of the turbulent noise". In: *Journal of Sound and Vibration* 50 (1 Jan. 1977), pp. 63–74. ISSN: 10958568. DOI: 10.1016/0022-460X(77)90551-X.

[27] Tjeu Gehlen. *Automotive Cooling Fan Noise Reduction: A Literature Review*. Tech. rep. University of Technology, Delft, 2023.

[28] A Gerard et al. "Passive adaptative control of tonal noise from subsonic axial fans using flow control obstructions". In: *Fan Noise 2007, Lyon, France, September 2007*. 2007.

[29] Anthony Gerard, Alain Berry, and Patrice Masson. "Automatic positioning of flow obstructions to control tonal fan noise". In: *INTER-NOISE and NOISE-CON Congress and Conference Proceedings*. Vol. 2009. 9. Institute of Noise Control Engineering. 2009, pp. 69–80.

[30] Anthony Gérard et al. "Design of multi-modal obstruction to control tonal fan noise using modulation principles". In: *Journal of Sound and Vibration* 356 (2015), pp. 34–47.

[31] Anthony Gérard et al. "Experimental validation of tonal noise control from subsonic axial fans using flow control obstructions". In: *Journal of sound and vibration* 321.1-2 (2009), pp. 8–25.

[32] Anthony Gérard et al. "Modelling of tonal noise control from subsonic axial fans using flow control obstructions". In: *Journal of sound and vibration* 321.1-2 (2009), pp. 26–44.

[33] Marvin E Goldstein. "Aeroacoustics". In: *New York* (1976), p. 293.

[34] Maren Gollub et al. "Annoyance Reduction of the Cooling Fan Noise". In: *ATZ worldwide* 121.7-8 (July 2019), pp. 16–21. DOI: 10.1007/s38311-019-0079-2. URL: https://doi.org/10.1007/s38311-019-0079-2.

[35] Lee James Gorny. *Sound attenuations of axial fan blade tones using flow-driven tunable resonator arrays*. The Pennsylvania State University, 2009.

[36] Yvon Goth et al. "Fan tonal noise reduction using calibrated obstructions in the flow—an experimental approach". In: *Fan2012, Senlis, Frankreich* (2012).

[37] L Gutin. "On the sound field of a rotating propeller". In: *Physikalische Zeitschrit der Sowjetinion: Physical magazine of the Soviet Union volume 9 number 1* 9.NACA-TM-1195 (1948).

[38] Donald B Hanson. "Helicoidal surface theory for harmonic noise of propellers in the far field". In: *AIAA journal* 18.10 (1980), pp. 1213–1220.

[39] Gert Herold, Florian Zenger, and Ennes Sarradj. "Influence of blade skew on axial fan component noise". In: *International Journal of Aeroacoustics* 16.4-5 (2017), pp. 418–430.

[40] Michael Ivanovich, Mark Stevens, and Michael Wolf. "Two New Metrics for Fan System Efficiency: Fan Energy Index and Fan Electrical Power". In: Sept. 2017.

[41] Choon-Man Jang, Tohru Fukano, and Masato Furukawa. "Effects of the tip clearance on vortical flow and its relation to noise in an axial flow fan". In: *JSME International Journal Series B Fluids and Thermal Engineering* 46.3 (2003), pp. 356–365.

[42] Frank Kameier and Wolfgang Neise. "Rotating blade flow instability as a source of noise in axial turbomachines". In: *Journal of Sound and Vibration* 203.5 (1997), pp. 833–853.

[43] CFB Kemp. "Some properties of the sound emitted by airscrews". In: *Proceedings of the Physical Society* 44.2 (1932), p. 151.

[44] Viswanath Kota and MCM Wright. “Wake generator control of inlet flow to cancel flow distortion noise”. In: *Journal of sound and vibration* 295.1-2 (2006), pp. 94–113.

[45] David Lennström, Thomas Lindbom, and Arne Nykänen. “Prominence of tones in electric vehicle interior noise”. In: *International Congress and Exposition on Noise Control Engineering: 15/09/2013-18/09/2013*. Vol. 1. ÖAL Österreichischer Arbeitsring für Lärmbekämpfung. 2013, pp. 508–515.

[46] RE Longhouse. “Control of tip-vortex noise of axial flow fans by rotating shrouds”. In: *Journal of sound and vibration* 58.2 (1978), pp. 201–214.

[47] Richard E Longhouse. “Noise mechanism separation and design considerations for low tip-speed, axial-flow fans”. In: *Journal of Sound and Vibration* 48.4 (1976), pp. 461–474.

[48] MV Lowson. “Reduction of compressor noise radiation”. In: *The Journal of the Acoustical Society of America* 43.1 (1968), pp. 37–50.

[49] MV Lowson. “Theoretical analysis of compressor noise”. In: *The Journal of the Acoustical Society of America* 47.1B (1970), pp. 371–385.

[50] Stephan Magne, Stephane Moreau, and Alain Berry. “Subharmonic tonal noise from backflow vortices radiated by a low-speed ring fan in uniform inlet flow”. In: *The Journal of the Acoustical Society of America* 137.1 (2015), pp. 228–237.

[51] Stéphan Magne et al. “Tonal noise control of centrifugal fan using flow obstructions-experimental and numerical approaches”. In: *19th AIAA/CEAS Aeroacoustics Conference*. 2013, p. 2043.

[52] Robert C Mellin. “Noise and performance of automotive cooling fans”. In: *SAE Transactions* (1980), pp. 141–171.

[53] Stéphane Moreau. “A review of turbomachinery noise: from analytical models to high-fidelity simulations”. In: *Fundamentals of High Lift for Future Civil Aircraft: Contributions to the Final Symposium of the Collaborative Research Center 880, December 17-18, 2019, Braunschweig, Germany*. Springer. 2021, pp. 579–595.

[54] Stéphane Moreau. “Direct noise computation of low-speed ring fans”. In: *Acta Acustica united with Acustica* 105.1 (2019), pp. 30–42.

[55] Stephane Moreau and Michel Roger. “Effect of angle of attack and airfoil shape on turbulence-interaction noise”. In: *11th AIAA/CEAS aeroacoustics conference*. 2005, p. 2973.

[56] Stéphane Moreau and Michel Roger. “Competing broadband noise mechanisms in low-speed axial fans”. In: *AIAA journal* 45.1 (2007), pp. 48–57.

[57] Stéphane Moreau, Marlene Sanjose, and Stéphan Magne. “Optimization of tonal noise control with flow obstruction”. In: *Journal of Sound and Vibration* 437 (2018), pp. 264–275.

[58] W Neise. “Review of fan noise generation mechanisms and control methods”. In: (1992).

[59] W Neise and GH Koopmann. “Reduction of centrifugal fan noise by use of resonators”. In: *Journal of Sound and Vibration* 73.2 (1980), pp. 297–308.

[60] World Health Organization et al. *Burden of disease from environmental noise: Quantification of healthy life years lost in Europe*. World Health Organization. Regional Office for Europe, 2011.

[61] Norman C Otto, Richard Simpson, and Jason Wiederhold. *Electric vehicle sound quality*. Tech. rep. SAE Technical Paper, 1999.

[62] Romain Pain et al. “Numerical optimization of the tonal noise of a backward centrifugal fan using a flow obstruction. Part II: Flow Obstruction Optimization”. In: *Proceedings of the Fan* (2015).

[63] E.T. Paris. “Philosophical Magazine”. In: 13.99 (1932).

[64] Minjun Park, Duck-Joo Lee, and Hakjin Lee. “Experimental and computational investigation of the effect of blade sweep on acoustic characteristics of axial fan”. In: *Applied Acoustics* 189 (2022), p. 108613.

[65] Minjun Park, Duck-Joo Lee, and Hakjin Lee. “Inflow effects on tonal noise of axial fan under system resistances”. In: *Applied Acoustics* 192 (2022), p. 108737.

[66] Robert Paterson and Roy Amiet. “Acoustic radiation and surface pressure characteristics of an airfoil due to incident turbulence”. In: *3rd Aeroacoustics Conference*. 1976, p. 571.

[67] Zhigang Peng et al. “Discrete noise control of cooling fan module: Stator and rotor interaction”. In: *Applied Acoustics* 165 (2020), p. 107308.

[68] Zhigang Peng et al. “Tonal noise control of cooling fan module by using modulation principles on both rotor and stator”. In: *Turbo Expo: Power for Land, Sea, and Air*. Vol. 50985. American Society of Mechanical Engineers. 2018, V001T09A007.

[69] Haran K Periyathamby and Marek Horski. *Noise attenuating sound resonator for automotive cooling module shroud*. US Patent 6,309,176. Oct. 2001.

[70] Franck Perot et al. “Numerical optimization of the tonal noise of a backward centrifugal fan using a flow obstruction”. In: *Noise Control Engineering Journal* 61.3 (2013), pp. 307–319.

[71] C Polacsek. “Reduction of fan rotor-stator interacting modes using a novel design: An experimental study”. In: *Shock and Vibration Digest* 32.1 (2000), p. 22.

[72] Guillaume Renaud. *Dissociation of noise sources foraeronautical fans*. 2017.

[73] Patrick J Roache. “Perspective: a method for uniform reporting of grid refinement studies”. In: (1994).

[74] M Schneider and C Feldmann. “Psychoacoustic evaluation of fan noise”. In: *Fan 2015*. 2015.

[75] William R Sears. “Some aspects of non-stationary airfoil theory and its practical application”. In: *Journal of the Aeronautical Sciences* 8.3 (1941), pp. 104–108.

[76] I Jr Sharland. “Sources of noise in axial flow fans”. In: *Journal of Sound and Vibration* 1.3 (1964), pp. 302–322.

[77] Simulia. *PowerFLOW 2021 User’s Guide*. English. Version Version R2. Simulia. 108 pp.

[78] Michael Sortor. “On-system engine cooling fan measurement as a tool for optimizing cooling system airflow performance and noise”. In: *SAE International Journal of Materials and Manufacturing* 4.1 (2011), pp. 1221–1230.

[79] M Sturm et al. “Application of analytical noise models using numerical and experimental fan data”. In: *Proceedings of the 11th European Conference on Turbomachinery, Fluid Dynamics and Thermodynamics, Jyvaskyla, Finland*. 2015, pp. 25–27.

[80] Michael Sturm and Thomas Carolus. “Unsteadiness of blade-passing frequency tones of axial fans”. In: *21st International Congress of Sound and Vibration*. 248. 2014, pp. 1440–1500.

[81] S Subramanian and TJ Mueller. “An experimental study of propeller noise due to cyclic flow distortion”. In: *Journal of Sound and Vibration* 183.5 (1995), pp. 907–923.

[82] J. M. Tyler and T. G. Sofrin. “Axial Flow Compressor Noise Studies”. In: *SAE Technical Paper Series*. SAE International, Jan. 1962. DOI: 10.4271/620532. URL: https://doi.org/10.4271/620532.

[83] S.E. Wright. “Discrete radiation from rotating periodic sources”. In: *Journal of Sound and Vibration* 17.4 (Aug. 1971), pp. 437–498. DOI: 10.1016/0022-460x(71)90061-7. URL: https://doi.org/10.1016/0022-460x(71)90061-7.

[84] Selwyn Edgar Wright. “Sound radiation from a lifting rotor generated by asymmetric disk loading”. In: *Journal of Sound and Vibration* 9.2 (1969), pp. 223–240.

[85] SF Wu, S Su, and H Shah. “Noise radiation from engine cooling fans”. In: *Journal of Sound and Vibration* 216.1 (1998), pp. 107–132.

[86] Yadong Wu et al. “Blade force model for calculating the axial noise of fans with unevenly spaced blades”. In: *Applied Acoustics* 146 (2019), pp. 429–436.

[87] Florian J Zenger et al. “Experimental investigation of the noise emission of axial fans under distorted inflow conditions”. In: *Journal of Sound and Vibration* 383 (2016), pp. 124–145.

[88] Florian J Zenger et al. “Sound source localization on an axial fan at different operating points”. In: *Experiments in Fluids* 57 (2016), pp. 1–10.

[89] Yinhui Zhong, Yinong Li, and Jun Li. “Study on Noise Model of an Automotive Axial Fan Based on Aerodynamic Load Force”. In: *Applied Sciences* 12.14 (2022), p. 7326.

[90] Tao Zhu and Thomas H Carolus. “Experimental and numerical investigation of the tip clearance noise of an axial fan”. In: *Turbo Expo: Power for Land, Sea, and Air*. Vol. 55188. American Society of Mechanical Engineers. 2013, V004T10A001.

[91] Tao Zhu et al. “Rotating coherent flow structures as a source for narrowband tip clearance noise from axial fans”. In: *Journal of Sound and Vibration* 417 (2018), pp. 198–215.

A

BEM model

This appendix elaborates on the Blade Element Momentum (BEM) model used to calculate the blade steady loading. The equations used are taken from the work of Zhong et al [89]. The angles and velocities used are shown in Fig. A-1.

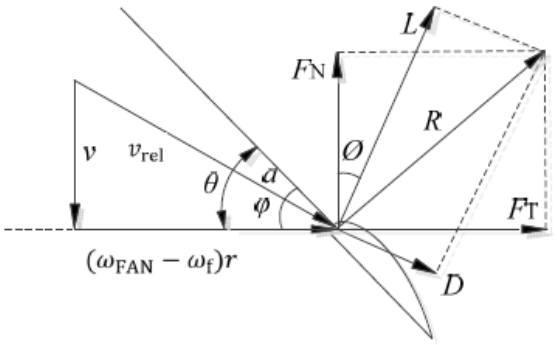

Figure A-1 Forces and angles [89]

For a complete derivation of the equation please see [89]. The method and equations that were used here are briefly described. BEM is an iterative approach, the initial values for v and ω_f were set at 5 m/s and 0 rad/s respectively. The fan was discretized in the same number of radial annuli as used for the unsteady calculation. The relative velocity v_{rel} is found using Equation A-1:

$$v_{rel} = \sqrt{v^2 + (\omega_{FAN} - \omega_f)^2 r^2} \tag{A-1}$$

Where ω_{FAN} is the fan rotational velocity and, v is the axial velocity, ω_f is the wake rotation and r is the radial coordinate. The inflow angle ϕ is then found with Equation A-2, and the angle of attack is calculated using Equation A-3.

$$tan\phi = \frac{v}{(\omega_{FAN} - \omega_f)^2)} \tag{A-2}$$

$$\alpha = \gamma - \phi \tag{A-3}$$

Where γ is the local twist angle. With the angle of attack, the lift and drag coefficient can be extracted from their respective polar. For this, a typical polar for automotive fan blades is used, proposed by Zhong et al [89]. When the airfoil shape is known, the polars can also be obtained with XFoil. The lift and drag coefficient are found with Equation A-4 and Equation A-5, respectively.

$$C_L = 0.5 + 0.08 * (\alpha - 4) \tag{A-4}$$

$$C_D = \frac{0.5 + 0.08 * (\alpha - 4)}{-0.116071\alpha^4 + 0.407738\alpha^3 + 0.5625\alpha^2 + 14.592262\alpha + 14.553571} \tag{A-5}$$

In this equation, the angle of attack α should be input in degrees. To accout for tip losses, the Blount tip model is used, in Equation A-6.

$$C_F = \frac{2}{\pi} arccos\left(e^{-f_\omega}\right) \tag{A-6}$$

Where f_ω is given by $f_\omega = \frac{B}{2}\left(\frac{R_t - r}{r sin\phi}\right)$. The axial velocity v and annular-induced angular velocity ω_f are then updated using the momentum theorem and conservation of mass, with Equation A-7 and Equation A-8.

$$8\pi v^2 r C_F = BC(r)v_{rel}^2(C_L cos\phi - C_D sin\phi) \tag{A-7}$$

$$8\pi v \omega_f r^2 C_F = BC(r)v_{rel}^2(C_L sin\phi + C_D cos\phi) \tag{A-8}$$

This process is iterated using 75% relaxation until the residuals of v are below e^{-5}, which was achieved after approximately 50 iterations. The lift force L and drag D per unit length can then be found with:

$$L = \frac{1}{2}\rho v_{rel}^2 C(r) C_L \tag{A-9}$$

$$D = \frac{1}{2}\rho v_{rel}^2 C(r) C_D \tag{A-10}$$

And the axial and tangential force is calculated using:

$$F_N = Lcos\phi - Dsin\phi \tag{A-11}$$

$$F_T = Lsin\phi + Dcos\phi \tag{A-12}$$

The angle of attack and inflow angle across the blade are then shown in Fig. A-2. And the axial and tangential force per unit span are given in Fig. A-3.

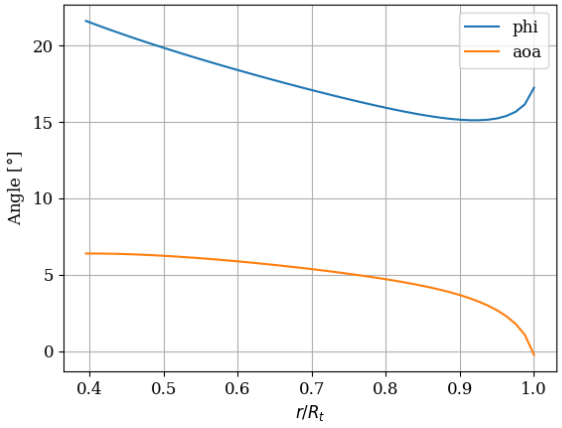

Figure A-2 Angle of attack and inflow angle

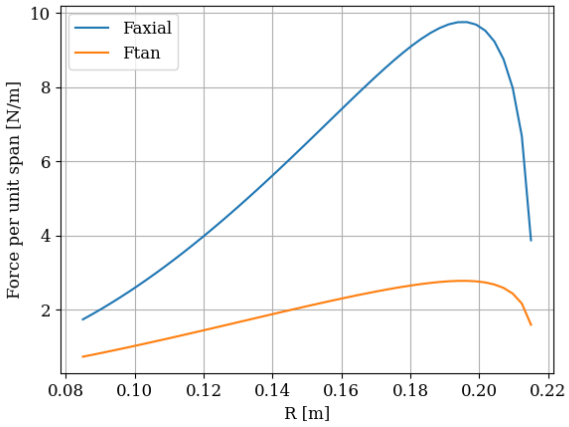

Figure A-3 Axial and tangential force

By integrating the force over the blade span, the total steady force ($F_{tot} = \sqrt{F_N^2 + F_T^2}$) per blade found by the BEM model is then 3.6N, approximately 0.4N lower compared to the measured force in simulation. This can be due to several reasons, like the tip loss being inaccurate for the shrouded ring-fan, or the fact that the BEM does not include the upstream radiator and condenser. This could be included in the momentum equation using Darcy's law, which is recommended. For noise calculations, it is not important, however, since the unsteady loading noise is louder.

B

Simulation measurements

This appendix summarizes the measurements that stored during the simulation. The visualization of the measurements is given in Section 3.2. All the sampling rates, averaging periods and times are given in Tab. B-1 on the next page.

Category	Name	Measurement time [s]	Measurement period	Variables	Measured parts
Volume	Mean_flow	meas_time	Fan rotation (averaged)	Velocity+ pressure	Measurement domain
	tr_meas_volume_find	0.00125	0.000125 s (snapshots)	Velocity+ pressure	Box around fan 500x700x700mm
	tr_meas_volume_low	meas_time	2048 timesteps (snapshots)	Velocity+ pressure	
	tr_meas_volume_high	meas_time/4	64 timesteps (averaged)	Pressure	
	tr_meas_plane_x_low	meas_time	1024 timesteps (snapshots)	Velocity+ pressure	x-aligned plane of 2mm thickness
	tr_meas_plane_x_high	meas_time	64 timesteps (averaged)	Pressure	
	tr_meas_plane_y_low	meas_time	1024 timesteps (snapshots)	Velocity+ pressure	y-aligned plane of 2mm thickness
	tr_meas_plane_y_high	meas_time	64 timesteps (averaged)	Pressure	
	tr_meas_plane_z_low	meas_time	1024 timesteps (snapshots)	Velocity+ pressure	z-aligned plane of 2mm thickness
	tr_meas_plane_z_high	meas_time	64 timesteps (averaged)	Pressure	
Standard face measurement	tr_meas_surface_low	meas_time	0.00025 s (snapshots)	Velocity+ pressure	Rotor +shroud (split in PID's)
	tr_meas_surface_high	meas_time	5e-5 s (averaged)	Pressure	Rotor +shroud (split in PID's)
Sampled face measurement	Modal_plane_1	meas_time	64 timesteps	Pressure	Circular plane, $\sqrt{0.5}$ with R = sqrt 0.5: outer radius 1 m
	Modal_plane_2	meas_time	64 timesteps	Pressure	Circular plane at 1.5 m, R = 0.75mm
Composite face measurement	Forces_rotor	meas_time	5e-5 s (averaged)	Forces	Rotor, hub, ring , and all blades measured separately
Probes	Probe_M1 - Probe_M6	sim_time	8 timesteps (averaged)	Velocity +pressure	probes at 1m distance 0,-45,45,180, 135,225 deg fan axis
	Probe_Modal1- Probe_Modal10	sim_time	8 timesteps (averaged)	Velocity+ pressure	Circular array of microphones upstream at 1 m distance

Table B-1 Measurements stored during simulation

C

Simulation convergence

This appendix presents the analyes that were done to verify the simulation grid convergence. The convergence in time is presented, as well as the convergence of aerodynamics and aeroacoustics with mesh size, that were not notable to present in the main part of the report.

Time convergence

The convergence in time of each of the simulations in the mesh convergence is shown in Fig. C-1. This is the recorded pressure on microphone 1 (mean removed). The red vertical line indicates the end of the initial 5 revolutions and where the measurements begin.

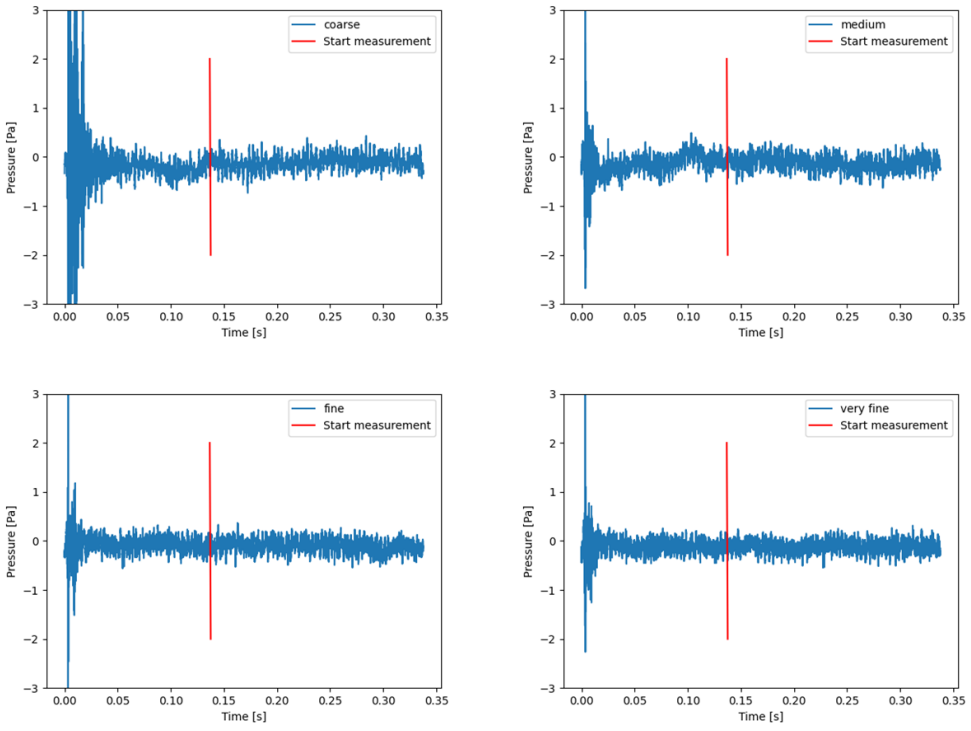

Figure C-1 Pressure time signal, time convergence

Rotor as 1D actuator

To understand the mean pressure and velocity development across the heat exchanger and rotor/stator, plane averaged quantities were used. The plane that was used for averaging is shown in Fig. C-2.

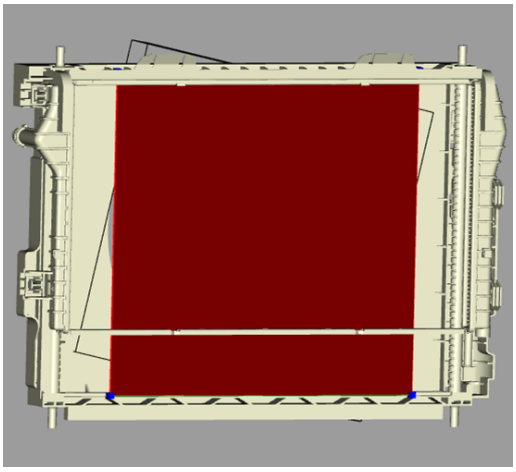

Figure C-2 Averaging plane used

The resulting axial velocity, static and total pressure and velocity magnitude are then given in Fig. C-3. Note that the velocity in the LRF region is coloured red, as caution should be taken when interpreting these results. Since the area of the plane that effectively measures velocity is reduced (due to the shroud), the velocities can be relatively higher. Furthermore, the velocity in this area is averaged in the Local Reference Frame.

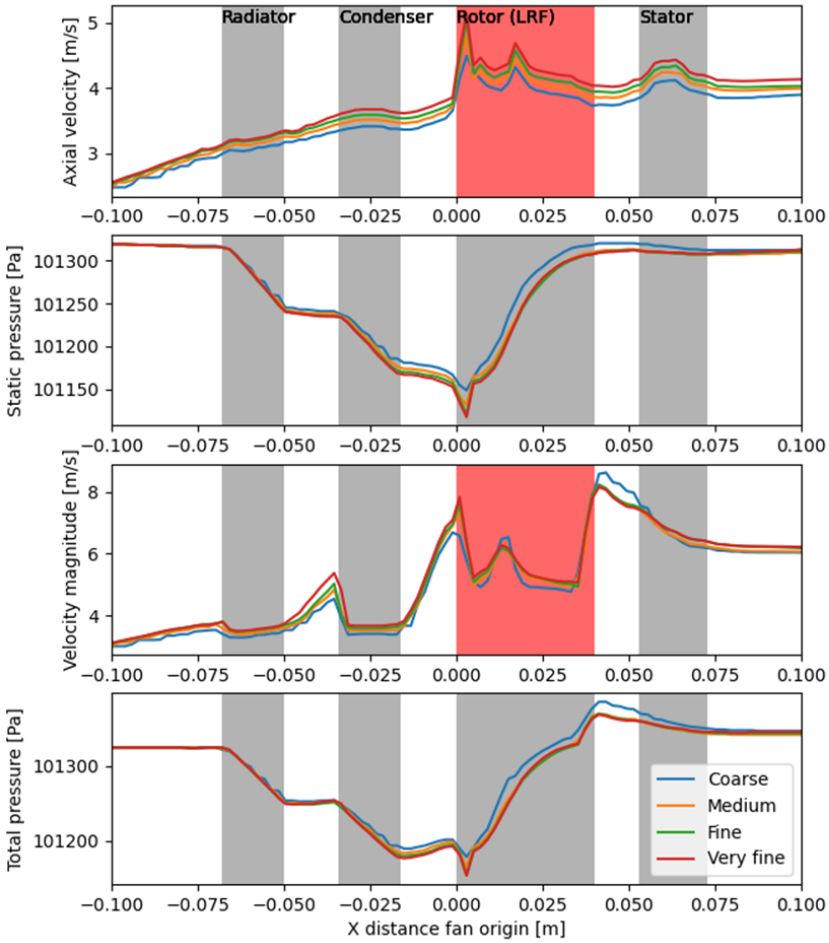

Figure C-3 Rotor as 1D 'actuator'; plane averaged quantities

What can be observed in the figure is that the development of the pressure converges well, only the coarse mesh stands out siginificantly. The axial velocity of the fan is converging but still increases slightly. The percentile change is similar to the Richardson Extrapolation of the axial force given in the report.

Slices of mean velocity

Next, some vertical and horizontal slices of the mean axial and tangential velocity are compared between mesh sizes. This is done on a few different location in streamwise direction. Upstream of the heat exchangers, downstream of heat exchangers, downstream of rotor and downstream of stator.

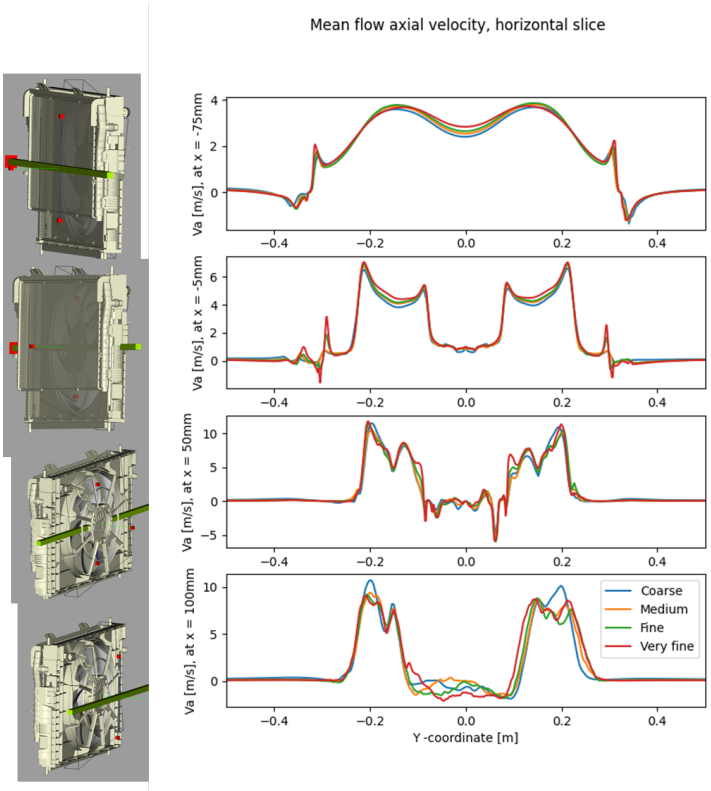

Figure C-4 Mean axial velocity horizontal line

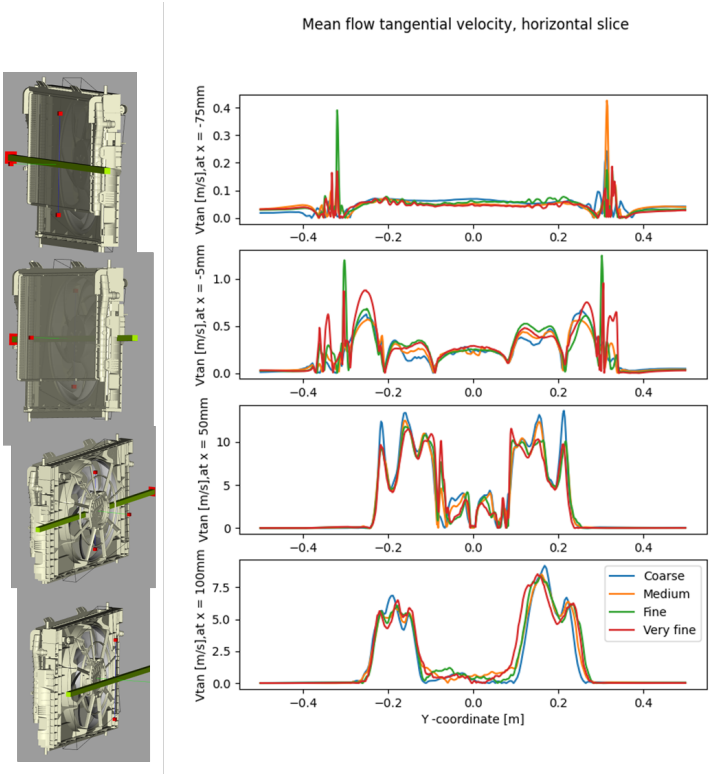

Figure C-5 Mean tangential velocity horizontal line

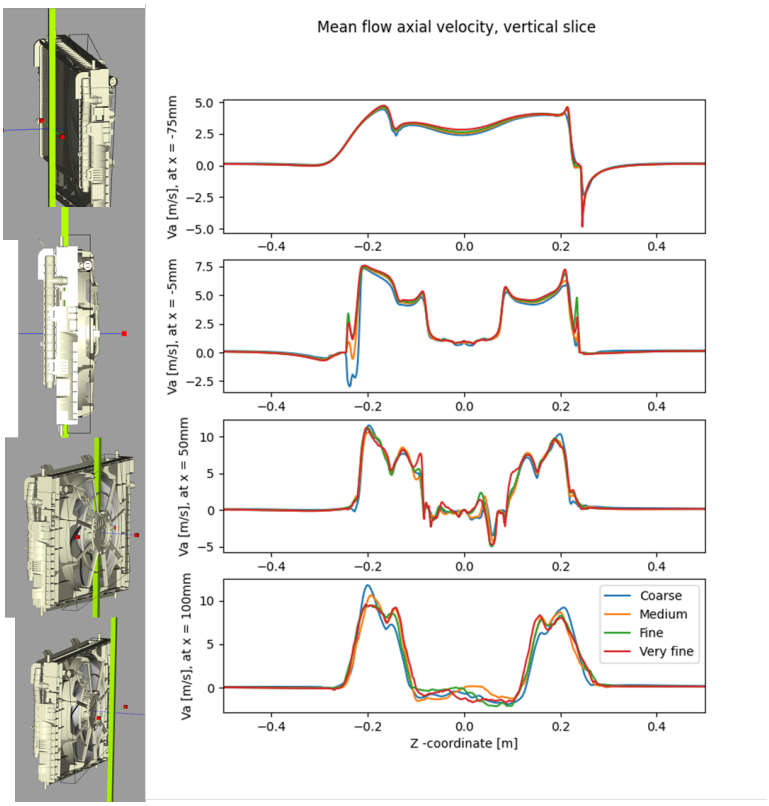

Figure C-6 Mean axial velocity vertical line

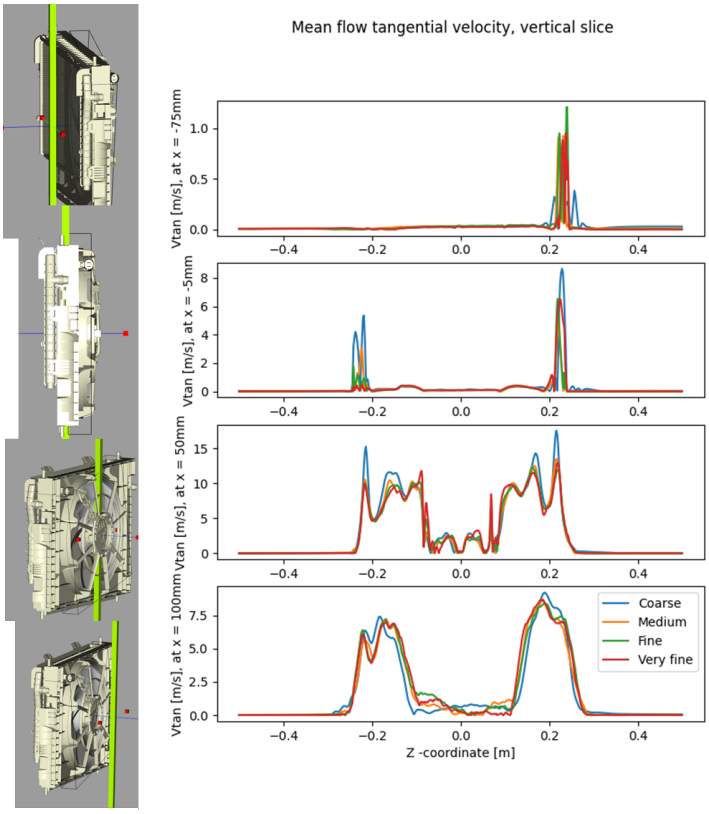

Figure C-7 Mean tangential velocity vertical line

Skin friction

The averaged blade skin friction at different spanwise locations is given in Fig. C-8. What is most notable is the earlier drop of the skin friction in the very fine mesh at $r/R = 0.72$ at the suction side (dotted line). This again confirms the earlier onset of separation in this very fine mesh.

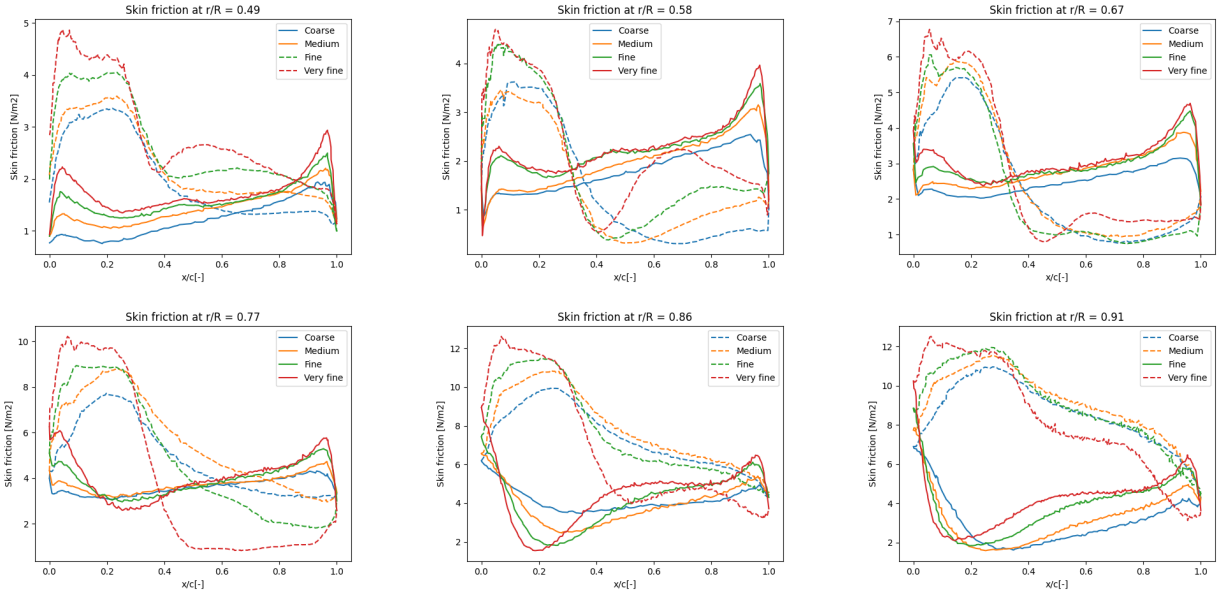

Figure C-8 Skin friction

The skin friction over the entire blade is shown in Fig. C-9, together with the surface streamlines. The

region of separated flow is visible by the blue color and lack of alignment in the streamlines.

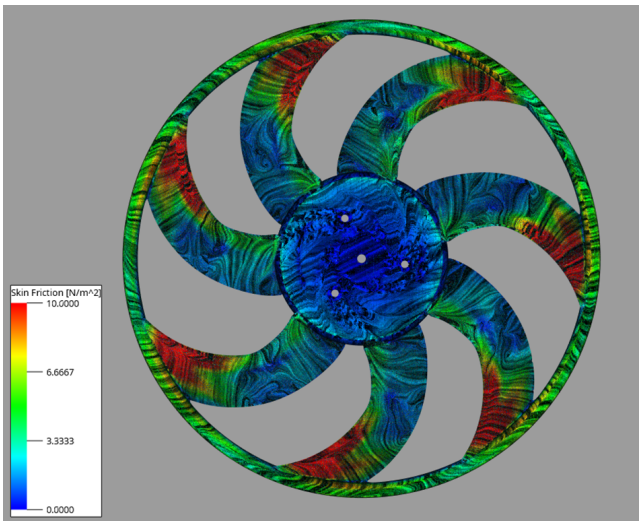

Figure C-9 Skin friction and streamlines

Surface $y+$

The surface $y+$-values at different spanwise location are given in Fig. C-10. It can be seen that the value of y+ approaches 10 on the very fine mesh for a part of the blade. This was hypothesised to be the reason for the difference in separation behaviour betweeen these mesh sizes.

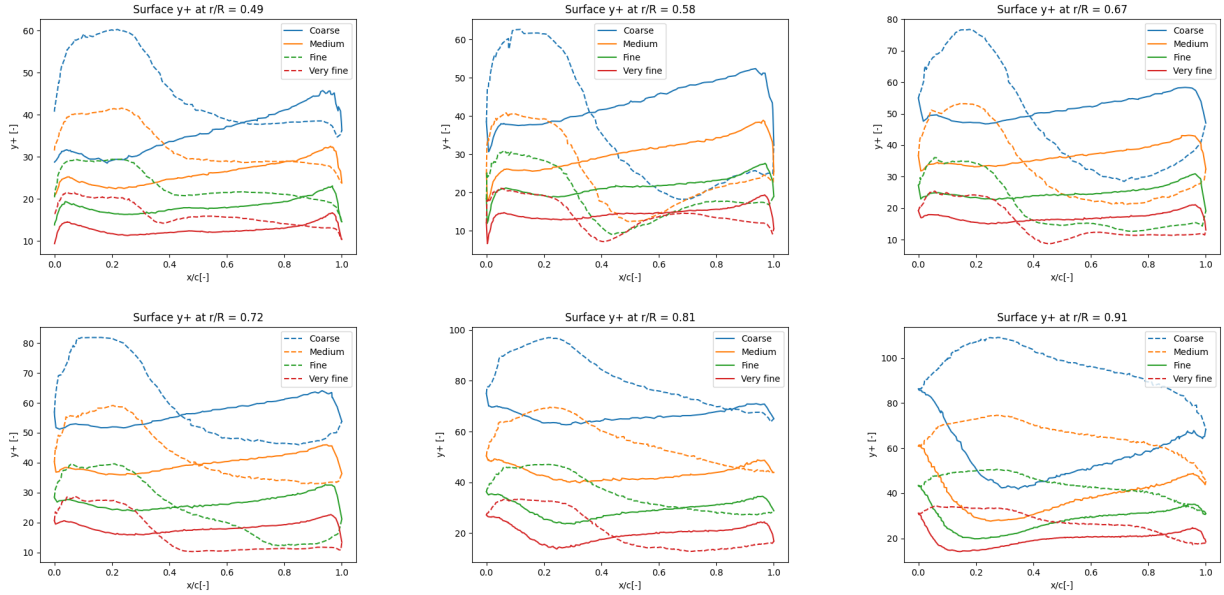

Figure C-10 y+

Convergence of acoustics

The convergence of the narrowband and broadband acoustics for all of the microphones are given in Fig. C-11 and Fig. C-12, respectively.

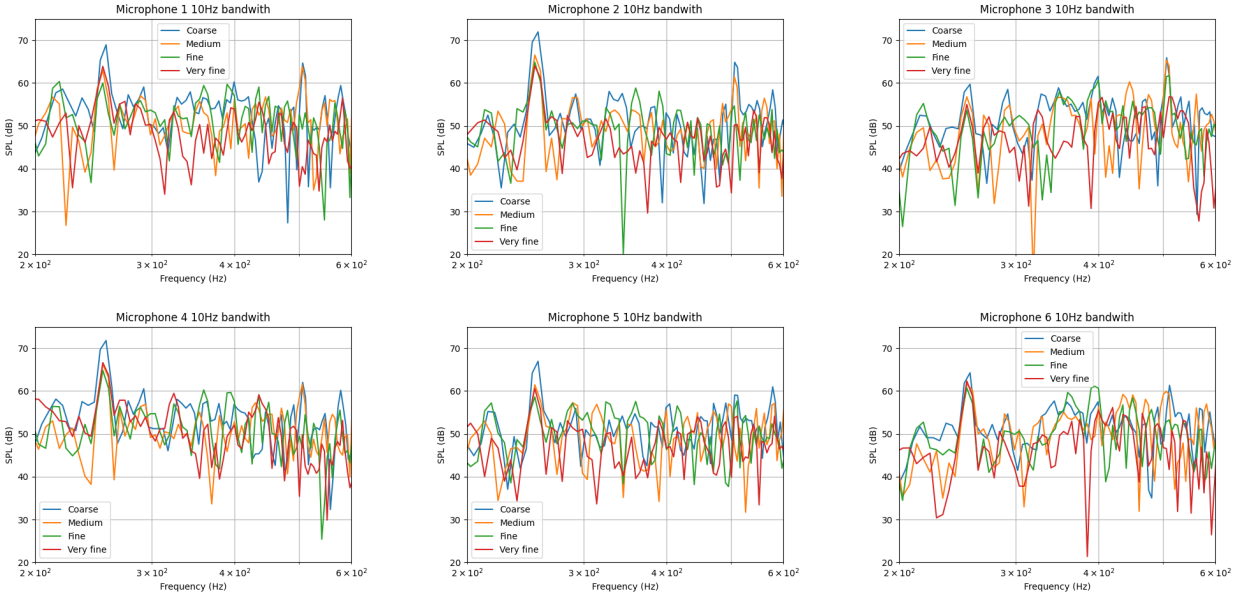

Figure C-11 Narrowband spectrum microphones

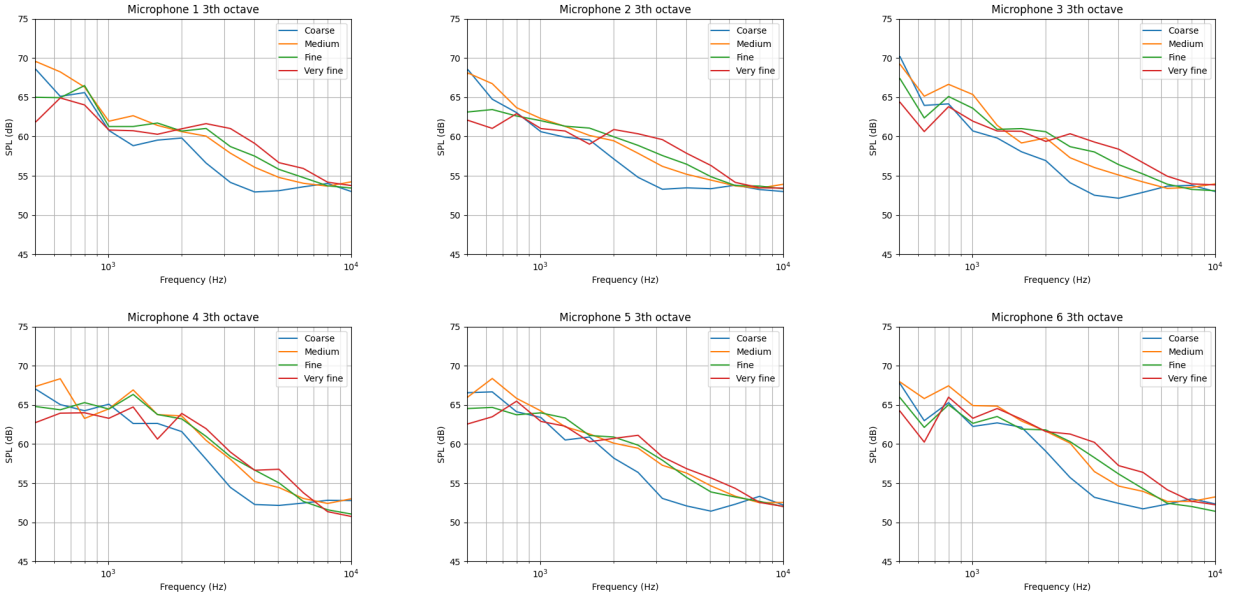

Figure C-12 Broadband spectrum microphones

Finally, it was noted in Section 3.3, that the noise from 1-4kHz was underestimated in the fine mesh. It is shown in Fig. C-13, that the very fine simulation indeed approaches the experiment better. FFA data is plotted here that was obtained at 20kHz, explaining the drop-off compared to the experiment above 4kHz.

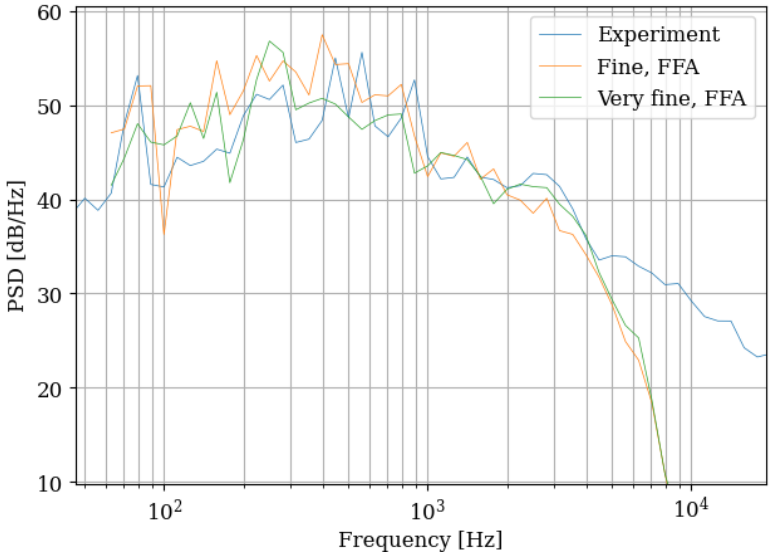

Figure C-13 Broadband fine very fine

D

Experimental campaign

This appendix lists all the tests that were conducted in the anechoic chamber. They are divided along a few tables, one for each day of testing. Day 1 is given in Tab. D-1. Note that during this day there was no proper marking of the angular position of the obstruction, hence a few angles were accidentally skipped. This sweep was therefore repeated on day 3.

Test day	Test name	Duty cycle	Obstruction	Comments
1	Background_noise	-	No	
	duty35_obstrNO	35	No	No obstruction and no ring
	duty55_obstrNO	55	No	
	duty75_obstrNO	75	No	
	duty95_obstrNO	95	No	
	duty95_obstr00_A40	95	40mm	
	duty95_obstr03_A40	95	40mm	
	duty95_obstr06_A40	95	40mm	
	duty95_obstr09_A40	95	40mm	
	duty95_obstr12_A40	95	40mm	
	duty95_obstr15_A40	95	40mm	
	duty95_obstr18_A40	95	40mm	
	duty95_obstr21_A40	95	40mm	
	duty95_obstr24_A40	95	40mm	
	duty95_obstr27_A40	95	40mm	
	duty95_obstr30_A40	95	40mm	
	duty95_obstr33_A40	95	40mm	
	duty95_obstr36_A40	95	40mm	
	duty95_obstr39_A40	95	40mm	
	duty95_obstr42_A40	95	40mm	
	duty95_obstr45_A40	95	40mm	
	duty95_obstr48_A40	95	40mm	Due to lack of marking the angular position was incorrect sweep repeated on day 3

Table D-1 Tests conducted on 06-03-2024

Tab. D-2 lists the experiments conducted on the second day of testing. Since it was observed that the 40mm obstruction was too big, a second obstruction with 30 mm amplitude was printed. Still this obstruction produced a tone that is too loud, hence an even smaller obstruction of 20mm was printed. While this was printing, the 30mm obstruction was used to test on a lower duty cycle of 75%.

Test day	Test name	Duty cycle	Obstruction	Comments
2	duty35_obstrNO	35	No	No obstruction, but with ring
	duty55_obstrNO	55	No	
	duty75_obstrNO	75	No	
	duty95_obstrNO	95	No	
	duty95_obstr00_A30	95	30mm	Lobe amplitude reduced after analyzing 40mm results
	duty95_obstr03_A30	95	30mm	
	duty95_obstr06_A30	95	30mm	
	duty95_obstr09_A30	95	30mm	
	duty95_obstr12_A30	95	30mm	
	duty95_obstr15_A30	95	30mm	
	duty95_obstr18_A30	95	30mm	
	duty95_obstr21_A30	95	30mm	
	duty95_obstr24_A30	95	30mm	
	duty95_obstr27_A30	95	30mm	
	duty95_obstr30_A30	95	30mm	
	duty95_obstr33_A30	95	30mm	
	duty95_obstr36_A30	95	30mm	
	duty95_obstr39_A30	95	30mm	
	duty95_obstr42_A30	95	30mm	
	duty95_obstr45_A30	95	30mm	
	duty95_obstr48_A30	95	30mm	
	duty95_obstr51_A30	95	30mm	
	duty75_obstr00_A30	75	30mm	Angle sweep at lower duty cycle, done while 20mm 3D-printed
	duty75_obstr03_A30	75	30mm	
	duty75_obstr06_A30	75	30mm	
	duty75_obstr09_A30	75	30mm	
	duty75_obstr12_A30	75	30mm	
	duty75_obstr15_A30	75	30mm	
	duty75_obstr18_A30	75	30mm	
	duty75_obstr21_A30	75	30mm	
	duty75_obstr24_A30	75	30mm	
	duty75_obstr27_A30	75	30mm	
	duty75_obstr30_A30	75	30mm	
	duty75_obstr33_A30	75	30mm	
	duty75_obstr36_A30	75	30mm	Repeated 2x
	duty75_obstr39_A30	75	30mm	
	duty75_obstr42_A30	75	30mm	
	duty75_obstr45_A30	75	30mm	

duty75_obstr48_A30	75	30mm	
duty75_obstr51_A30	75	30mm	
duty95_obstr00_A20	95	20mm	Lobe amplitude further reduced after analyzing 30mm results
duty95_obstr03_A20	95	20mm	
duty95_obstr06_A20	95	20mm	
duty95_obstr09_A20	95	20mm	
duty95_obstr12_A20	95	20mm	
duty95_obstr15_A20	95	20mm	
duty95_obstr18_A20	95	20mm	
duty95_obstr21_A20	95	20mm	
duty95_obstr24_A20	95	20mm	
duty95_obstr27_A20	95	20mm	
duty95_obstr30_A20	95	20mm	
duty95_obstr33_A20	95	20mm	
duty95_obstr36_A20	95	20mm	Repeated 2x
duty95_obstr39_A20	95	20mm	
duty95_obstr42_A20	95	20mm	
duty95_obstr45_A20	95	20mm	
duty95_obstr48_A20	95	20mm	
duty95_obstr51_A20	95	20mm	

Table D-2 Tests conducted on 07-03-2024

On day three, the double cosine design was tested, along with some repeat tests of the previous days. Furthermore, the radiator was removed and noise at 95% duty cycle was measured again. This is shown in Tab. D-3. Note that the difference in noise between repeat tests (on different days) was minimal. Sometimes a small difference in tonal noise (1-2dB) was observed, but overall the spectra overlap completely.

Test day	Test name	Duty cycle	Obstruction	Comments
3	duty35_obstrNO_ring	35	No	No obstruction but with ring, repeats day 2
	duty55_obstrNO_ring	55	No	
	duty75_obstrNO_ring	75	No	
	duty95_obstrNO_ring	95	No	
	duty35_obstrNO	35	No	No obstruction, no ring, repeats day 1
	duty55_obstrNO	55	No	
	duty75_obstrNO	75	No	
	duty95_obstrNO	95	No	
	duty95_obstr00_A30	95	L7,10mm,L14,10mm	Design with two cosines superimposed: DC: double cosine
	duty95_obstr03_DC	95	L7,10mm,L14,10mm	
	duty95_obstr06_DC	95	L7,10mm,L14,10mm	
	duty95_obstr09_DC	95	L7,10mm,L14,10mm	
	duty95_obstr12_DC	95	L7,10mm,L14,10mm	
	duty95_obstr15_DC	95	L7,10mm,L14,10mm	
	duty95_obstr18_DC	95	L7,10mm,L14,10mm	

duty95_obstr21_DC	95	L7,10mm,L14,10mm	
duty95_obstr24_DC	95	L7,10mm,L14,10mm	
duty95_obstr27_DC	95	L7,10mm,L14,10mm	
duty95_obstr30_DC	95	L7,10mm,L14,10mm	
duty95_obstr33_DC	95	L7,10mm,L14,10mm	
duty95_obstr36_DC	95	L7,10mm,L14,10mm	
duty95_obstr39_DC	95	L7,10mm,L14,10mm	
duty95_obstr42_DC	95	L7,10mm,L14,10mm	
duty95_obstr45_DC	95	L7,10mm,L14,10mm	
duty95_obstr48_DC	95	L7,10mm,L14,10mm	
duty95_obstr51_DC	95	L7,10mm,L14,10mm	
duty95_obstr00_A40	95	40mm	Repeats of day 1
duty95_obstr03_A40	95	40mm	
duty95_obstr06_A40	95	40mm	
duty95_obstr09_A40	95	40mm	
duty95_obstr12_A40	95	40mm	
duty95_obstr15_A40	95	40mm	
duty95_obstr18_A40	95	40mm	
duty95_obstr21_A40	95	40mm	
duty95_obstr24_A40	95	40mm	
duty95_obstr27_A40	95	40mm	
duty95_obstr30_A40	95	40mm	
duty95_obstr33_A40	95	40mm	
duty95_obstr36_A40	95	40mm	
duty95_obstr39_A40	95	40mm	
duty95_obstr42_A40	95	40mm	
duty95_obstr45_A40	95	40mm	
duty95_obstr48_A40	95	40mm	
duty95_obstr41_A40	95	40mm	
duty95_obstrNO_noradiator	95	NO	Radiator removed, measured 2x

Table D-3 Tests conducted on 08-03-2024